

NAG 3-475

LEWIS-GRANT
IN-32-CR
90660
130P.

ELECTROMAGNETICS LABORATORY
TECHNICAL REPORT NO. 87-6

August 1987

REDUCTION OF THE RADAR CROSS SECTION OF
ARBITRARILY SHAPED CAVITY STRUCTURES

R. Chou

H. Ling

S. W. Lee

(NASA-CR-180307) REDUCTION OF THE RADAR
CROSS SECTION OF ARBITRARILY SHAPED CAVITY
STRUCTURES (Illinois Univ.) 130 p Avail:
NTIS HC A07/NP A01 CSCL 20N

N87-27085

Unclas
63/32 0090660



ELECTROMAGNETICS LABORATORY
DEPARTMENT OF ELECTRICAL AND COMPUTER ENGINEERING
UNIVERSITY OF ILLINOIS AT URBANA-CHAMPAIGN
URBANA, ILLINOIS 61801

Electromagnetics Laboratory Report No. 87-6

REDUCTION OF THE RADAR CROSS SECTION OF
ARBITRARILY SHAPED CAVITY STRUCTURES

by

R. Chou
H. Ling
S. W. Lee

Technical Report

August 1987

Electromagnetics Laboratory
Department of Electrical and Computer Engineering
University of Illinois at Urbana-Champaign
Urbana, Illinois 61801

ACKNOWLEDGEMENTS

This work was supported by NASA Lewis Research Center under contract NAG3-475 and by the NSF under contract ECS 83-11345. Cray-XMP supercomputuer time was granted by the Peer Review Board at the National Center for Supercomputer Applications at the University of Illinois.

TABLE OF CONTENTS

CHAPTER	PAGE
1. INTRODUCTION.....	1
2. MODAL ATTENUATION IN MULTILAYERED COATED WAVEGUIDES	6
2.1 Introduction	6
2.2 Overview of Modal Fields in a Coated Circular Waveguide.....	8
2.3 Characteristic Equation of the Normal Modes	13
2.4 Numerical Results.....	21
2.4.1 Review of single-layer coating results	21
2.4.2 Multilayered coating.....	22
2.4.3 Radar cross section reduction.....	30
2.5 Summary	34
3. SHOOTING AND BOUNCING RAYS: CALCULATING THE RCS OF AN ARBITRARILY SHAPED CAVITY	35
3.1 Introduction	35
3.2 Formulation of Shooting and Bouncing Rays.....	37
3.2.1 Ray tracing	38
3.2.2 Amplitude tracking	40
3.2.3 Physical optics	49
3.3 Numerical Results.....	57
3.3.1 Exit ray positions.....	57
3.3.2 Comparison with modal analysis	57
3.3.3 Radar cross section of large circular cylinders	63
3.4 Summary	67
4. RADAR CROSS SECTION REDUCTION OF CAVITIES BY SHAPING.....	68
4.1 Introduction	68
4.2 Cavity Geometries	69
4.2.1 Circular cylinder	69
4.2.2 Triangle-to-circle transition waveguide	72
4.3 Numerical Results	77
4.3.1 Exit points and ray paths	80
4.3.2 Radar cross section computations	85
4.4 Summary	99

CHAPTER	PAGE
5. RAYS VERSUS MODES: PICTORIAL DISPLAY OF ENERGY FLOW IN AN OPEN-ENDED WAVEGUIDE	103
5.1 Introduction	103
5.2 Formulation	103
5.3 Numerical Discussion	107
5.4 Summary	114
6. CONCLUSIONS AND EXTENSIONS	115
APPENDIX A. BESSEL FUNCTIONS FOR LARGE ARGUMENTS WITH LARGE IMAGINARY PARTS	118
REFERENCES	120

LIST OF FIGURES

FIGURE	PAGE
1.1 Comparison of body shapes for (a) Allied moving van, with flat planar surfaces and (b) Chevrolet Corvette, with smooth, sleek curves.....	3
2.1 A coated circular waveguide.....	9
2.2 Exaggerated cross-sectional view of multilayered coated waveguide	10
2.3 Transverse field distributions of the normal modes in a) empty waveguide b) dielectric coated waveguide ($\epsilon_r = 10.0$, $\mu_r = 1.0$) at cutoff frequencies c) magnetic coated waveguide ($\epsilon_r = 1.0$, $\mu_r = 10.0$) at cutoff frequencies, and d) coated waveguide at the high-frequency limit.....	22
2.4 Attenuation constants of the HE_{11} mode in a lossy magnetic coated waveguide ($\epsilon_r = 1.0$, $\mu_r = 1.5 - j2.0$)	24
2.5 Attenuation constants of the EH_{11} mode in a lossy magnetic coated waveguide ($\epsilon_r = 1.0$, $\mu_r = 1.5 - j2.0$).....	25
2.6 Attenuation constants of the HE_{12} mode in a lossy magnetic coated waveguide ($\epsilon_r = 1.0$, $\mu_r = 1.5 - j2.0$).....	26
2.7 Normalized angle-averaged power distribution in Watts/λ^2 as a function of radial distance in a dielectric coated guide ($\epsilon_r = 10.0$, $\mu_r = 1.0$).....	27
2.8 Attenuation constants of the HE_{11} mode in a double layer coated waveguide with an inner layer of lossy magnetic material ($\epsilon_r = 1.0$, $\mu_r = 1.5 - j2.0$) and an outer layer of lossless dielectric material ($\epsilon_r = 10.0$, $\mu_r = 1.0$). The thickness of the inner layer is fixed while that for the outer layer is varied.....	28
2.9 Attenuation constants of the HE_{11} mode in a double layer coated waveguide with an inner layer of lossy magnetic material ($\epsilon_r = 1.0$, $\mu_r = 1.5 - j2.0$) and an outer layer of lossless dielectric material ($\epsilon_r = 10.0$, $\mu_r = 1.0$). The thickness of the outer layer is fixed while that for the inner layer is varied.....	29
2.10 Attenuation constants of the HE_{11} mode in a double layer coated waveguide with an inner layer of lossless dielectric material ($\epsilon_r = 10.0$, $\mu_r = 1.0$) and an outer layer of lossy magnetic material ($\epsilon_r = 1.0$, $\mu_r = 1.5 - j2.0$). The thickness of the inner layer is fixed while that for the outer layer is varied	31

FIGURE	PAGE
2.11 Attenuation constants of the EH_{11} mode in a double layer coated waveguide with an inner layer of lossy magnetic material ($\epsilon_r = 1.0, \mu_r = 1.5 - j2.0$) and an outer layer of lossless dielectric material ($\epsilon_r = 10.0, \mu_r = 1.0$). The thickness of the inner layer is fixed while that for the outer layer is varied.....	32
2.12 RCS's of coated and uncoated circular cylinders with diameter 4λ and depth 10λ	33
3.1 Ray bouncing approach to calculating the RCS of a partially open cavity with complex geometry and material loading	36
3.2 Local coordinate system of the first impact point.....	41
3.3 (a) The original curved interface is replaced by its tangent plane at the impact point 1 for calculating the reflection coefficient based on GO. (b) Transmission line analogy of the planar reflection problem in (a).....	43
3.4 Planar approximation for the wavefront of the exit ray tube	51
3.5 Shape of the exit ray tube on the output aperture is obtained by shooting four adjacent rays into the cavity	54
3.6 The area of the output ray tube is related to that of the incident ray tube by the product of the divergence factors	56
3.7 The incident and exit ray positions on the aperture for a circular cylinder with a flat end-plate	58
3.8 The incident and exit ray positions on the aperture for an elliptical cylinder with nonuniform cross section and a flat end-plate.....	59
3.9 Comparison of results for ray bouncing with modal analysis for a circular cylinder with diameter 4λ and depth 2λ . (a) $\phi\phi$ -polarization, (b) $\theta\theta$ -polarization	60
3.10 Comparison of results for ray bouncing with modal analysis for a circular cylinder with diameter 4λ and depth 4λ . (a) $\phi\phi$ -polarization, (b) $\theta\theta$ -polarization.....	61
3.11 Comparison of results for ray bouncing with modal analysis for a circular cylinder with diameter 4λ and depth 10λ . (a) $\phi\phi$ -polarization, (b) $\theta\theta$ -polarization.....	62
3.12 Convergence of the RCS results as the ray density launch is increased. (a) $\theta = 25^\circ$, (b) $\theta = 50^\circ$	64
3.13 RCS of a circular cylinder with diameter 10λ and depth 10λ	65

FIGURE	PAGE
3.14	RCS of a circular cylinder with diameter 20λ and depth 40λ66
4.1	Circular cylinder and S-bend circular cylinder.....70
4.2	Surface with transition from line segment to arc of circle. Circle is centered about $(x,y) = (0,0)$74
4.3	Triangle-to-circle transition waveguide.....75
4.4	Cross-sectional view of transition waveguide at various distances along the axial direction76
4.5	Surface with transition from line segment to arc of circle. Center is offset along the y axis78
4.6	Triangle-to-circle S-bend transition waveguide.....79
4.7	Exit ray pictures for (a) circular cylinder with flat end-plate and (b) S-bend circular cylinder with flat end-plate.....81
4.8	Exit ray pictures for (a) straight triangle-to-circle transition waveguide with flat plate end-plate and (b) S-bend straight triangle-to-circle transition waveguide with flat end-plate82
4.9	Ray path in an S-bend circular cylinder (5λ offset)83
4.10	Ray path in an S-bend circular cylinder (5λ offset)84
4.11	Triangular aperture of transition waveguide. Each point corresponds to input point of ray for Figs. 4.12 - 4.1786
4.12	Ray path in an S-bend triangle-to-circle transition waveguide87
4.13	Ray path in an S-bend triangle-to-circle transition waveguide88
4.14	Ray path in an S-bend triangle-to- circle transition waveguide89
4.15	Ray path in an S-bend triangle-to-circle transition waveguide90
4.16	Ray path in an S-bend triangle-to-circle transition waveguide91
4.17	Ray path in an S-bend triangle-to-circle transition waveguide92
4.18	BCS with different input ray densities for an S-bend cylinder with diameter of 5λ , depth of 10λ , and offset of 2.5λ . Direction of incidence $(\theta_{in}, \phi_{in}) = (10^\circ, -90^\circ)$. (a) $\phi\phi$ -polarization, (b) $\theta\theta$ -polarization93

FIGURE	PAGE
4.19 BCS with different input ray densities for an S-bend cylinder with diameter of 5λ , depth of 10λ , and offset of 5.0λ . Direction of incidence $(\theta_{in}, \phi_{in}) = (10^\circ, -90^\circ)$. (a) $\phi\phi$ -polarization, (b) $\theta\theta$ -polarization	94
4.20 BCS with different input ray densities for a triangle-to-circle transition waveguide with triangle side of 5.4λ , end circle diameter of 4.5λ , and depth of 6.75λ . Direction of incidence $(\theta_{in}, \phi_{in}) = (10^\circ, -90^\circ)$. (a) $\phi\phi$ -polarization, (b) $\theta\theta$ -polarization	95
4.21 BCS with different input ray densities for an S-bend triangle-to-circle transition waveguide with triangle side of 5.4λ , end circle diameter of 4.5λ , depth of 6.75λ , and offset of 4.05λ . Direction of incidence $(\theta_{in}, \phi_{in}) = (10^\circ, -90^\circ)$. (a) $\phi\phi$ -polarization, (b) $\theta\theta$ -polarization	96
4.22 Comparison of RCS's for straight circular cylinder (diameter of 5λ and depth of 10λ) with 2.5λ offset S-bend cylinder (same diameter and depth). (a) $\phi\phi$ -polarization, (b) $\theta\theta$ -polarization	97
4.23 Comparison of RCS's for straight circular cylinder (diameter of 5λ and depth of 10λ) with 5.0λ offset S-bend cylinder (same diameter and depth). (a) $\phi\phi$ -polarization, (b) $\theta\theta$ -polarization.....	98
4.24 Comparison of RCS's for straight circular cylinder (diameter of 5λ and depth of 10λ) with 2.5λ offset S-bend cylinder (same diameter and depth) and same S-bend with coating layer (thickness = 0.1λ , $\epsilon_r = 2.5 - j1.25$, $\mu_r = 1.6 - j0.8$) (a) $\phi\phi$ -polarization, (b) $\theta\theta$ -polarization.....	100
4.25 Comparison of RCS's for triangle-to-circle transition waveguide (triangle side of 5λ , circle diameter of 4.5 , and depth of 4.05λ) with 4.05λ offset S-bend transition waveguide (same aperture, end diameter, and depth) and same S-bend with coating layer (thickness = 0.1λ , $\epsilon_r = 2.5 - j1.25$, $\mu_r = 1.6 - j0.8$) (a) $\phi\phi$ -polarization, (b) $\theta\theta$ -polarization.....	101
5.1 Ray optical picture showing a beam bouncing back and forth in the parallel-plate waveguide	104
5.2 Plane wave incident on a semi-infinite parallel-plate waveguide. The electric field vector is y-directed.....	105

FIGURE	PAGE
5.3 Plots of Poynting vectors inside of a 50λ waveguide based on (a) the intuitive ray picture, (b) the actual fields obtained by summing up modes, and (c) an enlargement of a section of (b).....	108
5.4 Plots of Poynting vectors inside of a 10λ waveguide based on (a) the intuitive ray picture, (b) the actual fields obtained by summing up modes.....	110
5.5 Plots of Poynting vectors inside of a 3λ waveguide based on (a) the intuitive ray picture, (b) the actual fields obtained by summing up modes.....	111
5.6 Plots of Poynting vectors of the actual fields of a 5λ waveguide for various incident angles. (a) $\theta = 0^\circ$, (b) $\theta = 20^\circ$, (c) $\theta = 40^\circ$	112
5.7 Plots of Poynting vectors inside of a 5λ waveguide showing that the beam behavior reemerges after a chaotic region. (a) The intuitive ray picture, (b) the actual fields obtained by summing up modes.....	113

CHAPTER 1

INTRODUCTION

Although the development of radar did not mature until World War II, the study of electromagnetic scattering, the basis of radar, is almost as old as Maxwell's equations themselves. Hertz, experimentally testing the theories of Maxwell in 1886, demonstrated that radio waves could be reflected by metallic and dielectric bodies [1]. Sommerfeld's solution for the half-plane scattering problem [2] appeared in 1896, and Mie's classic paper on the scattering from spheres [3] was published in 1908. In a speech delivered to the Institute of Radio Engineers in 1922 [4], Marconi said:

As was shown by Hertz, the electric waves can be completely reflected by conducting bodies. In some of my tests I have noticed the effects of reflection and detection of these waves by metallic objects miles away.

It seems to me that it should be possible to design apparatus by means of which a ship could radiate or project a divergent beam of these rays in any desired direction, which rays, if coming across a metallic object, such as another steamer or ship, would be reflected back to a receiver screened from the local transmitter on the sending ship, and thereby, immediately reveal the presence and bearing of the other ship in fog or thick weather.

Today, radar is used not only in ship detection applications as Marconi had predicted, but also in air traffic control, remote sensing, satellite detection and tracking, and law enforcement. Additionally, radar has a wide variety of military applications: for surveillance and detection of friendly and hostile planes, ships, tanks, and missiles; for navigation; and for control and guidance of weapons.

With the increasing effectiveness and sophistication of today's military radar systems, the ability to reduce the radar visibility of potential targets has been of importance. There are four basic techniques for reducing the radar cross section (RCS) of a target [5]:

- (i) shaping
- (ii) radar absorbing (or lossy) materials
- (iii) passive cancellation
- (iv) active cancellation.

Of the four methods, shaping and the use of absorbing materials are the most effective. For example, a police radar capable of detecting the large planar surfaces of an Allied moving van (Fig. 1.1(a)) 1.5 miles away could not detect the sleek curved surfaces of a Corvette (Fig. 1.1(b)) 600 feet away [6].

One problem of interest in RCS reduction studies is that of the open-ended cavity [7] - [12]. Coating the interior of the cavity with lossy materials and shaping the cavities have been used in reducing the RCS of cavity structures. This thesis investigates both issues in the study of RCS reduction of arbitrary cavity structures.

In Chapter 2, the effects of interior coating are studied. An open-ended cavity is often modelled as a section of waveguide, open on one end and terminated by a flat conducting plate on the other. A layer or layers of material lining the waveguide wall serve to alter the modal fields in the guide in order to achieve either more or less attenuation for certain modes. With the proper choice of coating material and thickness, a significant RCS reduction can be achieved using only a single thin layer of coating. However, this reduction is only effective over a narrow frequency band at low frequencies ($a/\lambda \sim 1$, where a = radius of the cylinder; λ = the free-space wavelength). A generalized method is presented in this chapter for computing the propagation/attenuation constants for the normal modes of a circular waveguide lined with multiple layers of coating. This method is then applied to multilayered coated structures to show that a greater effectiveness in the attenuation of the normal modes can be achieved over a broadened frequency range.

ORIGINAL PAGE IS
OF POOR QUALITY

(a)



(b)



Fig. 1.1 Comparison of body shapes for (a) Allied moving van, with flat planar surfaces and (b) Chevrolet Corvette, with smooth, sleek curves.

In Chapter 3, the problem of calculating the RCS of an arbitrary cavity is addressed. Traditional methods of analysis for the open-ended cavity include such techniques as the modal analysis used in Chapter 2, finite element and difference methods, and moment methods. However, the aforementioned techniques become impossible if (i) the shape of the cavity is not a perfect sphere or cylinder, (ii) the electrical dimension of the cavity is large, or (iii) the space inside the cavity is not homogeneous. These restrictions prevent the realistic modelling of physical problems and hinder the study of the effects of shaping on RCS. In this chapter, a different strategy for analyzing the open cavity problem, entitled "shooting and bouncing rays" (SBR), is presented. A dense grid of geometric optics (GO) rays representing an incident plane wave is 'shot' into the cavity through the front aperture and followed as the rays bounce from conductors, penetrate through materials, and eventually return to the opening of the cavity. An innovative scheme is then used to integrate the aperture field to obtain the scattered field. This is the first attempt of its kind at solving partially open structures using the ray technique found in the open literature. The SBR method places no restriction on the shape of the cavity and permits the RCS computation for any arbitrarily shaped cavity.

Chapter 4 studies the effectiveness of shaping as an RCS reduction method. The SBR method is used to study the RCS of uniform and nonuniform cylindrical cavities. For a large (relative to wavelength) flat-plate terminated cylinder, there is a large RCS value at near axial incidence due to the reflection from the termination. The near axial RCS of such structures can be reduced by a smooth gradual bending of the cylindrical axis. This chapter shows the reduction of RCS achieved by applying a longitudinal S-bend to a circular waveguide and a triangle-to-circle transition waveguide. The SBR method is currently the only available viable method for computing the RCS for such geometries.

The range of validity of the SBR method is investigated in Chapter 5. The limitations of SBR are studied by considering the problem of a plane wave impinging on a semi-infinite

parallel-plate waveguide. Two alternative descriptions for the fields propagating in the waveguide are the modal analysis and GO ray analysis, used by the SBR method. A graphical comparison is made of the two field descriptions for the parallel-plate waveguide. This is believed to be the first graphical display showing the interplay between the two alternative descriptions of the fields. Though the simple model of the parallel-plate waveguide was chosen because it best demonstrates the ray - mode equivalence, the results extend to other waveguide and cavity structures. It is demonstrated that for a waveguide separation large compared to wavelength, the ray and modal descriptions are in good agreement.

Finally, the conclusions and some future work evolving from this thesis are discussed in Chapter 6.

CHAPTER 2

MODAL ATTENUATION IN MULTILAYERED COATED WAVEGUIDES

2.1 Introduction

One method used in reducing the RCS of cavity structures is to coat the interior of the cavity with lossy dielectric or magnetic materials. Previous studies [13],[14] on the effects of coating involve modelling the cavity as a coated circular cylindrical waveguide terminated by a perfect electric conducting (PEC) short and studying the propagation and attenuation properties of the normal modes of the waveguide. There are also many other applications in which it is desirable to line the wall of a conventional waveguide with a layer of coating material [15]-[20]. The lining serves to alter the modal fields in the waveguide in order to achieve either more or less attenuation for certain modes.

Pathak and Altintas [21] showed that the interior irradiation contribution to the RCS of a shorted waveguide is due mainly to a few low-order normal modes. By attenuating low-order modes, a lossy lining layer serves as a mode suppressor, which then reduces the RCS of the cavity. Lee et al. [14] studied the normal mode behavior for a circular waveguide lined with a single layer of coating. It was shown that at low frequencies ($a/\lambda \sim 1$, where a = radius of the cylinder; λ = the free-space wavelength) for a slightly lossy coating layer, the low-order modes can be highly attenuated with a single thin layer of coating. As the frequency increases, however, the attenuation constants of most of the low-order modes become small and decrease as a function of λ^2/a^3 . Thus, RCS reduction can be achieved only over a fairly narrow frequency range with a single layer of coating. This chapter studies the propagation/attenuation constants of the low-order modes in a waveguide lined with multiple layers of coating. By using two or more layers of coating material, the fields inside the waveguide can be more easily manipulated to achieve a greater region of attenuation. With multilayered coating, it is possible

to achieve larger attenuation constants over a broader frequency range than with a single layer of coating.

Past studies of coated waveguides have included such methods as perturbation theory [16],[17],[19], transmission-line model [15]-[18], and asymptotic theory [20]. These methods often require simplifying assumptions that are too restrictive, such as the coating material must be nearly lossless [16]-[18] or very lossy [20]. This treatment will apply the more general method of solving the modal characteristic equation exactly by a numerical method. This is feasible because of the fast computational speed of modern computers and the availability of efficient subroutines for computing Bessel functions with complex arguments.

In Sec. 2.2, an overview of the modal fields in a coated circular waveguide is given. The mathematical formulation for the exact characteristic equation of the normal modes for a circular waveguide with multiple layers of internal coating is presented in Sec. 2.3. The conventional method involves setting the determinant of a $4n \times 4n$ matrix equal to 0, where n is the number of coating layers. The propagation constants of the normal modes are the solutions of the characteristic equation. As the number of layers increases, this method becomes cumbersome due to the large size of the matrices involved. In addition, the characteristic equation, a transcendental equation involving Bessel functions, must be solved numerically on a computer. Different programs must be written for different numbers of coating layers. A generalized method for formulating the characteristic equation is presented which involves only the manipulation of 4×4 matrices. This method allows for a computer implementation which permits any arbitrary number of coating layers. Numerical results for the attenuation properties of the normal modes of circular waveguides with single and multiple layers of coating are presented in Sec. 2.4.

2.2 Overview of Modal Fields in a Coated Circular Waveguide

A coated cylindrical waveguide is shown in Fig. 2.1. The problem of interest is the propagation/attenuation properties of the normal modes of such a structure. Figure 2.2 shows an exaggerated view of the coating layers for the sake of illustrating the geometrical features of the guide. In the application, the coating layers will be very thin relative to the diameter of the guide. The waveguide walls are assumed to be perfectly conducting, and each coating layer is assumed to be of uniform thickness. The axis of the cylinder coincides with the z axis. Both the permittivity ϵ_i and permeability μ_i of each coating layer are allowed to be complex. The characteristic equation for the propagation constant k_z of the normal modes is derived from the well-known method of seeking nontrivial solutions for the coefficients of the field expressions of the equations obtained by enforcing the continuity of the four tangential fields, H_z , E_z , H_ϕ , E_ϕ , at each interface between two coating layers, and between the innermost coating layer and the inner region [22].

In an uncoated waveguide, the normal modes are either TE_{mn} or TM_{mn} with respect to the longitudinal axis z . The index m describes the azimuthal variation in the form of $\sin m\phi$ or $\cos m\phi$. Here, the index n describes the order of the eigenvalues of $J_m(k_\rho a) = 0$ for TM and $J'_m(k_\rho a) = 0$ for TE, where J_m is the Bessel function of order m . (Note that variable n is also used to represent the number of coating layers. The intended meaning of subsequent uses of n should be clear from its context.) With the exception of the $m = 0$ case, the normal modes are no longer pure TE or TM when the waveguide is coated with dielectric or magnetic material. The modes are commonly classified into HE_{mn} and EH_{mn} in such a way that in the limiting case of a vanishing thin coating [23]

$$HE_{mn} \rightarrow TE_{mn}, \quad \text{and} \quad EH_{mn} \rightarrow TM_{mn}. \quad (2.1)$$

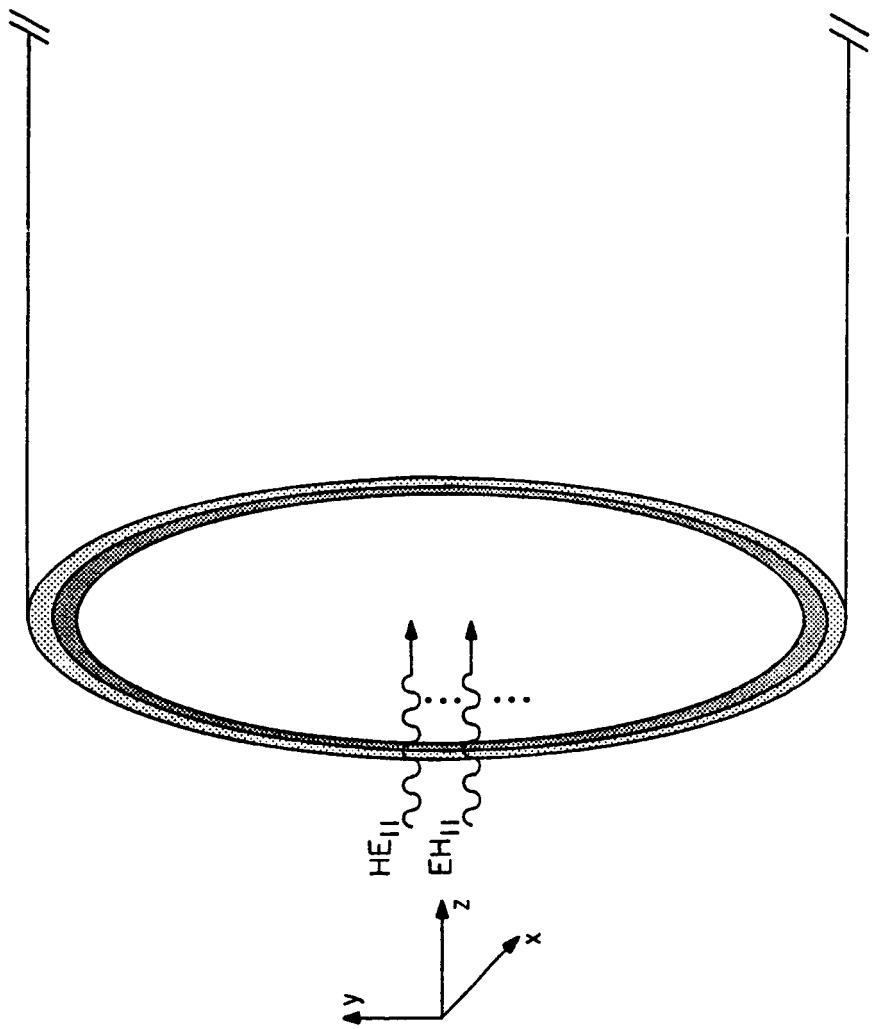


Fig. 2.1 A coated circular waveguide.

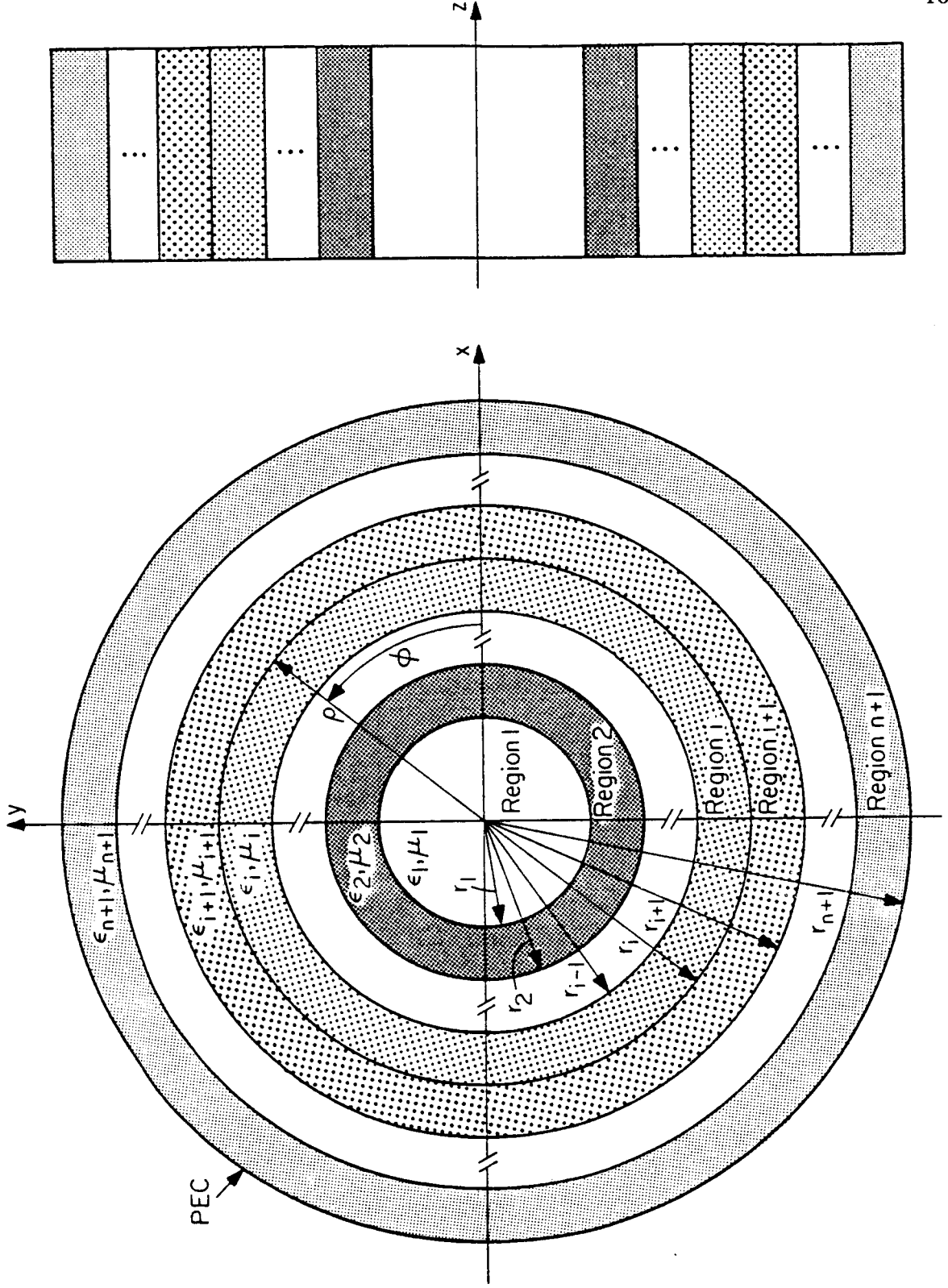


Fig. 2.2 Exaggerated cross-sectional view of multilayered coated waveguide.

The modal fields for the waveguide are given by

$$E_{\rho}^1 = \left[-A_1 \frac{k_z k_{\rho_1}}{\omega \epsilon_1} F_1'(\rho) - A_2 \frac{m}{\rho} F_1(\rho) \right] \cos m\phi$$

$$E_{\rho}^i = \left[-B_1^i \frac{k_z k_{\rho_i}}{\omega \epsilon_i} F_i'(\rho) - B_2^i \frac{k_z k_{\rho_i}}{\omega \epsilon_i} G_i'(\rho) - B_3^i \frac{m}{\rho} F_i(\rho) - B_4^i \frac{m}{\rho} G_i(\rho) \right] \cos m\phi$$

$$E_{\rho}^{n+1} = \left[-C_1 \frac{k_z k_{\rho_{n+1}}}{\omega \epsilon_{n+1}} K_1'(\rho) - C_2 \frac{m}{\rho} K_2(\rho) \right] \cos m\phi$$

$$E_{\phi}^1 = \left[-A_1 \frac{k_z m}{\omega \epsilon_1 \rho} F_1(\rho) - A_2 k_{\rho_1} F_1'(\rho) \right] \sin m\phi$$

$$E_{\phi}^i = \left[-B_1^i \frac{k_z m}{\omega \epsilon_i \rho} F_i(\rho) - B_2^i \frac{k_z m}{\omega \epsilon_i \rho} G_i(\rho) - B_3^i k_{\rho_i} F_i'(\rho) - B_4^i k_{\rho_i} G_i'(\rho) \right] \sin m\phi$$

$$E_{\phi}^{n+1} = \left[-C_1 \frac{k_z m}{\omega \epsilon_{n+1} \rho} K_1(\rho) - C_2 k_{\rho_{n+1}} K_2'(\rho) \right] \sin m\phi$$

$$E_z^1 = A_1 \frac{k_{\rho_1}^2}{j\omega \epsilon_1} F_1(\rho) \cos m\phi$$

$$E_z^i = \left[B_1^i \frac{k_{\rho_i}^2}{j\omega \epsilon_i} F_i(\rho) + B_2^i \frac{k_{\rho_i}^2}{j\omega \epsilon_i} G_i(\rho) \right] \cos m\phi$$

$$E_z^{n+1} = C_1 \frac{k_{\rho_{n+1}}^2}{j\omega \epsilon_{n+1}} K_1(\rho) \cos m\phi$$

$$H_{\rho}^1 = \left[-A_1 \frac{m}{\rho} F_1(\rho) - A_2 \frac{k_z k_{\rho_1}}{\omega \mu_1} F_1'(\rho) \right] \sin m\phi$$

$$H_{\rho}^i = \left[-B_1^i \frac{m}{\rho} F_i(\rho) - B_2^i \frac{m}{\rho} G_i(\rho) - B_3^i \frac{k_z k_{\rho_i}}{\omega \mu_i} F_i'(\rho) - B_4^i \frac{k_z k_{\rho_i}}{\omega \mu_i} G_i'(\rho) \right] \sin m\phi$$

$$H_{\rho}^{n+1} = \left[-C_1 \frac{k_z m}{\omega \mu_{n+1} \rho} K_1(\rho) - C_2 \frac{k_z k_{\rho_{n+1}}}{\omega \mu_{n+1}} K_2'(\rho) \right] \sin m\phi$$

$$H_{\phi}^1 = \left[-A_1 k_{\rho_1} F_1'(\rho) - A_2 \frac{k_z m}{\omega \mu_1 \rho} F_1(\rho) \right] \cos m\phi$$

$$H_{\phi}^i = \left[-B_1^i k_{\rho_i} F_i'(\rho) - B_2^i k_{\rho_i} G_i'(\rho) - B_3^i \frac{k_z m}{\omega \mu_i \rho} F_i(\rho) - B_4^i \frac{k_z m}{\omega \mu_i \rho} G_i(\rho) \right] \cos m\phi$$

$$H_{\phi}^{n+1} = \left[-C_1 k_{\rho_{n+1}} K_1'(\rho) - C_2 \frac{k_z m}{\omega \mu_{n+1} \rho} K_2(\rho) \right] \cos m\phi$$

$$H_z^1 = A_2 \frac{k_{\rho_1}^2}{j\omega \mu_1} F_1(\rho) \cos m\phi$$

$$H_z^i = \left[B_3^i \frac{k_{\rho_i}^2}{j\omega \mu_i} F_i(\rho) + B_4^i \frac{k_{\rho_i}^2}{j\omega \mu_i} G_i(\rho) \right] \cos m\phi$$

$$H_z^{n+1} = C_1 \frac{k_{\rho_{n+1}}^2}{j\omega \mu_{n+1}} K_2(\rho) \cos m\phi$$

where

$$F_i(\rho) = J_m(k_{\rho_i} \rho)$$

$$F_i'(\rho) = J_m'(k_{\rho_i} \rho)$$

$$G_i(\rho) = N_m(k_{\rho_i} \rho)$$

$$G_i'(\rho) = N_m'(k_{\rho_i} \rho)$$

$$K_1(\rho) = J_m(k_{\rho_{n+1}} \rho) N_m(k_{\rho_{n+1}} r_{n+1}) - N_m(k_{\rho_{n+1}} \rho) J_m(k_{\rho_{n+1}} r_{n+1})$$

$$K_1'(\rho) = J_m'(k_{\rho_{n+1}} \rho) N_m(k_{\rho_{n+1}} r_{n+1}) - N_m'(k_{\rho_{n+1}} \rho) J_m(k_{\rho_{n+1}} r_{n+1})$$

$$K_2(\rho) = J_m(k_{\rho_{n+1}} \rho) N_m'(k_{\rho_{n+1}} r_{n+1}) - N_m(k_{\rho_{n+1}} \rho) J_m'(k_{\rho_{n+1}} r_{n+1})$$

$$K_2'(\rho) = J_m'(k_{\rho_{n+1}} \rho) N_m'(k_{\rho_{n+1}} r_{n+1}) - N_m(k_{\rho_{n+1}} \rho) J_m'(k_{\rho_{n+1}} r_{n+1}) \quad (2.2)$$

The convention of $\exp[j(\omega t - k_z z)]$ is understood and suppressed. Superscript 1 represents the inner region; superscript $n+1$ represents the layer of coating on the conducting wall; and superscript i represents the i^{th} region, where $2 \leq i \leq n$. Subscripts ρ , ϕ , and z indicate the radial, angular, and propagation-directional components of the fields, respectively.

k_{ρ_i} represents the radial wave vector in region i , where $k_{\rho_i}^2 + k_z^2 = \epsilon_i \mu_i k_0^2$ and $k_0 = 2\pi/\lambda$; ω is the angular frequency; J_m is the Bessel function and N_m is the Neumann function of order m . $A_1, A_2, B^i_1, B^i_2, B^i_3, B^i_4, C_1$, and C_2 are the constants, which are determined by the boundary conditions and normalization requirements. Due to circular symmetry, there are two degenerate modes for each angular mode index except for $m = 0$. One of the two degenerate modes is arbitrarily chosen in the above expressions.

2.3 Characteristic Equation of the Normal Modes

For the case of a single layer of coating, the characteristic equation for the propagation constant k_z of a normal mode is well known [22] and given by

$$k_{\rho_1}^2 \left[F_1'(a) - \epsilon_2 \frac{F_1(a) K_1'(a) \frac{k_{\rho_1}}{k_{\rho_2}}}{K_1(a)} \right] \left[F_1'(a) - \mu_2 \frac{F_1(a) K_2'(a) \frac{k_{\rho_1}}{k_{\rho_2}}}{K_2(a)} \right] - \left[\frac{k_z m}{(k_0 a)} \right]^2 F_1^2(a) \left[1 - \left(\frac{k_{\rho_1}}{k_{\rho_2}} \right)^2 \right]^2 = 0 \quad (2.3)$$

where $a = r_1$

$b = r_2$

$$k_{\rho_1}^2 + k_z^2 = k_0^2$$

$$k_{\rho_2}^2 + k_z^2 = \epsilon_2 \mu_2 k_0^2.$$

For a double layer of coating, the characteristic equation for the propagation constant k_z of the modal fields is given by the 8×8 matrix equation

$$\det \begin{bmatrix} \frac{k_{p_1}^2}{\epsilon_1} F_1(a) & 0 & \frac{-k_{p_2}^2}{\epsilon_2} F_2(a) & \frac{-k_{p_2}^2}{\epsilon_2} G_2(a) & 0 & 0 & 0 & 0 \\ 0 & 0 & \frac{k_{p_2}^2}{\epsilon_2} F_2(b) & \frac{k_{p_2}^2}{\epsilon_2} G_2(b) & 0 & 0 & \frac{-k_{p_3}^2}{\epsilon_3} K_1(b) & 0 \\ 0 & \frac{k_{p_1}^2}{\mu_1} F_1(a) & 0 & 0 & \frac{-k_{p_2}^2}{\mu_2} F_2(a) & \frac{-k_{p_2}^2}{\mu_2} G_2(a) & 0 & 0 \\ 0 & 0 & 0 & 0 & \frac{k_{p_2}^2}{\mu_2} F_2(b) & \frac{k_{p_2}^2}{\mu_2} G_2(b) & 0 & \frac{-k_{p_3}^2}{\mu_3} K_2(b) \\ k_{p_1} F_1(a) & \frac{k_z m}{\omega a} \frac{1}{\mu_1} F_1(a) & -k_{p_2} F_2(a) & -k_{p_2} G_2(a) & \frac{-k_z m}{\omega a} \frac{1}{\mu_2} F_2(a) & \frac{-k_z m}{\omega a} \frac{1}{\mu_2} G_2(a) & 0 & 0 \\ 0 & 0 & k_{p_2} F_2(b) & k_{p_2} G_2(b) & \frac{k_z m}{\omega b} \frac{1}{\mu_2} F_2(b) & \frac{k_z m}{\omega b} \frac{1}{\mu_2} G_2(b) & -k_{p_3} K_1(b) & \frac{-k_z m}{\omega b} \frac{1}{\mu_3} K_2(b) \\ \frac{k_z m}{\omega a} \frac{1}{\epsilon_1} F_1(a) & k_{p_1} F_1(a) & \frac{-k_z m}{\omega a} \frac{1}{\epsilon_2} F_2(a) & \frac{-k_z m}{\omega a} \frac{1}{\epsilon_2} G_2(a) & -k_{p_2} F_2(a) & -k_{p_2} G_2(a) & 0 & 0 \\ 0 & 0 & \frac{k_z m}{\omega b} \frac{1}{\epsilon_2} F_2(b) & \frac{k_z m}{\omega b} \frac{1}{\epsilon_2} G_2(b) & k_{p_2} F_2(b) & k_{p_2} G_2(b) & \frac{-k_z m}{\omega b} \frac{1}{\epsilon_3} K_1(b) & -k_{p_3} K_2(b) \end{bmatrix} = 0$$

where $a = r_1$, $b = r_2$, and $c = r_3$. (2.4)

In general, for n layers of coating, the characteristic equation for k_z is given by a $4n \times 4n$ matrix equation. In numerically solving the equation, the computer time required becomes cumbersome as the number of layers increases. An efficient method for formulating the characteristic equation [24] for an arbitrary amount of layers can be utilized which involves only the manipulation of 4×4 matrices.

The boundary matching equations at each media interface can be written as 4 x 4 matrix equations. At $\rho = r_1$ (boundary between region 1, center region, and region 2, innermost layer),

$$\begin{bmatrix} \frac{k_{\rho_1}^2}{\epsilon_1} F_1(r_1) & 0 & 0 & 0 \\ 0 & \frac{k_{\rho_1}^2}{\mu_1} F_1(r_1) & 0 & 0 \\ k_{\rho_1} F_1'(r_1) & \frac{k_z m}{\omega r_1} \frac{1}{\mu_1} F_1(r_1) & 0 & 0 \\ \frac{k_z m}{\omega r_1} \frac{1}{\epsilon_1} F_1(r_1) & k_{\rho_1} F_1'(r_1) & 0 & 0 \end{bmatrix} \begin{bmatrix} A_1 \\ A_2 \\ 0 \\ 0 \end{bmatrix} = \begin{bmatrix} \frac{k_{\rho_2}^2}{\epsilon_2} F_2(r_1) & \frac{k_{\rho_2}^2}{\epsilon_2} G_2(r_1) & 0 & 0 \\ 0 & 0 & \frac{k_{\rho_2}^2}{\mu_2} F_2(r_1) & \frac{k_{\rho_2}^2}{\mu_2} G_2(r_1) \\ k_{\rho_2} F_2'(r_1) & k_{\rho_2} G_2'(r_1) & \frac{k_z m}{\omega r_1} \frac{1}{\mu_2} F_2(r_1) & \frac{k_z m}{\omega r_1} \frac{1}{\mu_2} G_2(r_1) \\ \frac{k_z m}{\omega r_1} \frac{1}{\epsilon_2} F_2(r_1) & \frac{k_z m}{\omega r_1} \frac{1}{\epsilon_2} G_2(r_1) & k_{\rho_2} F_2'(r_1) & k_{\rho_2} G_2'(r_1) \end{bmatrix} \begin{bmatrix} B_1^2 \\ B_2^2 \\ B_3^2 \\ B_4^2 \end{bmatrix} \quad (2.5)$$

At $\rho = r_i, 2 \leq i \leq n - 1$ (boundary between region i and $i + 1$),

$$\begin{bmatrix} \frac{k_{\rho_i}^2}{\epsilon_i} F_i(r_i) & \frac{k_{\rho_i}^2}{\epsilon_i} G_i(r_i) & 0 & 0 \\ 0 & 0 & \frac{k_{\rho_i}^2}{\mu_i} F_i(r_i) & \frac{k_{\rho_i}^2}{\mu_i} G_i(r_i) \\ k_{\rho_i} F_i'(r_i) & k_{\rho_i} G_i'(r_i) & \frac{k_z m}{\omega r_i} \frac{1}{\mu_i} F_i(r_i) & \frac{k_z m}{\omega r_i} \frac{1}{\mu_i} G_i(r_i) \\ \frac{k_z m}{\omega r_i} \frac{1}{\epsilon_i} F_i(r_i) & \frac{k_z m}{\omega r_i} \frac{1}{\epsilon_i} G_i(r_i) & k_{\rho_i} F_i'(r_i) & k_{\rho_i} G_i'(r_i) \end{bmatrix} \begin{bmatrix} B_1^i \\ B_2^i \\ B_3^i \\ B_4^i \end{bmatrix}$$

$$= \begin{bmatrix} \frac{k_{\rho_i}^2}{\epsilon_{i+1}} F_{i+1}(r_i) & \frac{k_{\rho_i}^2}{\epsilon_{i+1}} G_{i+1}(r_i) & 0 & 0 \\ 0 & 0 & \frac{k_{\rho_i}^2}{\mu_{i+1}} F_{i+1}(r_i) & \frac{k_{\rho_i}^2}{\mu_{i+1}} G_{i+1}(r_i) \\ k_{\rho_i} F_{i+1}'(r_i) & k_{\rho_i} G_{i+1}'(r_i) & \frac{k_z m}{\omega r_i} \frac{1}{\mu_{i+1}} F_{i+1}(r_i) & \frac{k_z m}{\omega r_i} \frac{1}{\mu_{i+1}} G_{i+1}(r_i) \\ \frac{k_z m}{\omega r_i} \frac{1}{\epsilon_{i+1}} F_{i+1}(r_i) & \frac{k_z m}{\omega r_i} \frac{1}{\epsilon_{i+1}} G_{i+1}(r_i) & k_{\rho_i} F_{i+1}'(r_i) & k_{\rho_i} G_{i+1}'(r_i) \end{bmatrix} \begin{bmatrix} B_1^{i+1} \\ B_2^{i+1} \\ B_3^{i+1} \\ B_4^{i+1} \end{bmatrix}$$

(2.6)

At $\rho = r_n$ (boundary between two most outermost layers),

$$\begin{bmatrix} \frac{k_{\rho_n}^2}{\epsilon_n} F_n(r_n) & \frac{k_{\rho_n}^2}{\epsilon_n} G_n(r_n) & 0 & 0 \\ 0 & 0 & \frac{k_{\rho_n}^2}{\mu_n} F_n(r_n) & \frac{k_{\rho_n}^2}{\mu_n} G_n(r_n) \\ k_{\rho_n} F_n'(r_n) & k_{\rho_n} G_n'(r_n) & \frac{k_z m}{\omega r_n} \frac{1}{\mu_n} F_n(r_n) & \frac{k_z m}{\omega r_n} \frac{1}{\mu_n} G_n(r_n) \\ \frac{k_z m}{\omega r_n} \frac{1}{\epsilon_n} F_n(r_n) & \frac{k_z m}{\omega r_n} \frac{1}{\epsilon_n} G_n(r_n) & k_{\rho_1} F_n'(r_n) & k_{\rho_1} G_n'(r_n) \end{bmatrix} \begin{bmatrix} B_1^n \\ B_2^n \\ B_3^n \\ B_4^n \end{bmatrix}$$

$$= \begin{bmatrix} \frac{k_{\rho_{n+1}}^2}{\epsilon_{n+1}} K_1(r_n) & 0 & 0 & 0 \\ 0 & \frac{k_{\rho_{n+1}}^2}{\mu_{n+1}} K_2(r_n) & 0 & 0 \\ k_{\rho_{n+1}} K_1'(r_n) & \frac{k_z m}{\omega r_n} \frac{1}{\mu_{n+1}} K_2(r_n) & 0 & 0 \\ \frac{k_z m}{\omega r_n} \frac{1}{\epsilon_{n+1}} K_1(r_n) & k_{\rho_{n+1}} K_2'(r_n) & 0 & 0 \end{bmatrix} \begin{bmatrix} C_1 \\ C_2 \\ 0 \\ 0 \end{bmatrix}$$

(2.7)

The boundary matching equations thus become n matrix equations for n layers of coating:

$$\begin{aligned}
 \mathbf{M}_{11} \mathbf{A} &= \mathbf{M}_{21} \mathbf{B} \\
 \mathbf{M}_{22} \mathbf{B} &= \mathbf{M}_{32} \mathbf{B} \\
 &\cdot \\
 &\cdot \\
 &\cdot \\
 \mathbf{M}_{nn} \mathbf{B} &= \mathbf{M}_{(n+1)n} \mathbf{C}.
 \end{aligned} \tag{2.8}$$

\mathbf{M}_{ab} refers to the matrix resulting from the tangential fields in region a matched at boundary r_b .

A is then related to C by

$$\mathbf{M}_{11} \mathbf{A} = \mathbf{M}_{21} \mathbf{M}_{22}^{-1} \dots \mathbf{M}_{nn}^{-1} \mathbf{M}_{(n+1)n} \mathbf{C} \tag{2.9}$$

or $\mathbf{M}_{11} \mathbf{A} = \mathbf{M} \mathbf{C}$

where $\mathbf{M} = \mathbf{M}_{21} \mathbf{M}_{22}^{-1} \dots \mathbf{M}_{nn}^{-1} \mathbf{M}_{(n+1)n}$.

Because the last two columns of $\mathbf{M}_{(n+1)n}$ are zero vectors, the last two columns of \mathbf{M} will also be zero vectors. Therefore, \mathbf{M} will be in form

$$\mathbf{M} = \begin{bmatrix} m_{11} & m_{12} & 0 & 0 \\ m_{21} & m_{22} & 0 & 0 \\ m_{31} & m_{32} & 0 & 0 \\ m_{41} & m_{42} & 0 & 0 \end{bmatrix}. \tag{2.10}$$

Equation (2.9) written out is then

$$\begin{bmatrix} \frac{k_{\rho_1}^2}{\epsilon_1} F_1(r_1) & 0 & 0 & 0 \\ 0 & \frac{k_{\rho_1}^2}{\mu_1} F_1(r_1) & 0 & 0 \\ k_{\rho_1} F'_1(r_1) & \frac{k_z m}{\omega r_1} \frac{1}{\epsilon_1} F_1(r_1) & 0 & 0 \\ \frac{k_z m}{\omega r_1} \frac{1}{\epsilon_1} F_1(r_1) & k_{\rho_1} F'_1(r_1) & 0 & 0 \end{bmatrix} \begin{bmatrix} A_1 \\ A_2 \\ 0 \\ 0 \end{bmatrix} = \begin{bmatrix} m_{11} & m_{12} & 0 & 0 \\ m_{21} & m_{22} & 0 & 0 \\ m_{31} & m_{32} & 0 & 0 \\ m_{41} & m_{42} & 0 & 0 \end{bmatrix} \begin{bmatrix} C_1 \\ C_2 \\ 0 \\ 0 \end{bmatrix} \quad (2.11)$$

which can be rewritten as

$$\begin{bmatrix} \frac{k_{\rho_1}^2}{\epsilon_1} F_1(r_1) & 0 & -m_{11} & -m_{12} \\ 0 & \frac{k_{\rho_1}^2}{\mu_1} F_1(r_1) & -m_{21} & -m_{22} \\ k_{\rho_1} F'_1(r_1) & \frac{k_z m}{\omega r_1} \frac{1}{\epsilon_1} F_1(r_1) & -m_{31} & -m_{32} \\ \frac{k_z m}{\omega r_1} \frac{1}{\epsilon_1} F_1(r_1) & k_{\rho_1} F'_1(r_1) & -m_{41} & -m_{42} \end{bmatrix} \begin{bmatrix} A_1 \\ A_2 \\ C_1 \\ C_2 \end{bmatrix} = 0 \quad (2.12)$$

A_1 , A_2 , and C_1 , C_2 fully define the fields in the inner region and outermost layer, respectively. The characteristic equation for the propagation constant k_z is then given by the

determinant of the 4 x 4 matrix M_{AC} set equal to zero, where M_{AC} is the 4 x 4 matrix in (2.12).

$$\det M_{AC} = \det \begin{bmatrix} \frac{k_{p_1}^2}{\epsilon_1} F_1(r_1) & 0 & -m_{11} & -m_{12} \\ 0 & \frac{k_{p_1}^2}{\mu_1} F_1(r_1) & -m_{21} & -m_{22} \\ k_{p_1} F_1'(r_1) & \frac{k_z m_1}{\omega r_1 \epsilon_1} F_1(r_1) & -m_{31} & -m_{32} \\ \frac{k_z m_1}{\omega r_1 \epsilon_1} F_1(r_1) & k_{p_1} F_1'(r_1) & -m_{41} & -m_{42} \end{bmatrix} = 0 \quad (2.13)$$

To summarize, the boundary field matching equations can be expressed in the form of 4 x 4 matrix equations (2.5), (2.6), and (2.7). From these relations, the coefficients for the fields in the center uncoated region can be shown to be related to the coefficients in the outermost coating layer by (2.9), which can be expressed as (2.12). Finally, for nontrivial solutions of the modal fields, the 4 x 4 matrix in (2.12) must be singular. Thus, the characteristic equation for the propagation constants of the normal modes is given by (2.13).

All manipulations now involve only the inversion and multiplication of 4 x 4 matrices. Using this formulation, a computer program to compute the propagation constant k_z for any arbitrary number of coating layers can be written. The final expression (2.13), a complex transcendental equation, can be solved numerically, using, for example, Müller's method (available as an International Mathematical Statistical Libraries subroutine).

2.4 Numerical Results

The attenuation constant α of a normal mode in a coated waveguide is related to the magnetic and electric energies in the coated regions, $|H|^2$ and $|E|^2$, by

$$\alpha \propto \int_V [\text{Im } |\mu|^2 |H|^2 + \text{Im } |\epsilon|^2 |E|^2] dV \quad (2.14)$$

where the volume of integration is over the coated region [22]. Because of the boundary condition of the PEC waveguide wall, the magnetic energy of an empty waveguide is much larger than the electric energy near the surface. Since the fields of the waveguide are not perturbed significantly by a coating layer in the low frequency region, a lossy and magnetic coating material is effective in reducing the RCS of a coated waveguide. Lee and Lee [12] theoretically predicted and experimentally verified a 20 dBSM reduction for a PEC-terminated waveguide ($a/\lambda = 0.98$) lined with a lossy magnetic coating material only 1.18% radii thick. As such, the numerical results presented will focus on coating configurations involving magnetic layers.

The attenuation properties of the two dominant low-order modes for near axial-incidence RCS, the HE_{11} and EH_{11} modes, will be discussed for single- and double-layer coating schemes. The interior uncoated region is taken to be free space ($\epsilon = \epsilon_0$, $\mu = \mu_0$) in all cases. The transverse field distributions for the two modes are shown in Fig. 2.3 for (a) empty guide, (b) lossless dielectric coated guide near cutoff, (c) lossless magnetic coated guide near cutoff, and (d) lossless coated guide in the high frequency limit.

2.4.1 Review of single-layer coating results

With a layer of lossy coating material, the low-order modes of a circular waveguide become inner modes [14] as a/λ increases. The field distribution for such modes is confined mostly in the center region. The fields decay very rapidly from the coating interface to the

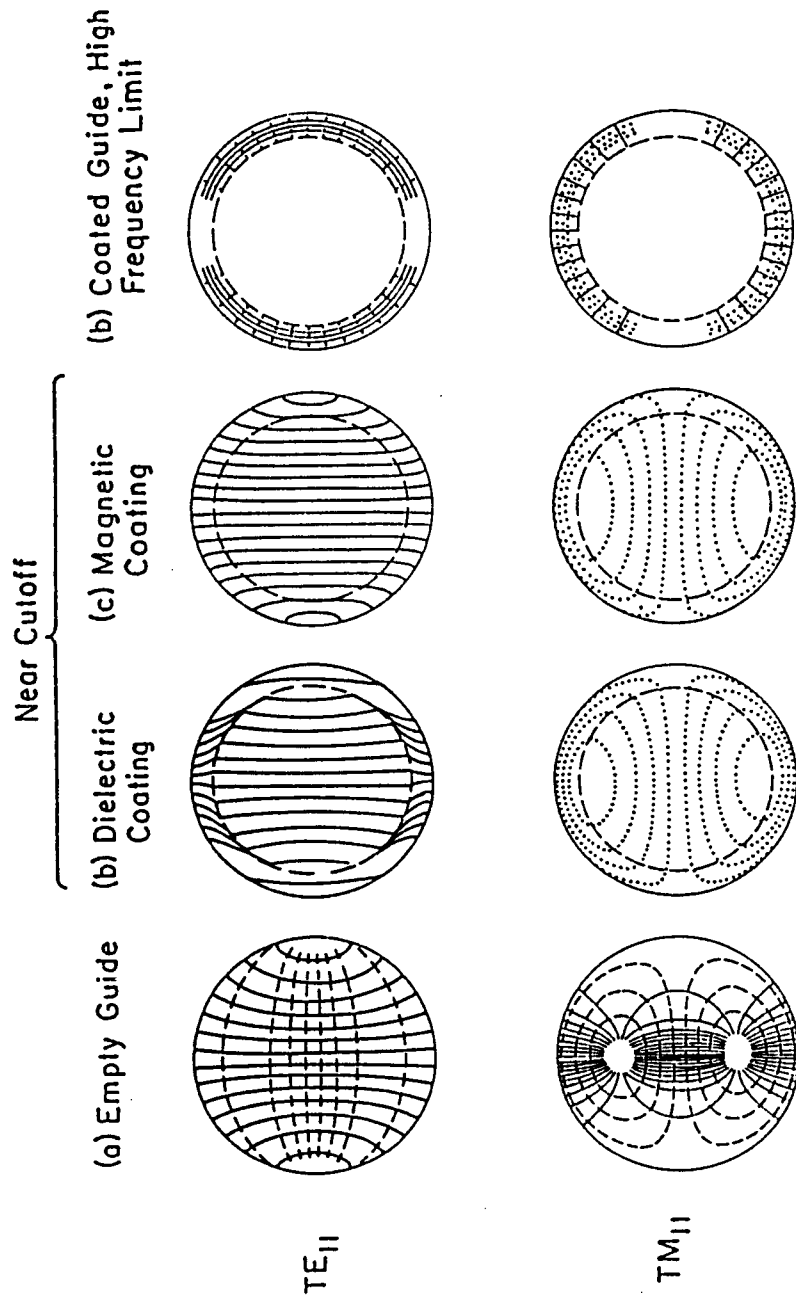


Fig. 2.3 Transverse field distributions of the normal modes in a) empty waveguide b) dielectric coated waveguide ($\epsilon_r = 10.0, \mu_r = 1.0$) at cutoff frequencies c) magnetic coated waveguide ($\epsilon_r = 1.0, \mu_r = 10.0$) at cutoff frequencies, and d) coated waveguide at the high frequency limit.

lossy layer, and the attenuation constants are small. Figures 2.4 - 2.6 show the attenuation constants as a function of increasing frequency for the HE_{11} and EH_{11} , as well as the HE_{12} , modes in a lossy magnetic ($\mu_r = 1.5 - j2.0$) coated waveguide. As the frequency increases, the lossy material tends to expel the fields from the coating region. The attenuation constants decrease as a function of λ^2/a^3 for large frequencies [14].

If the coating material is lossless, however, the modal power distribution is largely concentrated in the coating region. A layer of high dielectric constant tends to "pull" the fields into the coating region as the frequency increases. As shown in Fig. 2.7, although the dielectric layer ($\epsilon_r = 10.0$) covers only 12 percent of the waveguide cross section, 99 percent of the power is confined in the dielectric layer. These results suggest that by using a double layer of coating consisting of a lossy layer and a lossless layer with a large permittivity, the high attenuation region of some of the modes of the waveguide can be extended. A high field concentration would be attracted by the lossless dielectric layer into the coating region, and attenuated by the lossy layer. In the following multilayered coating results, the lossless dielectric layer will have $\epsilon_r = 10.0$, and the lossy magnetic layer will have $\mu_r = 1.5 - j2.0$.

2.4.2 Multilayered coating

Figures 2.8 and 2.9 show the TE_{11} attenuation constant as a function of increasing frequency for a lossless dielectric layer sandwiched between the waveguide wall and a lossy magnetic layer. Figure 2.8 shows a family of curves for a fixed thickness of lossy material and varying thicknesses of lossy dielectric material. As the dielectric layer increases in thickness, a greater amount of the field energy will be concentrated in this layer. This also causes more of the field to be within the lossy layer, resulting in greater attenuation. Note that there is a significant increase in both the level of attenuation and the frequency band of high attenuation.

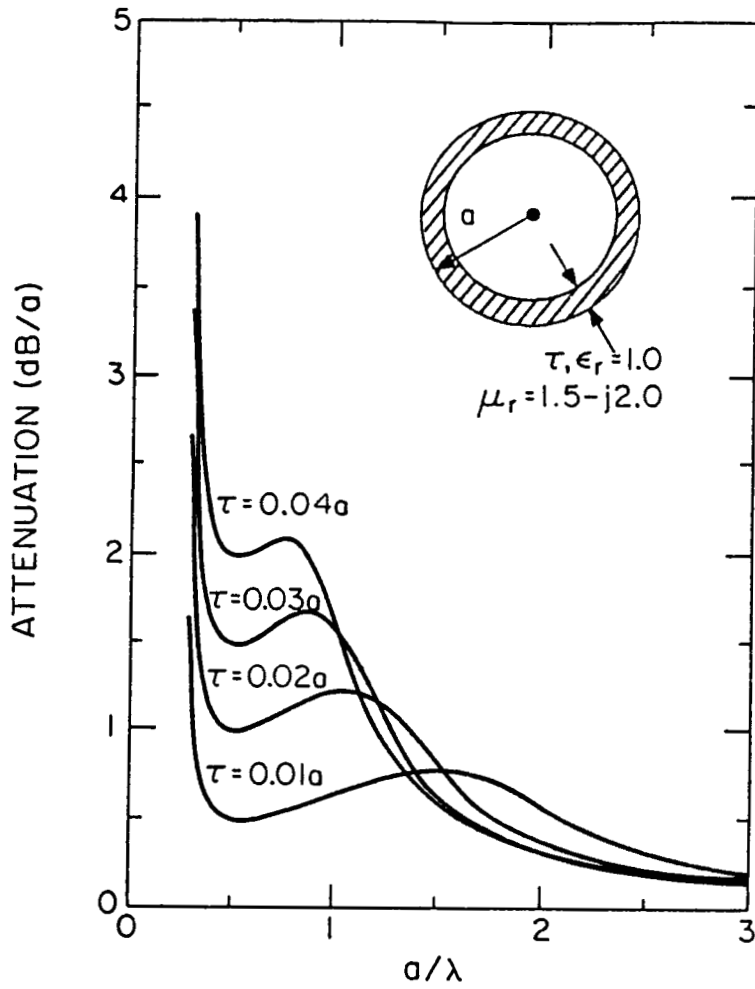


Fig. 2.4 Attenuation constants of the HE_{11} mode in a lossy magnetic coated waveguide ($\epsilon_r = 1.0$, $\mu_r = 1.5 - j2.0$).

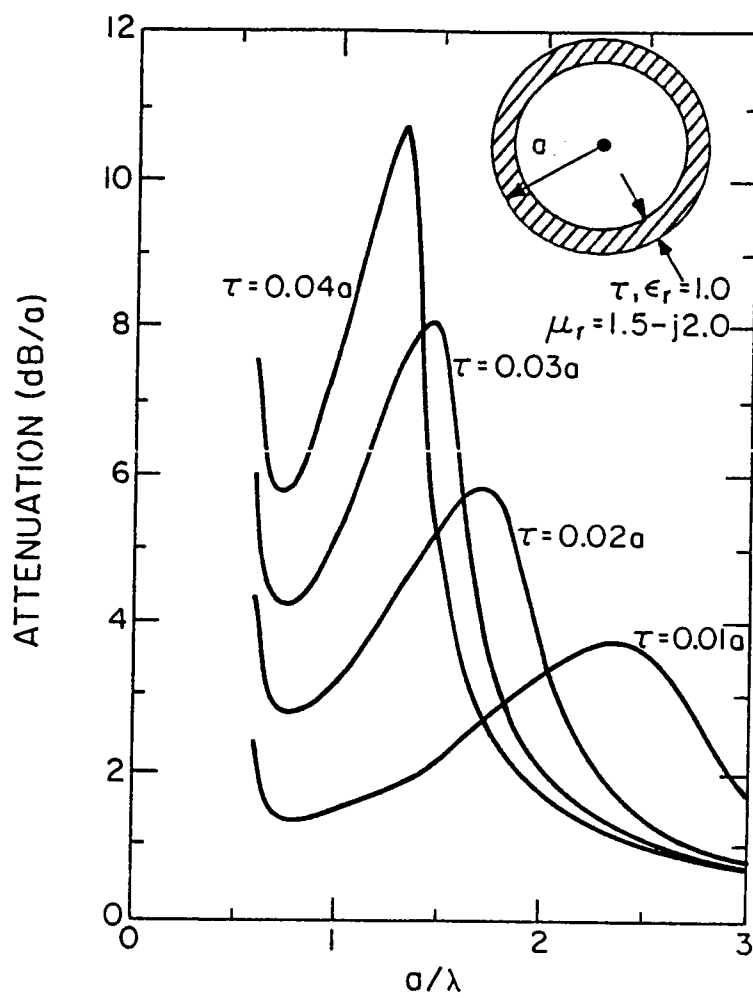


Fig. 2.5 Attenuation constants of the EH_{11} mode in a lossy magnetic coated waveguide ($\epsilon_r = 1.0$, $\mu_r = 1.5 - j2.0$).

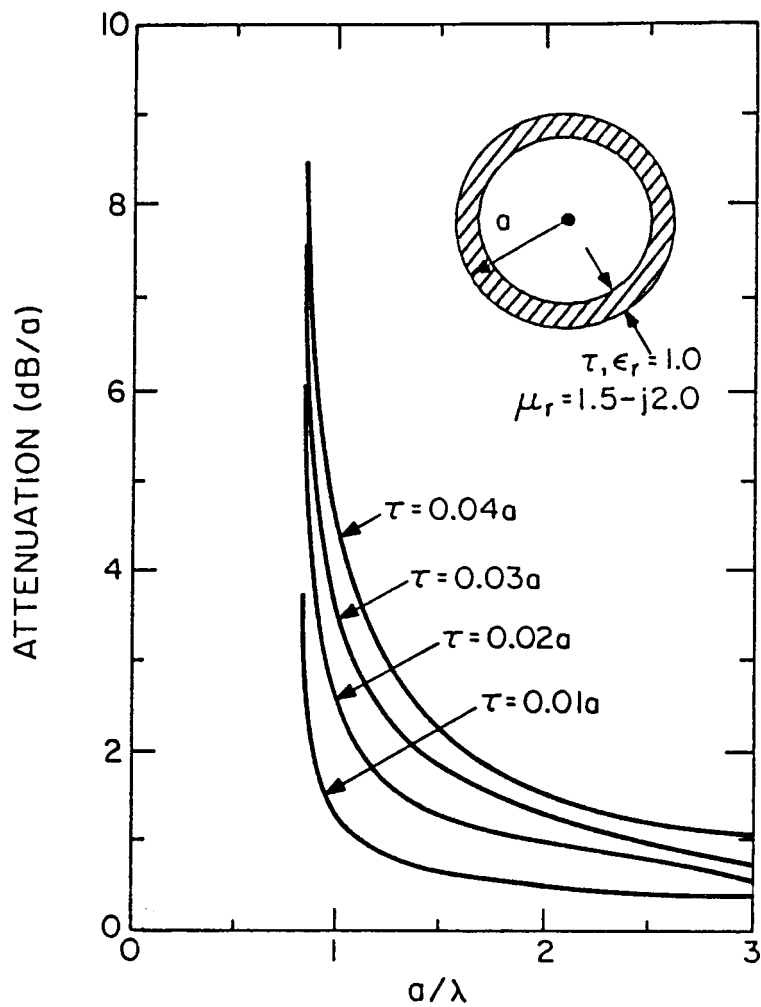


Fig. 2.6 Attenuation constants of the HE_{12} mode in a lossy magnetic coated waveguide ($\epsilon_r = 1.0$, $\mu_r = 1.5 - j2.0$).

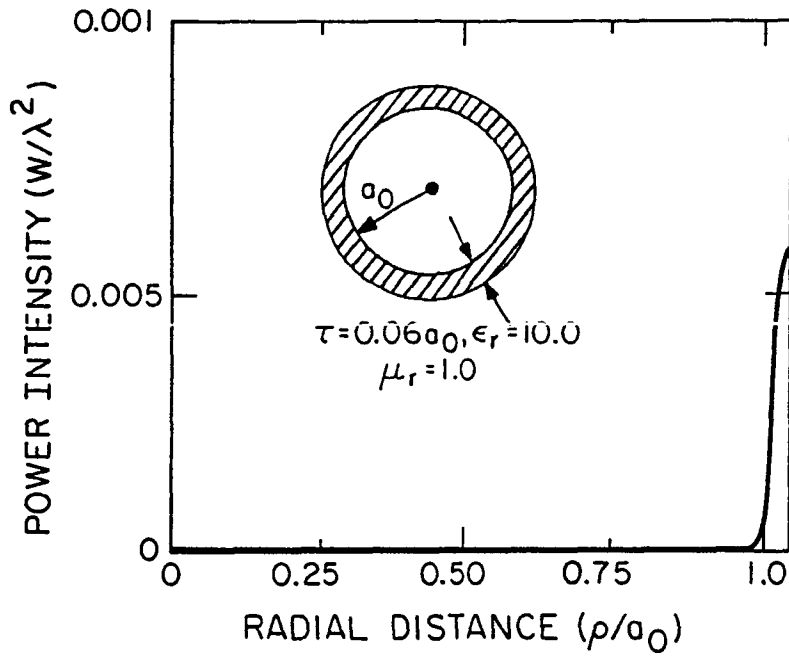


Fig. 2.7 Normalized angle-averaged power distribution in Watts/ λ^2 as a function of radial distance in a dielectric coated guide ($\epsilon_r = 10.0$, $\mu_r = 1.0$).

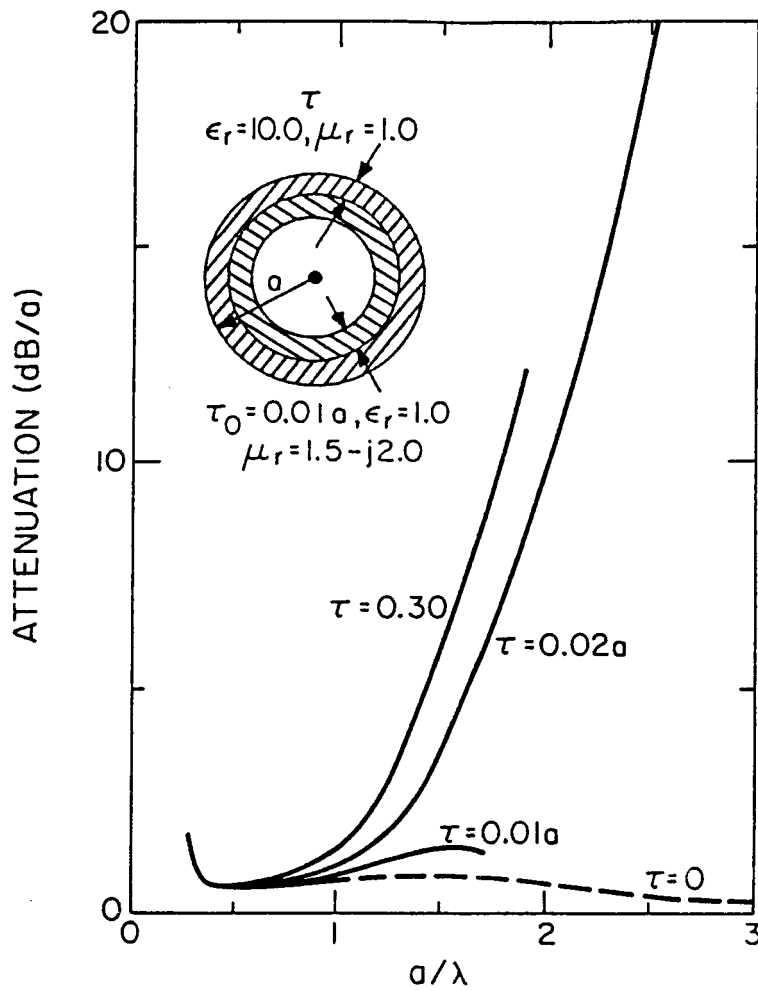


Fig. 2.8 Attenuation constants of the HE_{11} mode in a double layer coated waveguide with an inner layer of lossy magnetic material ($\epsilon_r = 1.0$, $\mu_r = 1.5 - j2.0$) and an outer layer of lossless dielectric material ($\epsilon_r = 10.0$, $\mu_r = 1.0$). The thickness of the inner layer is fixed while that for the outer layer is varied.

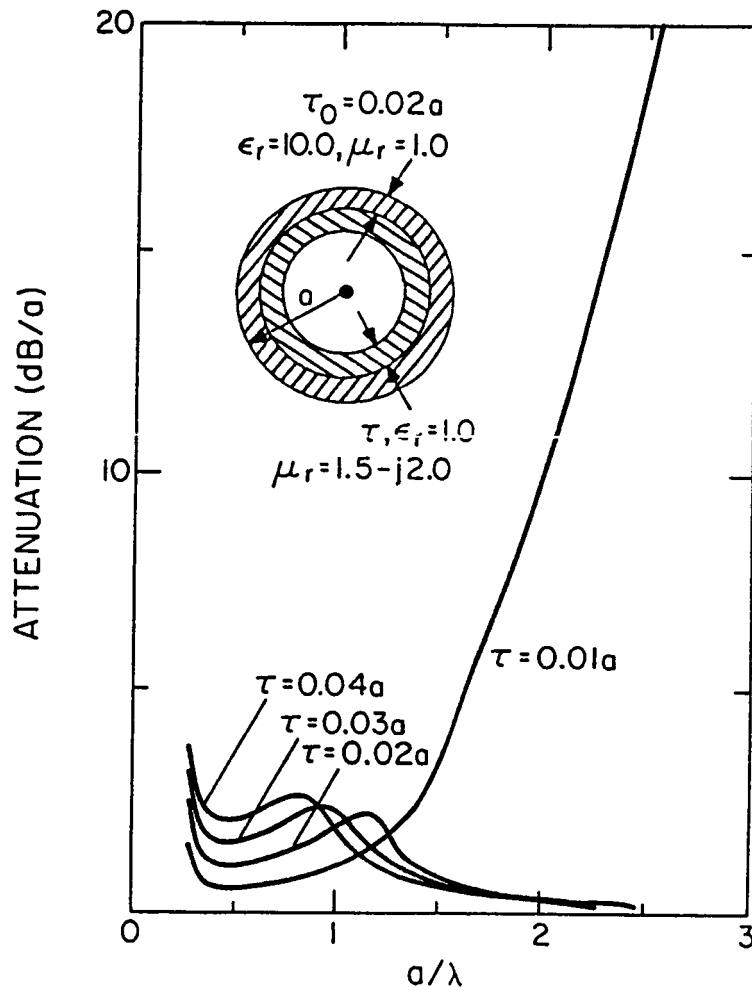


Fig. 2.9 Attenuation constants of the HE_{11} mode in a double layer coated waveguide with an inner layer of lossy magnetic material ($\epsilon_r = 1.0, \mu_r = 1.5 - j2.0$) and an outer layer of lossless dielectric material ($\epsilon_r = 10.0, \mu_r = 1.0$). The thickness of the outer layer is fixed while that for the inner layer is varied.

In Fig. 2.9, the thickness of the lossy layer is varied while the thickness of the lossless layer is increased. If the lossy layer becomes too thick, the field repulsion property of the lossless layer is dominant over the field attraction property of the lossless layer. Figure 2.10 reverses the lossless and the lossy layers so that the lossless layer is towards the waveguide center. No significant increase in attenuation is achieved with this configuration for the TE_{11} mode.

Finally, Fig. 2.11 shows the EH_{11} attenuation constant as function of increasing frequency for the waveguide wall - lossless layer - lossy layer geometry. The family of curves represents a fixed thickness of the lossy layer and varying thicknesses of the lossless layer. Again, there is a significantly higher level of modal attenuation over a wider frequency band for the multilayered case compared to that of a single layer of the lossy coating case. Note that the maximum value of the attenuation axis is now 100 dB/a (a = radius of cylinder). It is interesting to observe that up to $a/\lambda \sim 2.0$, a thicker lossless layer results in a higher attenuation. But for $a/\lambda > 2.0$, the $\tau = 0.01a$ case results in the highest attenuation. This geometry, though, is not an effective coating for the HE_{11} mode (Fig. 2.8).

2.4.3 Radar cross section reduction

The application of interest is the reduction of RCS of coated cavity structures. In such applications, the actual coating geometry must be optimized to effectively attenuate all the highly excited modes. Detailed discussion of the evaluation of the RCS from a coated waveguide can be found in Reference [12]. Figure 2.12 shows the theoretical RCS calculations for a length of circular waveguide terminated with a flat PEC plate. The diameter of the guide is 4λ , and the length is 10λ . The three curves correspond to the RCS of (i) an empty guide, (ii) a waveguide coated with a single layer of lossy magnetic coating, and (iii) a multilayered coated waveguide consisting of a lossless dielectric layer sandwiched between the waveguide wall and a lossy layer. For the given size of the structure, the single layer coating is

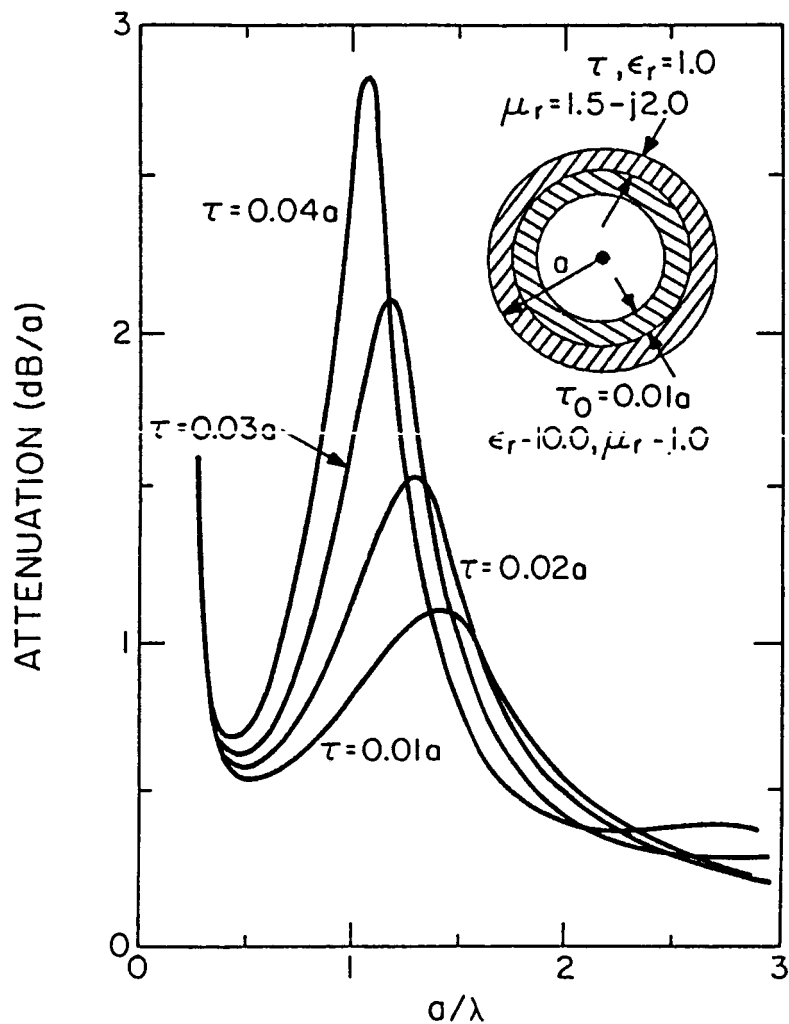


Fig. 2.10 Attenuation constants of the HE_{11} mode in a double layer coated waveguide with an inner layer of lossless dielectric material ($\epsilon_r = 10.0, \mu_r = 1.0$) and an outer layer of lossy magnetic material ($\epsilon_r = 1.0, \mu_r = 1.5 - j2.0$). The thickness of the inner layer is fixed while that for the outer layer is varied.

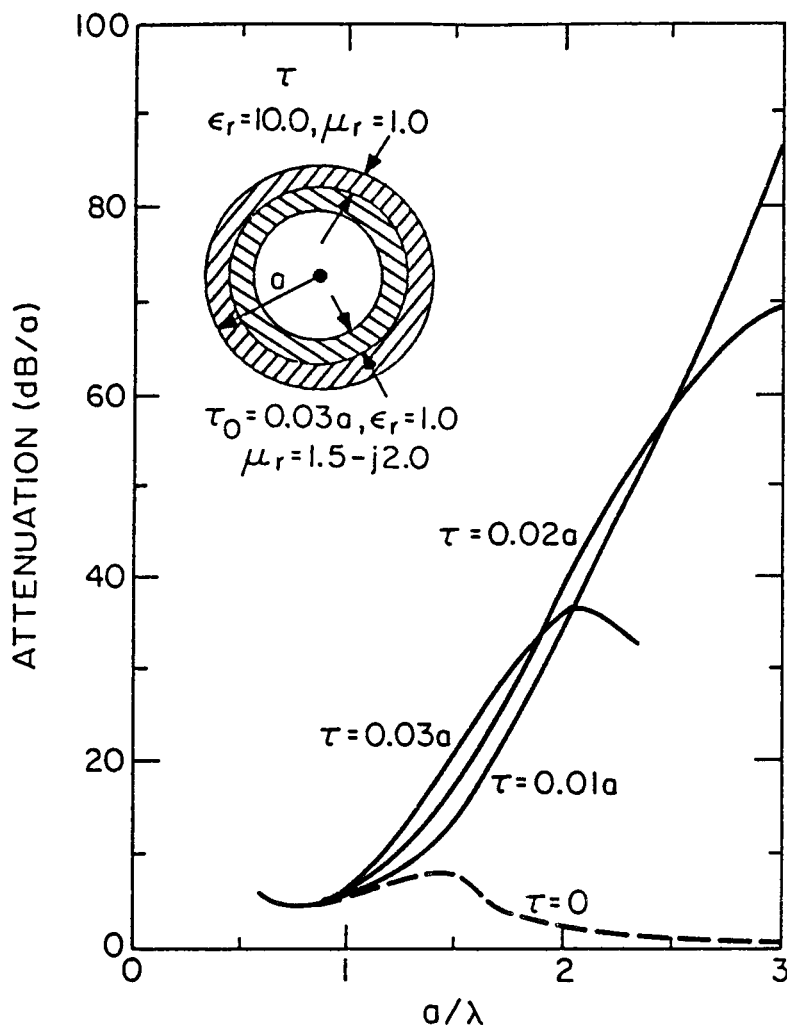


Fig. 2.11 Attenuation constants of the EH_{11} mode in a double layer coated waveguide with an inner layer of lossy magnetic material ($\epsilon_r = 1.0$, $\mu_r = 1.5 - j2.0$) and an outer layer of lossless dielectric material ($\epsilon_r = 10.0$, $\mu_r = 1.0$). The thickness of the inner layer is fixed while that for the outer layer is varied.

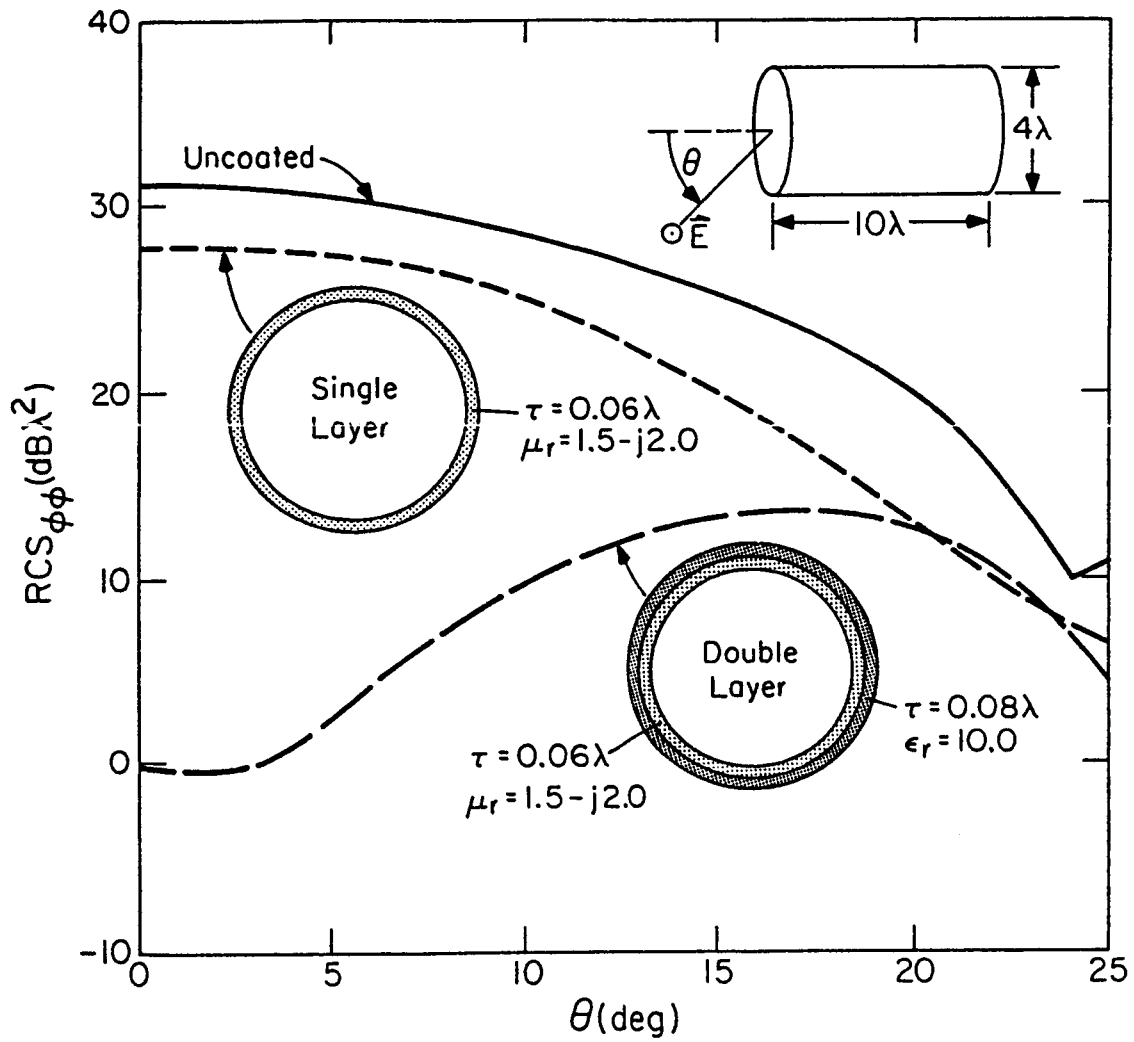


Fig. 2.12 RCS's of coated and uncoated circular cylinders with diameter 4λ and depth 10λ .

not very effective in reducing the RCS. However, a double layer coating results in a substantial reduction in the RCS of the cavity at near axial incidence. When the angle of incidence of the incoming plane wave $\theta \cong 20^\circ$, the three curves approach a similar level. This is due to the fact that the higher-order modes are now more strongly excited, and the chosen coating geometry is not effective in attenuating these modes.

2.5 Summary

This chapter studied interior coating as a means of reducing the RCS of arbitrary cavities by studying modal attenuation in coated waveguide structures. An overview of the modal fields in a coated circular waveguide was given. To avoid dealing with excessively large matrices, a method was shown to express the waveguide characteristic equation for any number of coating layers which involves only the manipulation of 4×4 matrices. This method was applied to study modal attenuation in a multilayered coated waveguide.

The dominant contributors to the RCS of a PEC-terminated waveguide at near-axial incidence are the low-order modes. A thin single layer of lossy magnetic material can greatly attenuate these modes, and thus reduce the RCS of a waveguide cavity. However, this is only effective over a narrow frequency band at low frequencies. With the proper combination of lossless dielectric coating and lossy magnetic coating, it was shown that a significantly higher modal attenuation can be attained over a broader frequency band for the HE_{11} and EH_{11} modes. For large off-axis incidence, higher-order modes come into importance. It should be possible to reduce these modes over a broad frequency band with the proper combination of three or more layers of coating.

CHAPTER 3

SHOOTING AND BOUNCING RAYS: CALCULATING THE RCS OF AN ARBITRARY CAVITY

3.1 Introduction

Traditionally, the problem of calculating the RCS of a cavity structure is treated by the modal analysis. For example, Chang and Senior [9] studied the open spherical shell problem based on the expansion of interior and exterior fields in the spherical wave function. Recently, the problem of scattering from an open-ended circular cylinder with wall coatings was analyzed by Lee *et al.* [25] by utilizing the cylindrical waveguide modes. Analytic solutions to a family of canonical problems have also been obtained by the dual series approach [26], [27]. However, the aforementioned techniques become impossible if (i) the shape of the cavity is not a perfect sphere or cylinder, (ii) the electrical dimension of the cavity is large, or (iii) the space inside the cavity is not homogeneous. These restrictions prevent the realistical modelling of physical problems and hinder the study of the effects of shaping on RCS.

In this chapter, a different strategy for analyzing the open cavity problem, entitled shooting and bouncing rays (SBR), is presented. A dense grid of geometric optics (GO) rays representing an incident plane wave is "shot" into the cavity through the front aperture and followed as the rays bounce from conductors, penetrate through materials, and eventually return to the opening of the cavity (see Fig. 3.1). An innovative scheme is then used to integrate the aperture field to obtain the scattered field. This approach has the following features. First, this is the first attempt of its kind at solving partially open structures using the ray technique. This approach is different from the traditional ray-tracing or ray-mode hybrid methods. Second, a real physical problem can be modelled closely, taking into account the noncircular opening of the cavity, the wall coating, and the longitudinal bending or twisting of

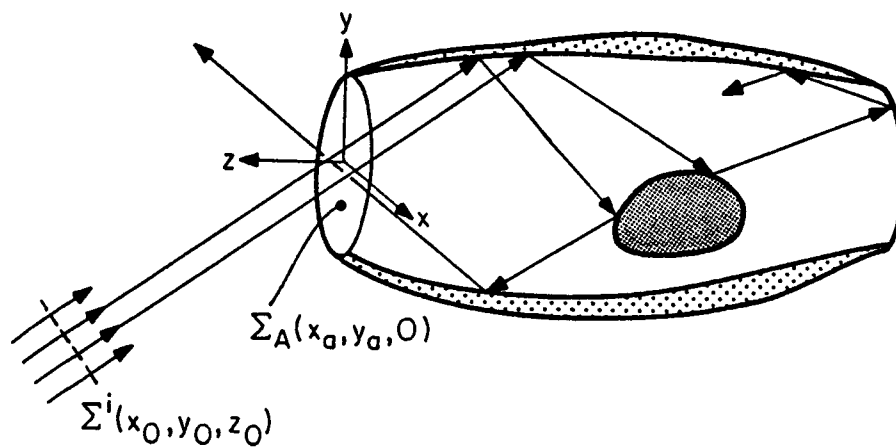


Fig. 3.1 Ray bouncing approach to calculating the RCS of a partially open cavity with complex geometry and material loading.

the cavity. This method is so simple in concept that there is virtually no restriction on the shape or material loading of the cavity.

In Sec. 3.2, the problem is formulated based on geometrical optics. The paths of each individual ray are first determined by Snell's law. The field amplitudes associated with each ray are computed by taking into consideration (i) geometrical divergence factor, (ii) polarization, and (iii) material loading of the cavity walls. The contributions to the backscattered field from individual rays are then summed up to arrive at the total RCS due to the interior irradiation of the cavity. Results of the SBR method are compared to the existing modal results for the case of a straight circular cylinder with a PEC termination in Sec. 3.4.

3.2 Formulation of Shooting and Bouncing Rays

Referring to Fig. 3.1, consider an arbitrary cavity with an opening at the aperture Σ_A . The inside walls of the cavity may be coated with dielectric or magnetic materials. Additional scatterers may also exist inside the cavity, but will not be considered in this treatment. The incident plane wave is given by (for $\exp(+j\omega t)$ time convention)

$$\vec{E}^i = [-\hat{\phi} I + \hat{\theta}^i \bar{I}] e^{j\vec{k}^i \cdot \hat{r}} \quad (3.1)$$

where

$$\vec{k}^i = k_0 (\hat{x} \sin \theta^i \cos \phi^i + \hat{y} \sin \theta^i \sin \phi^i + \hat{z} \cos \theta^i)$$

I = amplitude of the TE wave

\bar{I} = amplitude of the TM wave.

The problem at hand is to determine the backscattered field in the direction of \vec{k}^i and the RCS of the cavity. The backscattering from the exterior of the cavity is not treated, since (i) the exterior scattering is small for small angle of incidence θ^i and (ii) the exterior scattered field can be considered separately. In addition, it is well known that the contribution to the backscattered field from the energy coupled into and re-radiated from the cavity is much greater than that from the rim diffraction, especially if the cavity opening is large compared to the wavelength [8], [10]-[12], [25], [28]. Therefore, attention will be focused on the interior irradiation mechanism.

The ray bouncing approach will be carried out in three parts:

- (i) Given the geometry of the cavity and the incident field, find the ray paths in the cavity by ray tracing. This part of the problem is dependent only on the geometry of the problem.
- (ii) Determine the field amplitude of the exit rays on the aperture based on geometrical optics. This involves calculating the ray tube divergence factors and the reflection coefficients.
- (iii) Use Kirchhoff's approximation (physical optics) to determine the backscattered field and the RCS.

These steps will be described in detail in the following sections.

3.2.1 Ray tracing

In order to model the incident plane wave, parallel rays are launched from the incident direction. Each ray is represented by a line in space with a reference point (x_0, y_0, z_0) and a direction vector (s_1, s_2, s_3) . Any point (x_1, y_1, z_1) along this line would then be described by

$$(x_1, y_1, z_1) = (x_0, y_0, z_0) + (s_1, s_2, s_3) t \quad (3.2)$$

By this definition, if the phase of the field at (x_1, y_1, z_1) lags that of point (x_0, y_0, z_0) , then t will be a positive quantity. The direction vector of the incident rays is given by

$$s_1 = -\sin \theta^i \cos \phi^i \quad (3.3)$$

$$s_2 = -\sin \theta^i \sin \phi^i$$

$$s_3 = -\cos \phi^i .$$

The reference point (x_0, y_0, z_0) on the incident plane Σ^i can be related to the point $(x_a, y_a, 0)$ on the aperture Σ_A via

$$x_0 = (s_2^2 + s_3^2) x_a - s_1 s_2 y_a + s_1 t_0$$

$$y_0 = (s_1^2 + s_3^2) y_a - s_1 s_2 y_a + s_1 t_0 \quad (3.4)$$

$$z_0 = -s_1 s_3 x_a - s_2 s_3 y_a + s_3 t_0 .$$

The parameter t_0 in (3.4) determines how far Σ^i is from the aperture plane and can be chosen arbitrarily (e.g., $t_0 = -10$). To summarize, the incident ray is described by (3.2), where the direction vector is given in (3.3) and the reference point (x_0, y_0, z_0) can be related to a corresponding point on the aperture via (3.4).

Once the incident rays have been defined, the impact point of each ray on the inner wall of the cavity can be determined. This is accomplished by solving simultaneously the equation describing the cavity $z = f(x, y)$ and (3.2). For example, if the cavity is a circular cylinder with radius a , the intersection is found by substituting into (3.2)

$$t = (-B + \sqrt{B^2 - 4AC}) / 2A \quad (3.5)$$

where

$$A = s_1^2 + s_2^2$$

$$B = 2(s_1 x_0 + s_2 y_0)$$

$$C = x_0^2 + y_0^2 - a^2 .$$

For arbitrary cavity structures, the condition $\vec{k}^i \cdot \hat{n} > 0$, where \hat{n} is the inward pointing normal of the wall, may be useful for discarding extraneous solutions.

Next, the equation for the reflected ray will be determined. The reflected ray must satisfy Snell's law, namely, (i) it must lie in the plane of incidence and (ii) the angle of reflection must equal the angle of incidence. Referring to Fig. 3.2, define a unit vector

$$\hat{m} = (\hat{\Gamma} \times \hat{n}) / \sin \theta_c^i \quad (3.6)$$

\hat{m} is perpendicular to the plane of incidence. The above two conditions can be restated as (i) $\hat{\Gamma} \cdot \hat{m} = 0$ and (ii) $\hat{\Gamma} \cdot \hat{n} = \cos \theta_c^i$. These two conditions are solved simultaneously in

order to determine the direction of the reflected ray. The equation for the reflected ray is now complete since both the direction and the reference point (impact point) are known.

Consequently, by using this reflected ray as the incident ray, the above procedure can be repeated until the ray exits the cavity. The exit of the ray from the cavity is easily detected when the ray intersects the aperture Σ_A . For every ray launched, a set of impact points inside the cavity and the direction of the existing ray are obtained.

3.2.2 Amplitude tracking

Once the ray paths inside the cavity are found, the field amplitude along the ray can be determined. For each ray launched, a set of impact points was found within the cavity, $\{(x_1, y_1, z_1)\}$, $i = 1, 2, \dots, N$. The aperture field associated with the exit ray, $\vec{E}(x_N, y_N, 0)$, is to be determined. From geometrical optics, the electric field obeys the following recursion relationship

$$\vec{E}(x_{i+1}^-, y_{i+1}^-, z_{i+1}^-) = (DF)_i \cdot (\bar{\Gamma})_i \cdot \vec{E}(x_i^-, y_i^-, z_i^-) \cdot e^{-j(\text{Phase})} \quad (3.7)$$

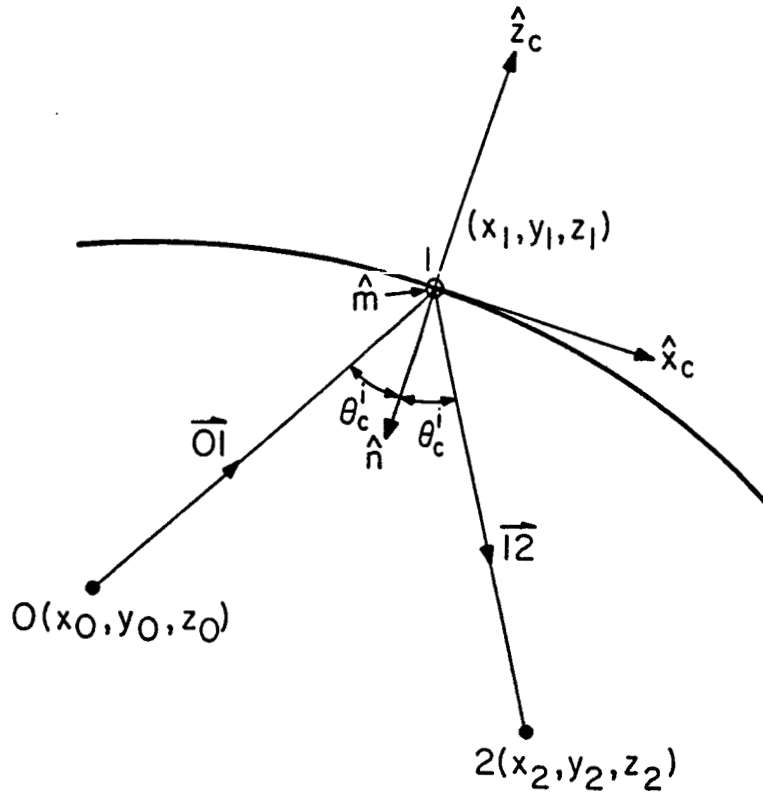


Fig. 3.2 Local coordinate system of the first impact point.

where Phase = $k_0 [(x_{i+1} - x_i)^2 + (y_{i+1} - y_i)^2 + (z_{i+1} - z_i)^2]^{1/2}$ and $\vec{E}(x_i^-, y_i^-, z_i^-)$ is the incident field at (x_i, y_i, z_i) . $\bar{\Gamma}_i$ is the planar reflection coefficient matrix at the i^{th} reflection point where the original curve interface in Fig. 3.2 is replaced by its tangent plane at the reflection point. $(DF)_i$ is the divergence factor which governs the spreading of the differential ray tube from just after the i^{th} reflection to just before the $(i+1)^{\text{th}}$ reflection. The remaining tasks are the determinations of these two quantities.

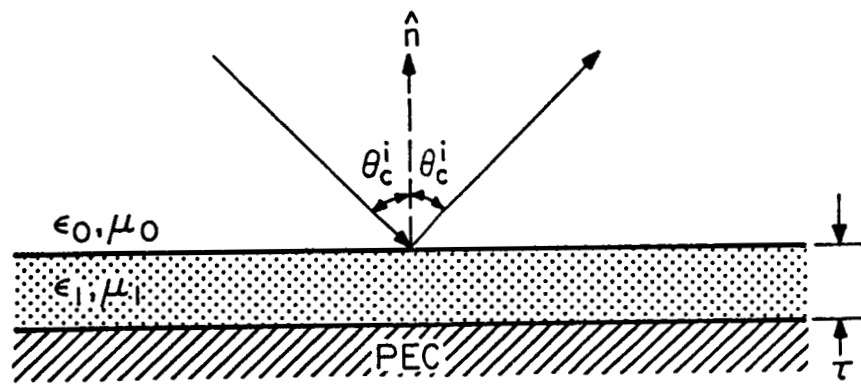
A. Planar Reflection Coefficients. Referring to Fig. 3.3(a), attention will be restricted to the case of one layer of dielectric or magnetic coating with thickness τ and backed by perfect conducting walls. The transmission line analogy to the field problem is shown in Fig. 3.3(b). The well-known planar reflection coefficients for the TE and the TM case are summarized in Table 3.1.

Table 3.1 Reflection Coefficients

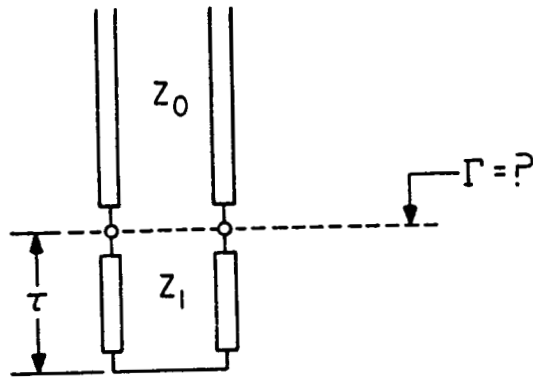
TE	TM
$\Gamma = \frac{1 - Z_0/Z_{\rightarrow}}{1 + Z_0/Z_{\rightarrow}}$	$\bar{\Gamma} = \frac{1 - Z_0/Z_{\rightarrow}}{1 + Z_0/Z_{\rightarrow}}$
$Z_{\rightarrow} = jZ_1 \tan(\beta_{z1}\tau)$	$Z_{\rightarrow} = jZ_1 \tan(\beta_{z1}\tau)$
$Z_1 = \omega\mu_1/\beta_{z1}$	$Z_1 = \beta_{z1}/\omega\epsilon_1$
$Z_0 = \omega\mu_0/\beta_{z0}$	$Z_0 = \beta_{z0}/\omega\epsilon_0$

$$\beta_{z0} = \omega\sqrt{\mu_0\epsilon_0} \cos \theta_c^i$$

$$\beta_{z0} = \omega\sqrt{\mu_1\epsilon_1 - \mu_0\epsilon_0 \sin^2 \theta_c^i}$$



(a)



(b)

Fig. 3.3 (a) The original curved interface is replaced by its tangent plane at the impact point 1 for calculating the reflection coefficient based on GO.
 (b) Transmission line analogy of the planar reflection problem in (a).

For the assumed time convention, the complex root is chosen to have a positive real component and a negative imaginary component.

B. TE/TM Decomposition. In order to apply the reflection coefficients Γ and $\bar{\Gamma}$ found in Table 3.1, the incident field needs to be decomposed into its TE and TM components. Using subscript c to denote local coordinates (see Fig. 3.2), the incident field can be written as

$$\vec{E}(1^-) = (\vec{E}^i \cdot \hat{\phi}_c^i) \hat{\phi}_c^i + (\vec{E}^i \cdot \hat{\theta}_c^i) \hat{\theta}_c^i . \quad (3.8)$$

The reflected field is then given by

$$\vec{E}(1^+) = \Gamma(\vec{E}^i \cdot \hat{\phi}_c^i) \hat{\phi}_c^r + \bar{\Gamma}(\vec{E}^i \cdot \hat{\theta}_c^i) \hat{\theta}_c^r . \quad (3.9)$$

So the reflected field is easily found once $\hat{\phi}_c^{i,r}$ and $\hat{\theta}_c^{i,r}$ are determined in terms of the global xyz coordinate. Choose

$$\begin{aligned} \hat{x}_c &= \hat{m} \times \hat{n} \\ \hat{z}_c &= -\hat{n} \\ \hat{y}_c &= -\hat{m} . \end{aligned} \quad (3.10)$$

From Fig. 3.2,

$$\begin{aligned} \theta_c^i &= \cos^{-1}(\hat{10} \cdot \hat{n}) \\ \phi_c^i &= 0 . \end{aligned} \quad (3.11)$$

Then

$$\begin{aligned}\hat{\theta}_c^i &= \hat{x}_c \cos \theta_c^i - \hat{z}_c \sin \theta_c^i \\ \hat{\phi}_c^i &= \hat{y}_c\end{aligned}\tag{3.12}$$

and

$$\begin{aligned}\hat{\theta}_c^r &= -\hat{x}_c \cos \theta_c^i - \hat{z}_c \sin \theta_c^i \\ \hat{\phi}_c^r &= \hat{y}_c\end{aligned}\tag{3.13}$$

C. Divergence Factor.

This space intentionally left blank

Pages 46 - 48 intentionally left blank.

This space intentionally left blank

3.2.3 Physical optics

Given the outgoing field on the aperture Σ_A , the outgoing field can be computed by the standard physical-optics approximation. First, the outgoing field is replaced by an equivalent magnetic current sheet \vec{K}_S

$$\vec{K}_S = \begin{cases} 2 \vec{E}(x_N, y_N, 0) \times \hat{z} & ; \text{ over } \Sigma_A \\ 0 & ; \text{ outside } \Sigma_A \end{cases} \quad (3.23)$$

\vec{K}_S radiates in the backscattering direction and gives rise to the RCS. The backscattered field is calculated from

$$\vec{E}^{bs} = \frac{e^{-jk_0 r}}{r} [\hat{\theta}^i A_\theta + \hat{\phi}^i A_\phi]$$

$$\begin{bmatrix} A_\theta \\ A_\phi \end{bmatrix} = \frac{jk_0}{2\pi} \iint_{\Sigma_A} dx dy e^{jk_0(ux + vy)} \cdot \begin{bmatrix} E_x \cos \phi^i + E_y \sin \phi^i \\ (-E_x \sin \phi^i + E_y \cos \phi^i) \cos \theta^i \end{bmatrix} \quad (3.24)$$

$$u = \sin \theta^i \cos \phi^i$$

$$v = \sin \theta^i \sin \phi^i$$

E_x and E_y are the x and y components of the outgoing field on the aperture Σ_A . The RCS is defined in Table 3.2.

PRECEDING PAGE BLANK NOT FILMED

46, 47, 48

Table 3.2 Radar Cross Section Definition

	TE Incidence ($I = 1, \bar{I} = 0$)	TM Incidence ($I = 0, \bar{I} = 1$)
Co-pol	$RCS_{\phi\phi} = 4\pi A_{\phi} ^2$	$RCS_{\theta\theta} = 4\pi A_{\theta} ^2$
Cross-pol	$RCS_{\theta\phi} = 4\pi A_{\theta} ^2$	$RCS_{\phi\theta} = 4\pi A_{\phi} ^2$
Phase	$\angle A_{\phi}, \angle A_{\theta}$	$\angle A_{\theta}, \angle A_{\phi}$

In general, the positions of the outgoing rays are randomly dispersed over the aperture, even if the incident rays are launched uniformly. Since the outgoing rays do not lie on an equally spaced grid, the integration in (3.24) cannot be easily carried out. One possible solution to this problem would be to interpolate the results to find the fields on the integration grid. However, the proper interpolation scheme is difficult and an alternative approach is taken. Suppose only a small ray tube is shot into the cavity. This ray tube bounces around the walls and eventually comes to the aperture plane. It is possible to compute the backscattered field due to this ray tube by taking into account its wavefront curvature, size, and shape. By repeating this process until enough ray tubes are launched into the cavity to model the incident plane wave, the total scattered field should be the sum of the scattered field due to each individual ray tube. Using this idea, the scattered field expression will now be derived.

Consider one of the incident ray tubes with an area of $(\Delta x_0 \Delta y_0)$. The central ray with direction vector (s_1, s_2, s_3) hits point (x_i, y_i) on Σ_A (see Fig. 3.4). The field within the exiting ray tube area $(\Delta x_1 \Delta y_1)$ will be approximated as follows:

$$\begin{bmatrix} E_x(x,y) \\ E_y(x,y) \end{bmatrix} = \begin{bmatrix} E_x(x_i,y_i) \\ E_y(x_i,y_i) \end{bmatrix} e^{-jk_0[s_1(x-x_i) + s_2(y-y_i)]} \quad (3.25)$$

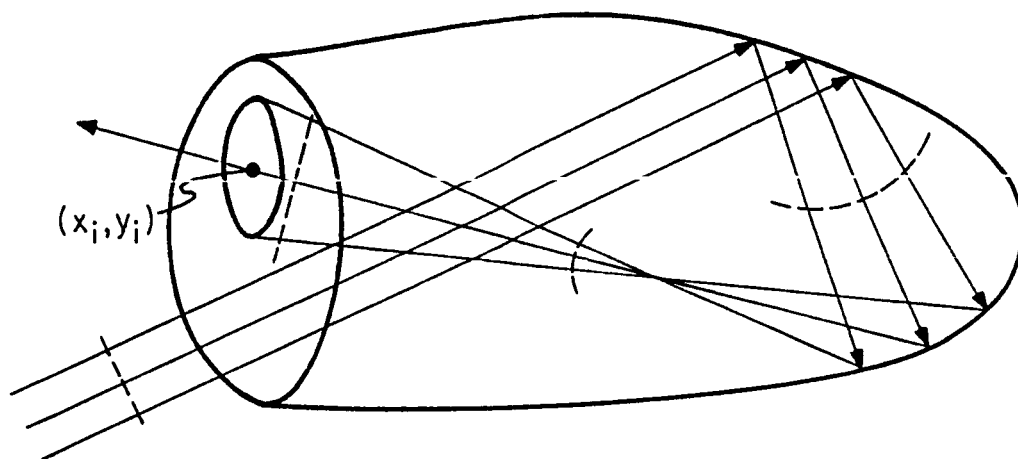


Fig. 3.4 Planar approximation for the wavefront of the exit ray tube.

In other words, the field with the ray tube at point (x, y) has the same magnitude as the field associated with the central ray. In addition, there is a linear phase variation across the ray tube. This linear phase approximation should be valid as long as the output ray tube is not too large. The physical-optics integral in (3.24) can now be evaluated using the plane-wave approximation. By summing over each ray tube, (3.24) becomes

$$\begin{bmatrix} A_\theta \\ A_\phi \end{bmatrix} = \frac{jk_0}{2\pi} \sum_i \int_{\text{ith ray tube}} \int_{\text{exit}} dx dy e^{jk_0(ux+vy)} e^{-jk_0[s_1(x-x_i) + s_2(y-y_i)]} \begin{bmatrix} E_x(x_i, y_i) \cos \phi^i + E_y(x_i, y_i) \sin \phi^i \\ -E_x(x_i, y_i) \sin \phi^i \cos \theta^i + E_y(x_i, y_i) \cos \phi^i \cos \theta^i \end{bmatrix} \quad (3.26)$$

Since the fields associated with each exit ray, $E_x(x_i, y_i)$ and $E_y(x_i, y_i)$, are independent of the integration variables x and y , the bracket in (3.26) can be taken out of the integral sign:

$$\begin{bmatrix} A_\theta \\ A_\phi \end{bmatrix} = \frac{jk_0}{2\pi} \sum_i \begin{bmatrix} E_x(x_i, y_i) \cos \phi^i + E_y(x_i, y_i) \sin \phi^i \\ -E_x(x_i, y_i) \sin \phi^i \cos \theta^i + E_y(x_i, y_i) \cos \phi^i \cos \theta^i \end{bmatrix} e^{-jk_0[s_1 x_i + s_2 y_i]} (\Delta x_i \Delta y_i) I_i \quad (3.27)$$

where

$$I_i = \frac{1}{(\Delta x_i \Delta y_i)} \int_{\text{ith ray}} \int_{\text{exit tube}} dx dy e^{jk_0[(u-s_1)x + (v-s_2)y]}$$

and

$(\Delta x_i \Delta y_i)$ = area of the exit ray tube.

Closer examination reveals that I_i is nothing but the Fourier transform of the ray tube shape function (normalized with respect to the ray tube area). In order to determine the shape of the i th exit ray tube, four adjacent rays are launched into the cavity in the form of a square as shown in Fig. 3.5. These four rays, upon exit, form a tetragonal shape on the output aperture. The position vectors of the four rays on the aperture are denoted by $\vec{\gamma}_n = x_n \hat{x} + y_n \hat{y}$, $n = 1, 2, 3, 4$. The normalized Fourier transform of the tetragonal shaped function can now be evaluated as described in [34]:

$$I_i = S(p,q) / S(0,0) \quad (3.28)$$

where

$$S(p,q) = \sum_{n=1}^4 e^{j\vec{\omega} \cdot \vec{\gamma}_n} \frac{(x_{n+1} - x_n)(y_n - y_{n-1}) - (y_{n+1} - y_n)(x_n - x_{n-1})}{[(x_n - x_{n-1})p + (y_n - y_{n-1})q][-(x_{n+1} - x_n)p + (y_{n+1} - y_n)q]}$$

$$S(0,0) = 1/2 [(x_1 y_2 - x_2 y_1) + (x_2 y_3 - x_3 y_2) + (x_3 y_4 - x_4 y_3) + (x_4 y_1 - x_1 y_4)]$$

$$p = k_0 (u-s_1)$$

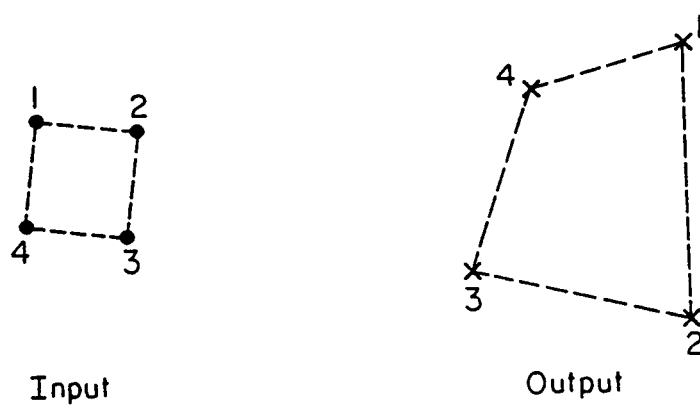


Fig. 3.5 Shape of the exit ray tube on the output aperture is obtained by shooting four adjacent rays into the cavity.

$$q = k_0 (v - s_2)$$

$$\vec{w} = p\hat{x} + q\hat{y} .$$

Note that by definition, $\vec{\gamma}_0 = \vec{\gamma}_4$ in the above expression. The shape of the ray tube is approximated by a four-sided polygon. If desired, higher-order polygons can always be used for a more refined approximation of the ray tube shape.

Lastly, the output ray tube area ($\Delta x_i \Delta y_i$) can be related to the incident ray tube area ($\Delta x_0 \Delta y_0$) through the ray tube divergence factors calculated earlier. The area of the exit ray tube is related to the area of the incident ray tube via the product of the divergence factors:

$$(\Delta x_i \Delta y_i) = \left[\prod_{i=1}^N |(DF)_i| \right]^{-2} \left(\frac{\cos \theta^i}{\cos \theta_2} \right) (\Delta x_0 \Delta y_0) . \quad (3.29)$$

The ratio of the cosines is an added factor which accounts for the angles of the ray tubes entering and exiting the cavity (see Fig. 3.6).

If the quantity of interest is the bistatic cross section (BCS) rather than the assumed monostatic RCS, the incident direction angles θ^i and ϕ^i should be replaced by the observation direction angles θ^{ob} and ϕ^{ob} in (3.24), (3.26), and (3.27).

To summarize, the physical-optics integral defined in (3.24) is evaluated by summing the backscattering contributions due to each ray tube. The wavefront of the exiting ray tube is approximated to be planar as given in (3.25). The shape of the exit ray tube is approximated by a four-sided polygon. The far field is proportional to the Fourier transform of this normalized shape function and is found using (3.28). Finally, the area of the exit ray tube is found by the product of the divergence factors and is related to the incident ray tube via (3.29).

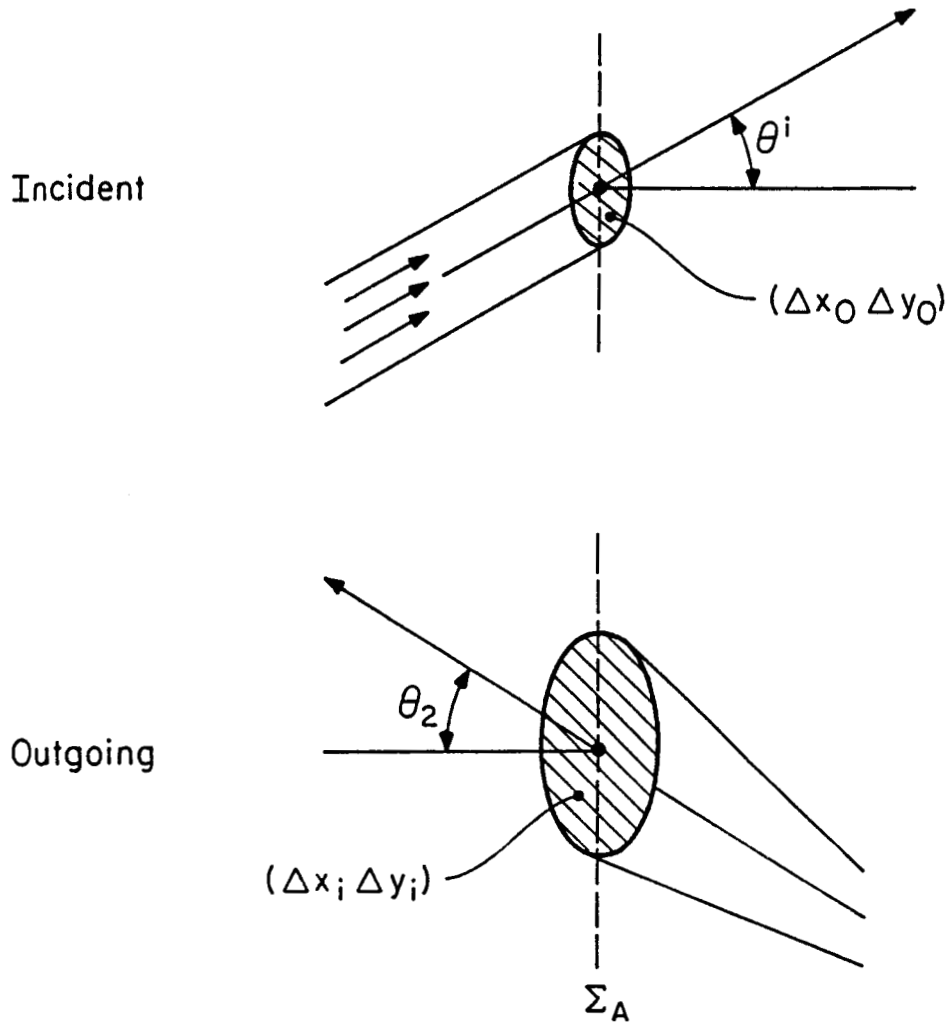


Fig. 3.6 The area of the output ray tube is related to that of the incident ray tube by the product of the divergence factors.

3.3 Numerical Results

A ray bouncing program, denoted as SBR (Shooting and Bouncing Rays), has been implemented based on the formulation described in Sec. 3.2. In this program, it is assumed that the cavity is composed of an arbitrary cylindrical cavity with a flat aperture at $z=0$ and a flat PEC termination at $z=d$. The inner walls of the cylinder can be coated with either dielectric or magnetic materials. Below, the comparison of SBR results with those generated by the modal analysis for a circular cylinder with uniform cross section is shown.

3.3.1 Exit ray positions

Shown in Fig. 3.7 are plots of the incident and exit ray positions on the aperture plane for a circular cylinder with a flat end-plate. The incident rays are launched from a uniformly spaced grid on the aperture. For a small incident angle ($\theta = 1^\circ$), the majority of the incident rays simply reflect off the end-plate and bounce back to the aperture without hitting the side walls. Therefore, they remain uniformly spaced on the exit aperture. As the incident angle increases, the positions of the exit rays become more dispersed due to the large number of bounces inside the cavity. This behavior is even more apparent in the case of an elliptical cylinder with nonuniform cross sections as shown in Fig. 3.8.

3.3.2 Comparison with modal analysis

RCS results generated by the SBR program are compared with those obtained by the modal analysis [12] for a straight circular cylinder with PEC walls. Shown in Figs. 3.9-3.11 are RCS plots versus angle θ for circular cylinders with a fixed diameter of 4λ and a different depth d . The copolarization of both the TE and TM cases are plotted as $RCS_{\phi\phi}$ and $RCS_{\theta\theta}$, respectively. The solid circles are the modal results and the solid curves represent results from the present SBR formulation. Good agreement is obtained between the ray bouncing method

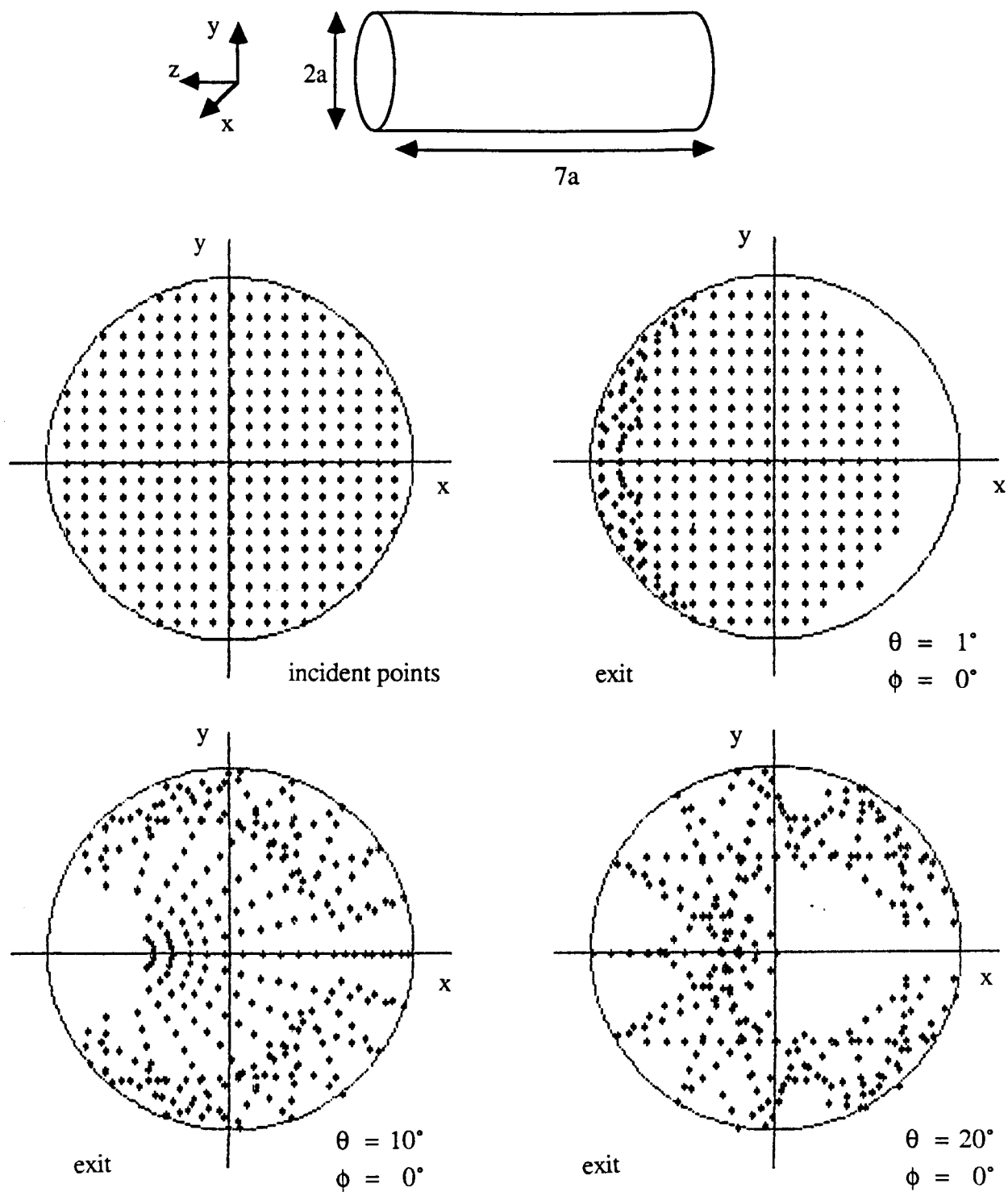


Fig. 3.7 The incident and exit ray positions on the aperture for a circular cylinder with a flat end-plate.

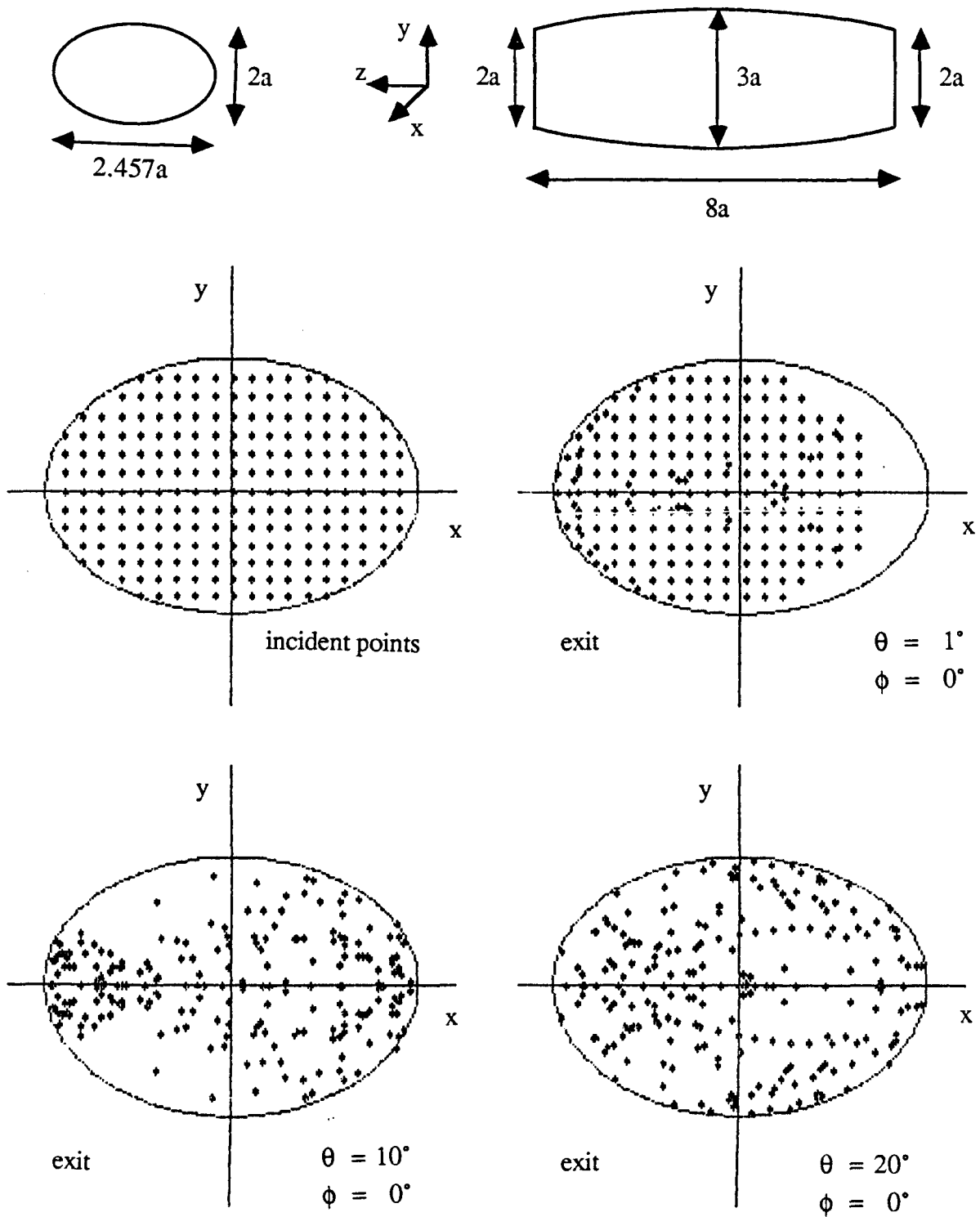


Fig. 3.8 The incident and exit ray positions on the aperture for an elliptical cylinder with nonuniform cross section and a flat end-plate.

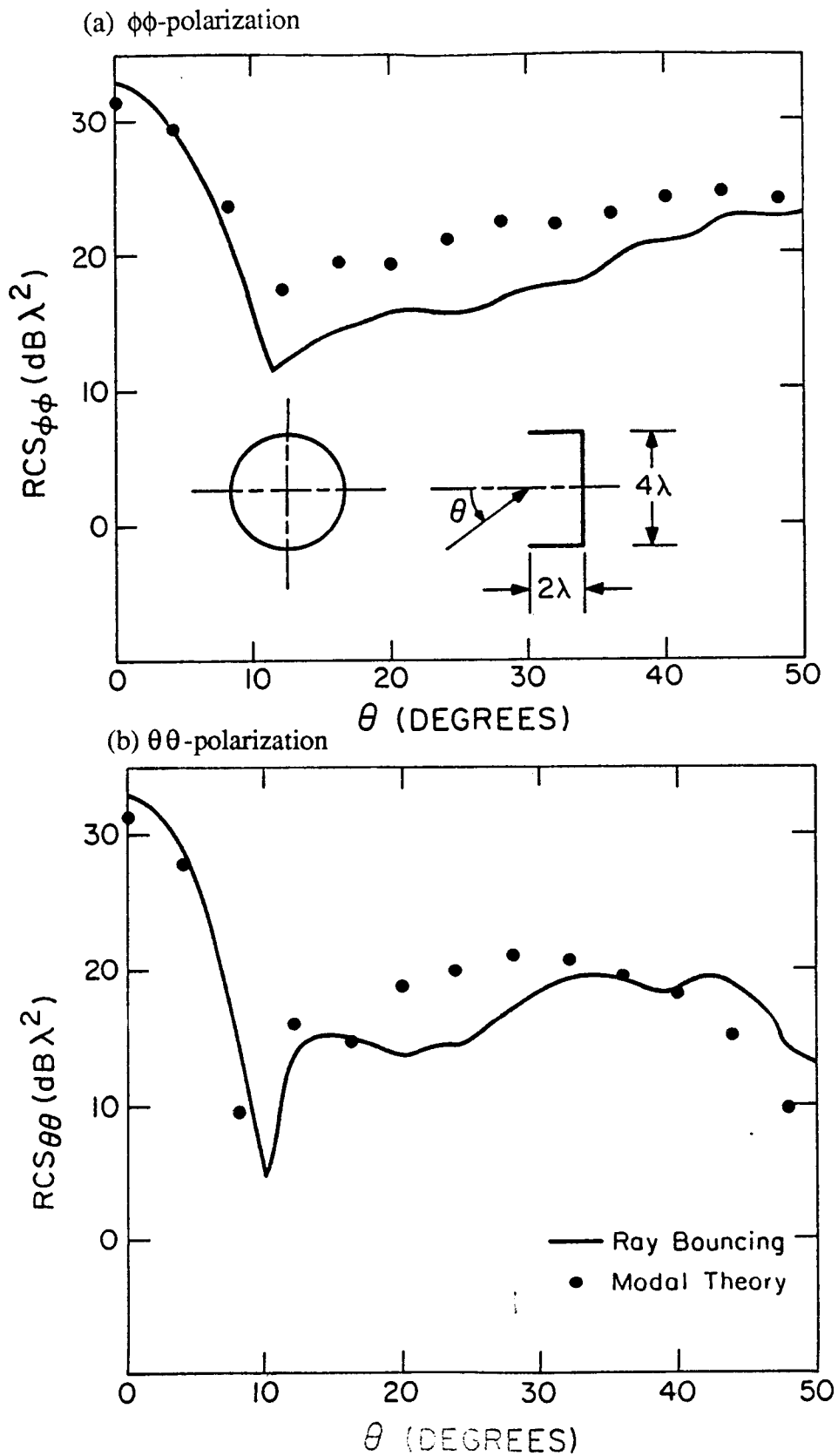


Fig. 3.9 Comparison of results for ray bouncing with modal analysis for a circular cylinder with diameter 4λ and depth 2λ . (a) $\phi\phi$ -polarization, (b) $\theta\theta$ -polarization.

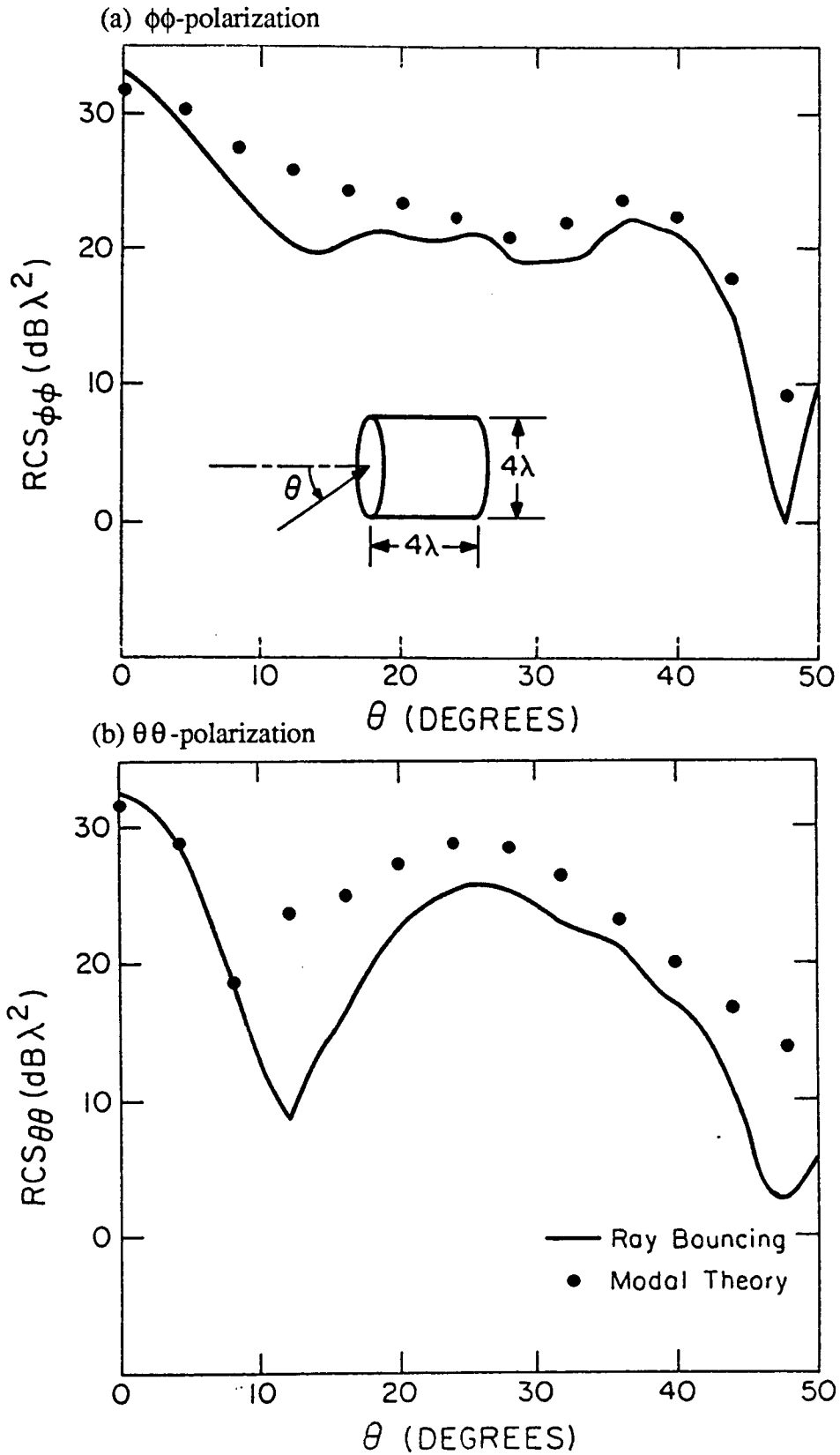


Fig. 3.10 Comparison of results for ray bouncing with modal analysis for a circular cylinder with diameter 4λ and depth 4λ . (a) $\phi\phi$ -polarization, (b) $\theta\theta$ -polarization.

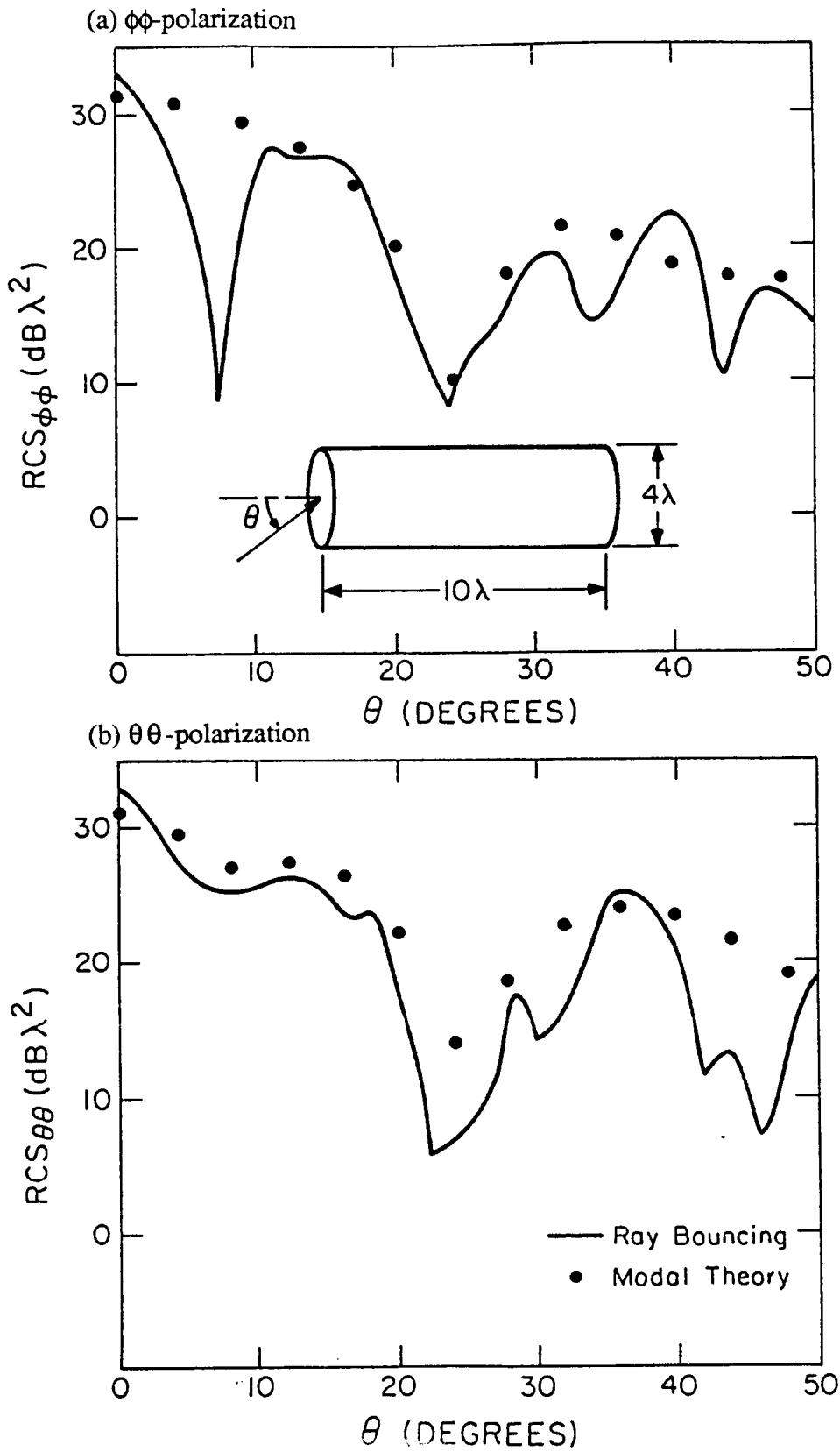


Fig. 3.11 Comparison of results for ray bouncing with modal analysis for a circular cylinder with diameter 4λ and depth 10λ . (a) $\phi\phi$ -polarization, (b) $\theta\theta$ -polarization.

and the modal analysis, except in Fig. 3.11(a) for the 10λ deep cylinder. Possible reasons for the discrepancy will be addressed in Chapter 5. Although a comparison with a much larger cylinder is preferable, the modal analysis program was limited to about a 4λ opening.

The convergence of the present ray formulation is checked by increasing the total number of rays launched into the cavity. Shown in Fig. 3.12(a) is the $RCS_{\theta\theta}$ at $\theta = 25^\circ$ plotted as a function of the number of rays per wavelength. It is observed that the results converged for a density greater than about 10-15 rays per wavelength. As the depth of the cylinder increases, the rate of convergence slows down. This is presumably due to an increased number of ray bounces inside the cavity and the highly divergent exit ray directions on the output aperture. In Fig. 3.12(b), the $RCS_{\theta\theta}$ at $\theta = 50^\circ$ is plotted as a function of the number of rays. At this larger angle, convergence is slower compared to the case in Fig. 3.12(a), again due to the increased number of bounces.

3.3.3 Radar cross section of large circular cylinders

Because the number of propagating modes increases exponentially with the radius of the cylinder, large aperture problems are not easily handled by the modal analysis. Modal analysis quickly becomes extremely cumbersome for large apertures because the propagation constant of each normal mode must be known. Since GO is a high frequency approximation, SBR is ideally suited for large aperture problems. Shown in Figs. 3.13 and 3.14 are the RCS plots of large circular cylinders. In Fig. 3.13, the cylinder has a diameter of 5λ and depth of 10λ . In Fig. 3.14, the cylinder has a diameter of 10λ and depth of 40λ . Fifteen rays per wavelength as suggested by the convergence study were used. The results were generated on the NSF Cray X-MP supercomputer at the University of Illinois.

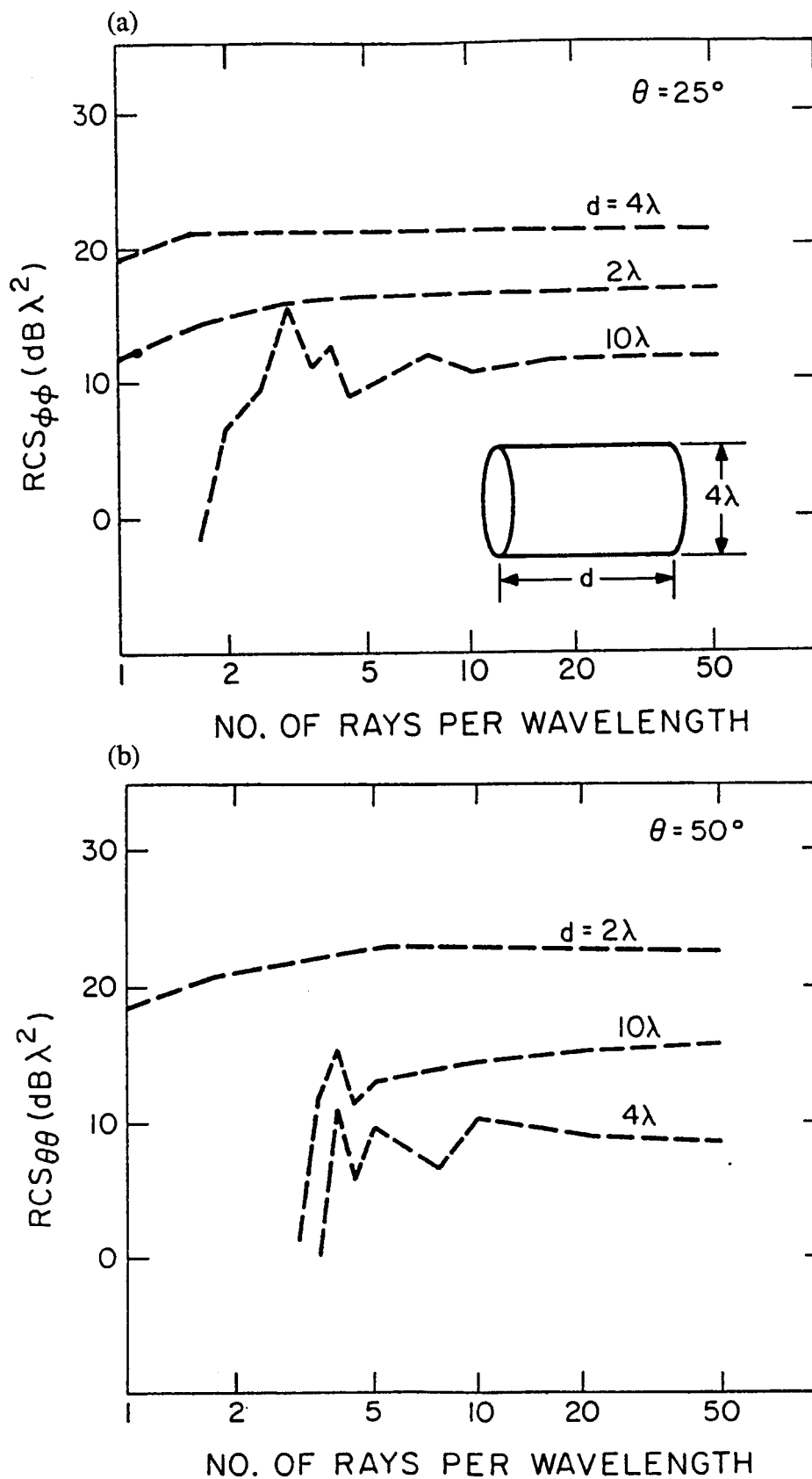


Fig. 3.12 Convergence of the RCS results as the ray density launch is increased.
 (a) $\theta = 25^\circ$, (b) $\theta = 50^\circ$.

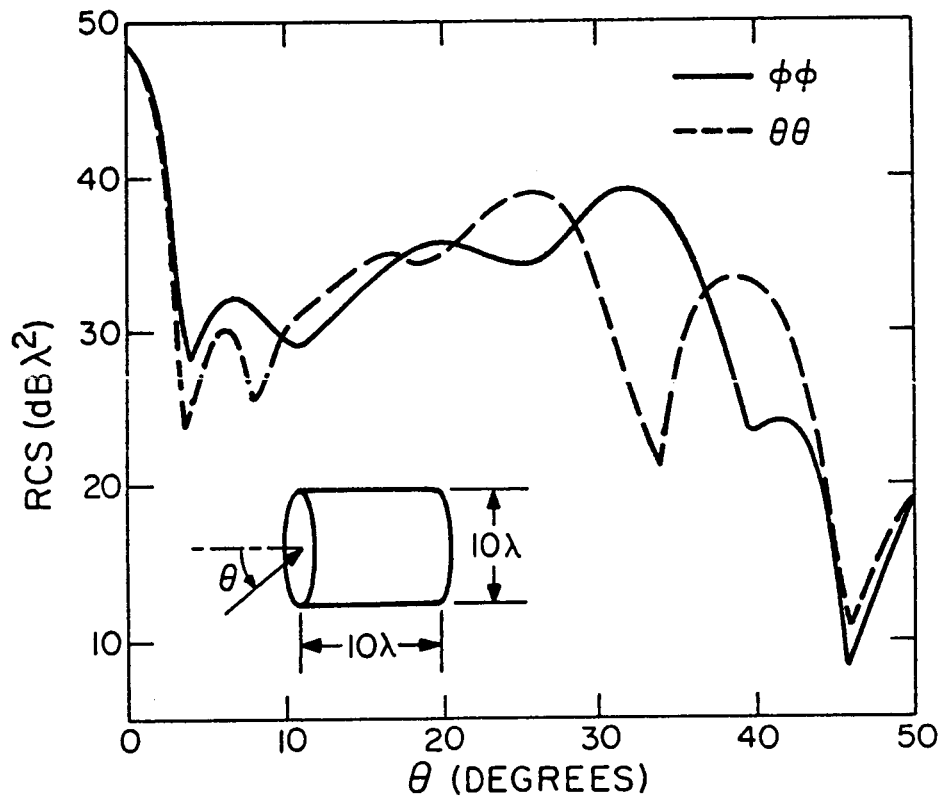


Fig. 3.13 RCS of a circular cylinder with diameter 10λ and depth 10λ .

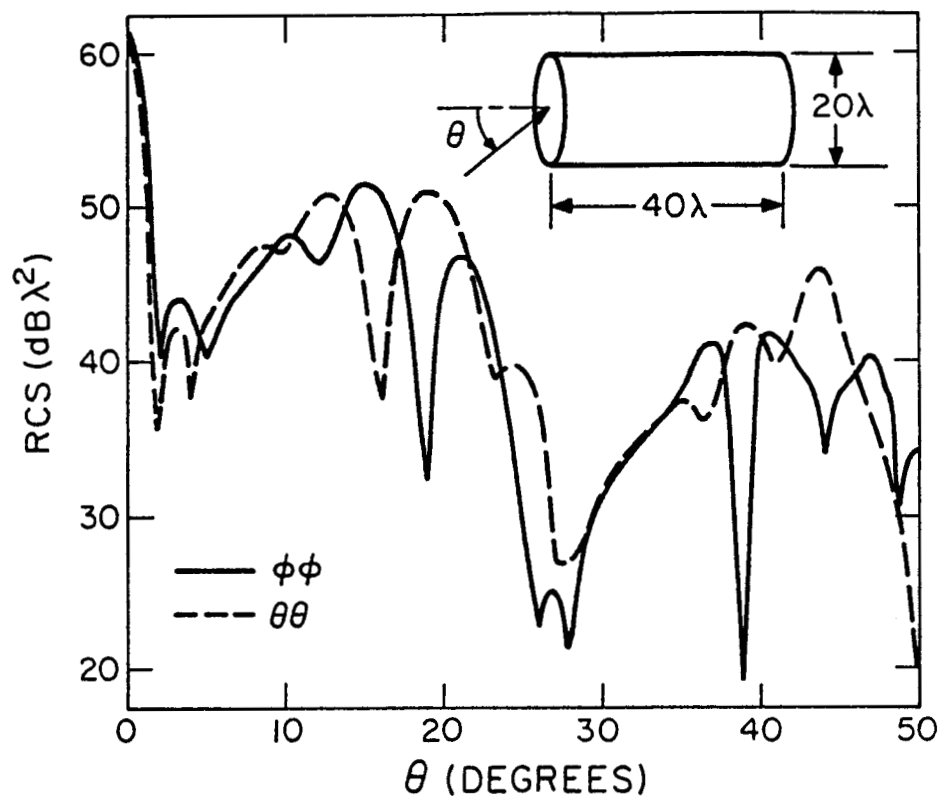


Fig. 3.14 RCS of a circular cylinder with diameter 20λ and depth 40λ .

3.4 Summary

A ray bouncing method was presented for calculating the electromagnetic scattering from an arbitrary open cavity. This approach is based on tracking a large number of rays launched into the cavity through the opening and determining the geometrical optics field associated with each ray by taking into consideration the (i) geometrical divergence factor, (ii) polarization, and (iii) material loading of the cavity walls. The contributions to the backscattered field from individual rays launched into the cavity are summed up to obtain the total internal RCS of the cavity. It was shown that the RCS results obtained by the ray approach agree well with those for the modal analysis even for a small 4λ cavity.

CHAPTER 4

RADAR CROSS SECTION REDUCTION OF CAVITIES BY SHAPING

4.1 Introduction

In addition to coating with lossy or absorbing materials, another method for reducing the RCS of a target is the proper shaping of the target. Through the use of shaping and radar absorbing materials, the RCS of a B-1 bomber is two orders of magnitude less than that of a B-52 [35]. A target should not have any flat, cylindrical, or conical surfaces which might be illuminated by the incident radar field along the normal to the target. An example of a target shape that yields a low RCS value over a wide range of incidence angles is the cone-sphere [1]. This chapter examines the effects of shaping, specifically, the effects of longitudinal bending, on the RCS of cylindrical cavities by applying the SBR method developed in Chapter 3.

For a large (relative to wavelength) flat-plate terminated cylinder, there is a large RCS value at near axial incidence due to the reflection from the termination (for examples, see Figs. 3.13 and 3.14). The near axial RCS of such structures can be reduced by a smooth gradual bending of the cylindrical axis. One such longitudinal bend, an S-bend, can be described by a half cosine function. For a cylindrical cavity with the cavity aperture on the x-y plane, the body restricted to the $z \leq 0$ half-space, and the cylindrical axis coincident with the z-axis (e.g., Fig. 3.1), the axis of the cylinder is deformed to

$$(x_c, y_c) = (0., H/2 [\cos(\pi z/d)] - 1) \quad \text{for } 0 \leq z < -d \quad (4.1)$$

where H is the amount of offset and d is the depth of the cavity. If H is greater than the largest radii of the aperture, no GO ray at axial incidence will directly reflect from the termination plate.

Two cavity geometries and their corresponding S-bend geometries will be considered. First is a circular cylinder terminated by a flat shorting plate. The second is a cylindrical waveguide with a triangular aperture and a circular end-plate. The transition extending from the triangular cross section to the circular cross section is smooth. The SBR method is currently the only available viable method for computing the RCS for such geometries. Section 4.2 will describe the mathematics of the cavities and their SBR implementation. Numerical results will be presented in Sec. 4.3.

4.2 Cavity Geometries

In this section, the mathematical descriptions of the cavities to be analyzed will be presented. Section 4.4.2 describes the straight and S-bend circular cylinders. The formulation for the triangular-to-circular waveguide is given in Sec. 4.4.3.

4.2.1 Circular cylinder

The terminated circular cylinder and S-bend circular cylinder are shown in Fig. 4.1. The surface for the straight cylinder is described by

$$\begin{aligned} x^2 + y^2 &= a^2 && \text{for } 0 \leq z < -d \\ x^2 + y^2 &\leq a^2 && \text{for } z = -d \end{aligned} \quad (4.2)$$

where a is the radius and d is the depth of the cylinder. The equation for a terminated S-bend circular cylinder is given by

$$\begin{aligned} x^2 + (y - H/2 [\cos(\pi z/d)] - 1)^2 &= a^2 && \text{for } 0 \leq z < -d \\ x^2 + (y - H)^2 &\leq a^2 && \text{for } z = -d \end{aligned} \quad (4.3)$$

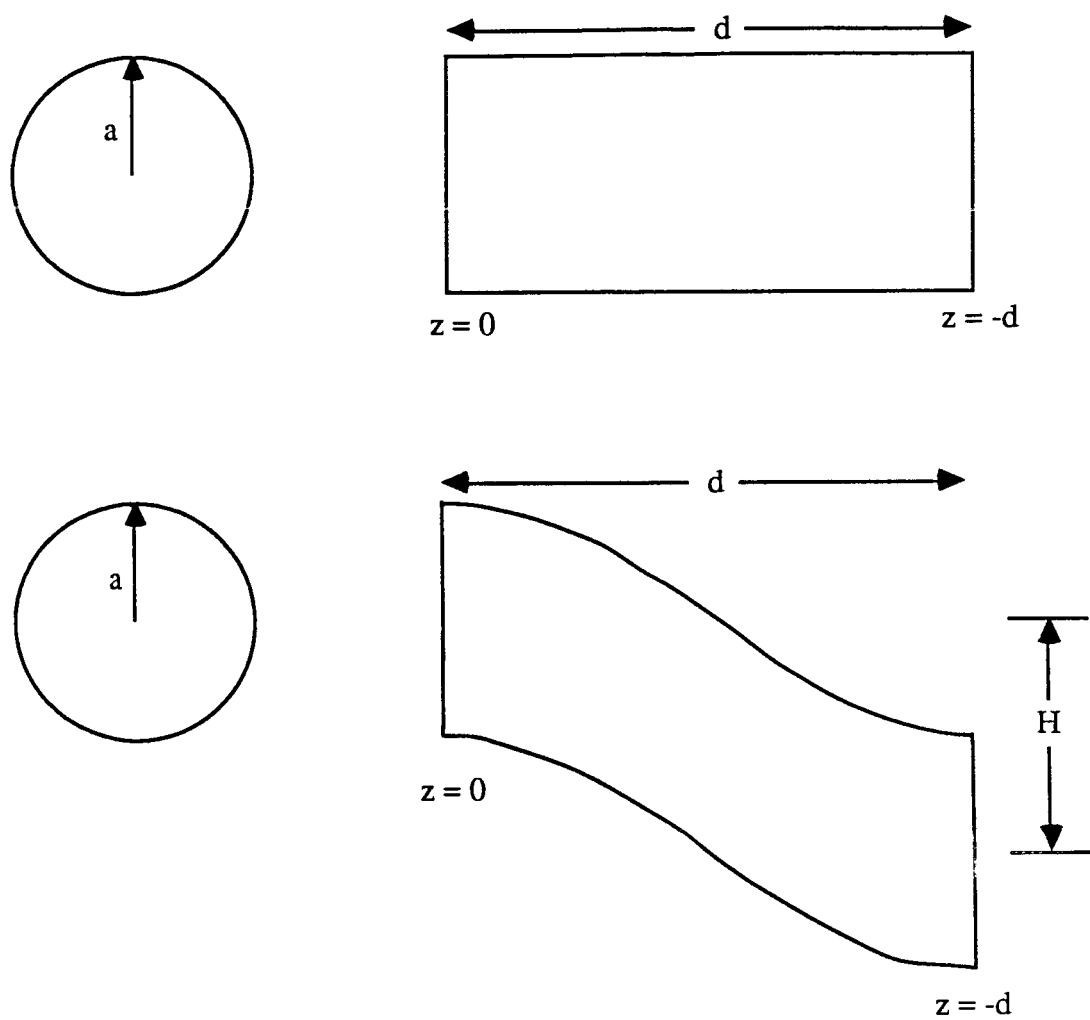


Fig. 4.1 Circular cylinder and S-bend circular cylinder.

where H is the amount of offset of the end-plate with respect to the aperture. If $H = a$, the offset of the end-plate is exactly one diameter. When $H = 0$, (4.3) reduces to (4.2). Note that for the S-bend cylinder, a cross-sectional view at any $z = \text{constant}$ plane also yields a perfect circle.

An impact point (x_1, y_1, z_1) of a ray with the cavity is found from solving the equation of the cavity parametrically with the equation of the ray

$$(x, y, z) = (x_0, y_0, z_0) + (s_1, s_2, s_3) t \quad (4.4)$$

where

(x_0, y_0, z_0) is the initial starting point or the previous reflection point or the ray,

(s_1, s_2, s_3) is the direction vector of the ray.

For the straight circular cylinder, the solution can be given in closed form by

$$t = (-B + \sqrt{B^2 - 4AC}) / 2A \quad (4.5)$$

where

$$A = s_1^2 + s_2^2$$

$$B = 2(s_1 x_0 + s_2 y_0)$$

$$C = x_0^2 + y_0^2 - a^2 .$$

The coordinate (x_1, y_1, z_1) is then found by substituting (4.5) into (4.4). For the S-bend circular cylinder, the simultaneous solution to (4.3) and (4.4) is found numerically.

In the computation of the curvature matrix, the obvious choice for the (u, v) coordinates of the straight cylinder is $(u, v) = (\phi, z)$, where ϕ is the standard angular coordinate in a cylindrical coordinate system. For the end-plate at $z=-d$, (u, v) is set to $(u, v) = (x, y)$. The cavity can then be described by

$$\begin{aligned}\vec{r} &= (x, y, z) = (a \cos \phi, a \sin \phi, z) && \text{for } 0 \leq z < -d \\ \vec{r} &= (x, y, -d) \text{ with } x^2 + y^2 \leq a && \text{for } z = -d .\end{aligned}\quad (4.6)$$

The curvature matrix $\bar{\bar{Q}}^\Sigma$ for the cavity, defined by (3.18), can be easily shown to be

$$\bar{\bar{Q}}^\Sigma = \begin{bmatrix} 1/R & 0 \\ 0 & 0 \end{bmatrix} \quad \text{for } 0 \leq z < -d \quad (4.7)$$

$$\bar{\bar{Q}}^\Sigma = \begin{bmatrix} 0 & 0 \\ 0 & 0 \end{bmatrix} \quad \text{for } z = -d .$$

For the S-bend, define an angle ϕ such that

$$\begin{aligned}x &= a \cos \phi \\ y - H/2 [\cos(\pi z/d)] - 1 &= a \sin \phi .\end{aligned}\quad (4.8)$$

In other words, ϕ can be described by

$$\phi = \tan^{-1} \left\{ (y - H/2 [\cos(\pi z/d)] - 1) / x \right\} . \quad (4.9)$$

In this case, the choice for (u, v) is now (ϕ, z) , and

$$\begin{aligned}\vec{r} &= (x, y, z) = (a \cos \phi, a \sin \phi + H/2 [\cos(\pi z/d)], z) && \text{for } 0 \leq z < -d \\ \vec{r} &= (x, y, -d) \text{ with } x^2 + y^2 \leq a && \text{for } z = -d .\end{aligned}\quad (4.10)$$

The curvature matrix $\bar{\bar{Q}}^\Sigma$ can be found from (3.18).

4.2.2 Triangle-to-circle transition waveguide

A segment of the line on the $z = 0$ plane described by $y = mx + b$ can be smoothly transformed in the $-z$ direction to an arc of the circle described by $x^2 + y^2 = a^2$ on the $z = -d$ plane with the following equation:

$$\alpha z (x^2 + y^2 - a^2) + (z + d) (y - mx - b) = 0 \quad \text{for } 0 \leq z < -d \quad (4.11)$$

where α is a transition parameter. This can also be represented in cylindrical coordinates by

$$\rho(\phi, z) = -g(z)(\sin \phi - m \sin \phi) + \sqrt{[g(z)(\sin \phi - m \sin \phi)]^2 + a^2 + 2g(z)b} \quad (4.12)$$

$$\text{where } g(z) = \frac{z + d}{2\alpha z} \quad \text{for } 0 \leq z < -d$$

Figure 4.2 shows such a transition for $\alpha = 0.05$, $d = 45$, $m = 0$, $b = -16/\sqrt{3}$, and $a = 15$, where ϕ is restricted to $-150^\circ \leq \phi \leq -30^\circ$. Several of these surfaces can be combined to form a smooth transition from an arbitrary polygon to a circle. Care must be taken to insure continuity of the structure at the surface junctions. This is accomplished with the proper choice of α .

Figure 4.3 shows such a waveguide structure with a triangle-to-circle transition. For a triangular aperture with side s , center at $(x_c, y_c) = (0., 0.)$, and base parallel to the x -axis, the parameters that define the waveguide are

$$\begin{array}{llll} \alpha_1 = \alpha_0 & m_1 = 0.0 & b_1 = -s/(2\sqrt{3}) & -150^\circ \leq \phi \leq -30^\circ \\ \alpha_2 = 2\alpha_0 & m_2 = -\sqrt{3} & b_2 = s/\sqrt{3} & -30^\circ \leq \phi \leq 90^\circ \\ \alpha_3 = 2\alpha_0 & m_3 = \sqrt{3} & b_3 = s/\sqrt{3} & 90^\circ \leq \phi \leq -150^\circ \end{array} \quad (4.13)$$

In Fig. 4.4, cross-sectional cuts at various lengths along the waveguide for $\alpha_0 = 0.05$ are shown.

The equation for the S-bend transition is

$$\alpha z (x^2 + (y - H/2 [\cos(\pi z/d)])^2 - a^2) + (z + d) (y - H/2 [\cos(\pi z/d)] - mx - b) = 0 \quad \text{for } 0 \leq z < -d \quad (4.14)$$

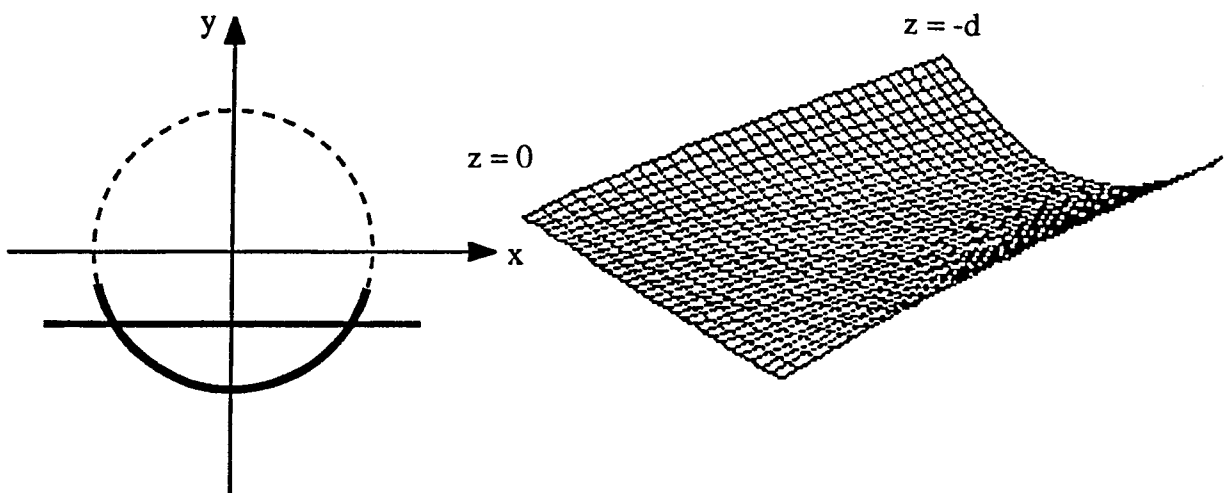


Fig. 4.2 Surface with transition from line segment to arc of circle. Circle is centered about $(x,y) = (0,0)$.

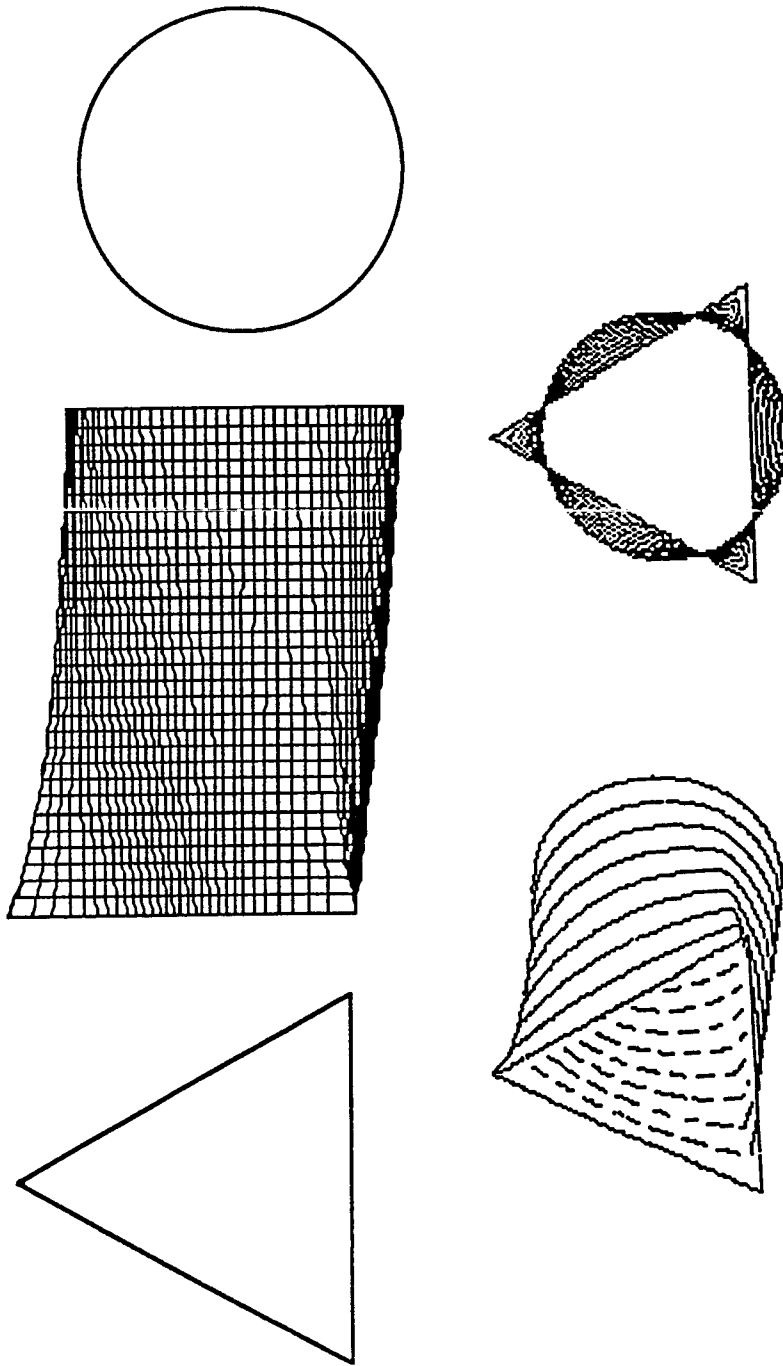


Fig. 4.3 Triangle-to-circle transition waveguide.

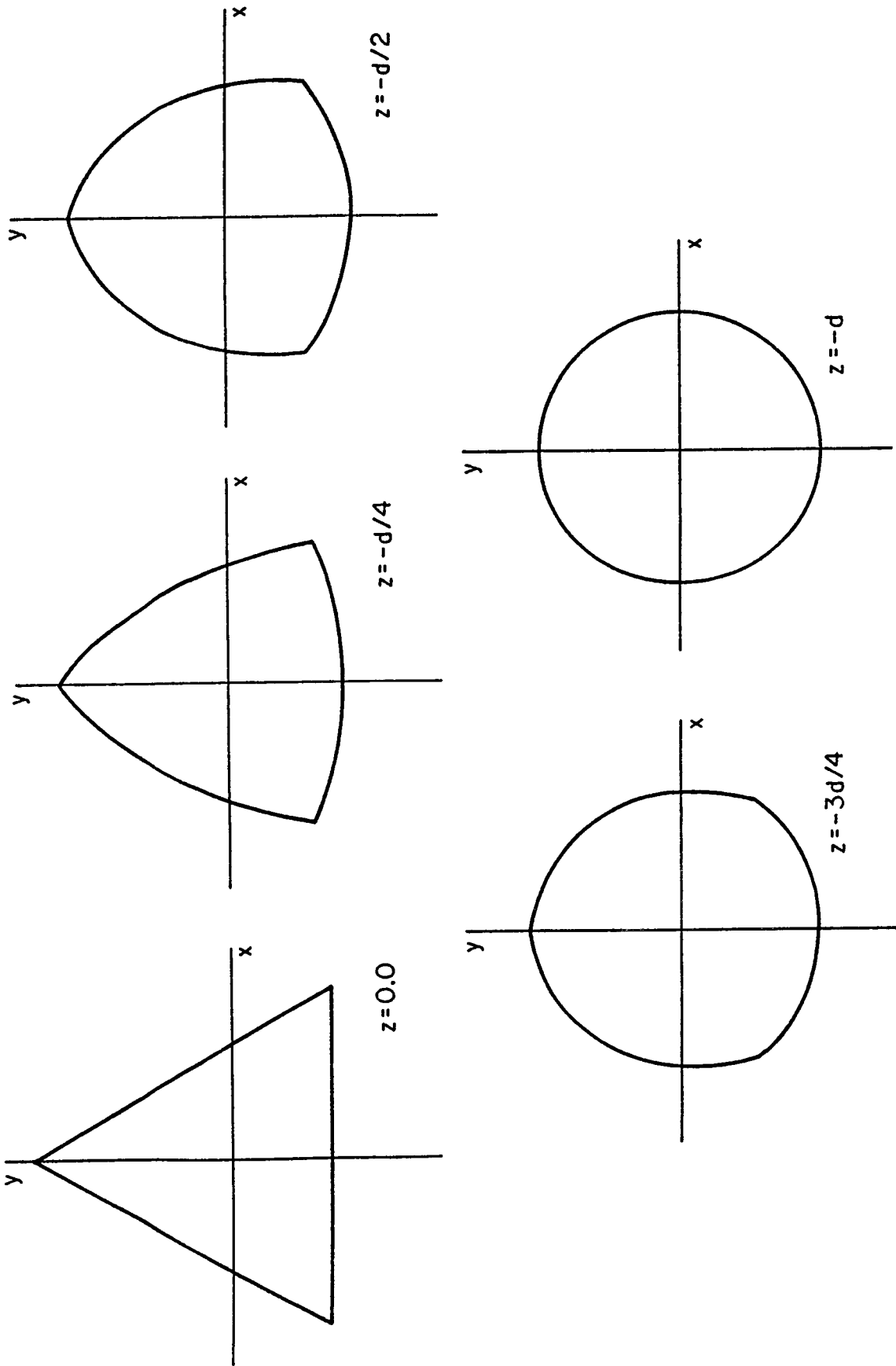


Fig. 4.4 Cross-sectional view of transition waveguide at various distances along the axial direction.

Figure 4.5 shows the surface shown in Fig. 4.2 with the addition of an offset $H = 27$. Figure 4.6 shows the S-bend triangle-to-circle transition waveguide. In computing the surface curvature matrix, define φ from

$$x = \rho(\varphi, z)\cos\varphi \quad (4.15)$$

$$y - H/2 [\cos(\pi z/d) - 1] = \rho(\varphi, z) \sin \varphi$$

where $\rho(\varphi, z)$ is given by (4.12). Thus, φ is exactly equivalent to (4.9). The choice of (u, v) coordinates, as for the S-bend circular cylinder, is $(u, v) = (\varphi, z)$. The surface given parametrically by (φ, z) is then

$$\vec{r} = (x, y, z) = (\rho(\varphi, z)\cos \varphi, \rho(\varphi, z) \sin \varphi + H/2 [\cos(\pi z/d)], z) \quad (4.16)$$

for $0 \leq z < -d$.

Equations (4.14), (4.15), and (4.16) reduce to a straight transition waveguide when $H = 0$. The intersection points for the rays with the cavity is determined from the solution of simultaneously solving (4.4) and (4.14). The equations for the flat end-plate at $d = 0$ are identical to the second half of (4.2), (4.3), (4.6), and (4.7) in Sec. 4.2.2.

4.3 Numerical Results

RCS computation results will be presented for the end-plate terminated straight and S-bend circular waveguides and the straight and S-bend triangle-to-circle transition waveguides. For the circular waveguides, the diameter used is 5λ across and the length along the z -axis is 10λ . The diameter offset parameters H for the circular S-bend are 2.5λ and 5λ , so that the back plate of the cylinder is exactly one half and one diameter below the aperture, respectively. For the transition waveguide, the length of one side of the triangular aperture is 5.4λ and the

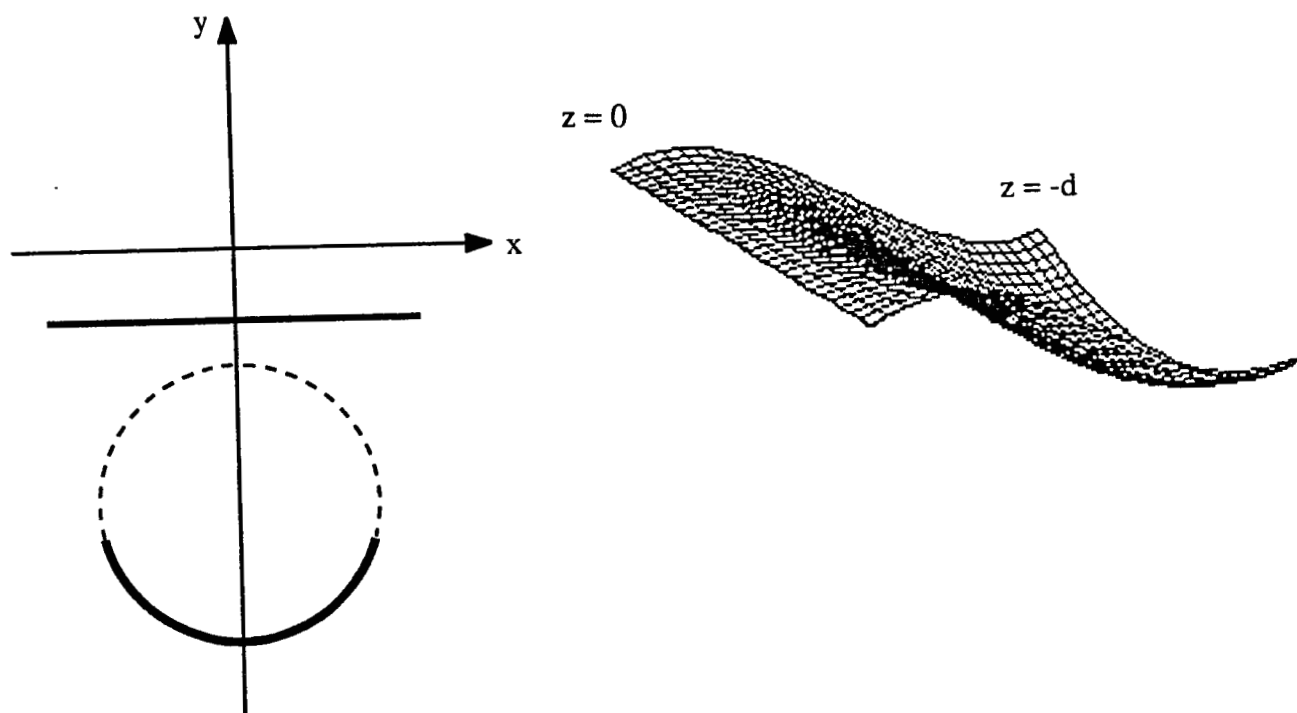


Fig. 4.5 Surface with transition from line segment to arc of circle. Center is offset along the y axis.

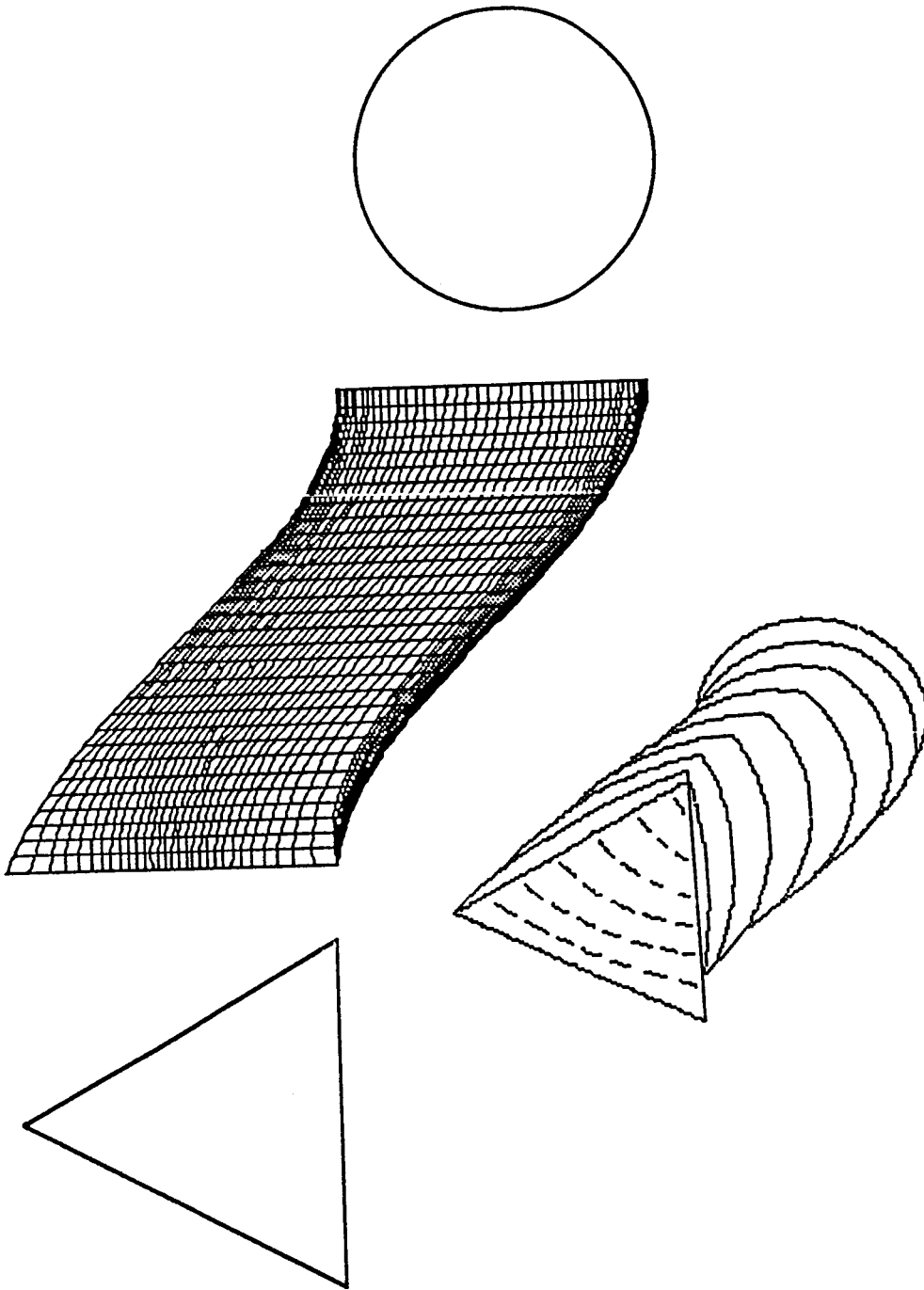


Fig. 4.6 Triangle-to-circle S-bend transition waveguide.

diameter of the end circle is 4.5λ . The length along the z -axis is 6.75λ , and the offset for the S-bend case is 4.05λ . A ray entering the cavity at axial incidence will not directly hit the circular end-plate.

4.3.1 Exit points and ray paths

Shown in Fig. 4.7 are the exit ray pictures on the aperture plane for the circular straight and S-bend cavities. Each dot represents the point on the aperture plane where a ray exits the cavity. The incident rays are launched from a uniformly spaced grid on the aperture. At axial incidence ($\theta = \phi = 0^\circ$), the incident rays reflect straight back from the end plate, and the exit ray positions are coincident with the input ray positions on the aperture plane. For the S-bend geometry, because there is no direct reflection, the output rays are dispersed even at axial incidence. Figure 4.8 shows some exit ray pictures for the straight and S-bend transition waveguides.

Figures 4.9 and 4.10 show the ray paths for a single individual ray for the S-bend circular cavity. The figures show the ray path from three different perspectives. Each dot represents a reflection point inside the cavity. The area ratio given on each figure is the ratio of output area to input area for the differential ray tube associated with the ray, calculated from (3.29). A typical ray can take anywhere from a few bounces to well over a hundred bounces for the given geometry. The ray in Fig. 4.9 takes 5 bounces inside the cavity while the ray in Fig. 4.10 takes 123 bounces inside the cavity. Both rays represent a plane wave incoming at axial incidence. The ray in Fig. 4.10 is similar to a ray for the whisper gallery mode [36]. SBR is ideally suited for computer-aided design (CAD) systems in the sense that a high RCS in a particular aspect angle can be traced back to the contribution from a particular portion of the target through examination of the rays paths and field amplitudes. The particular portion of the

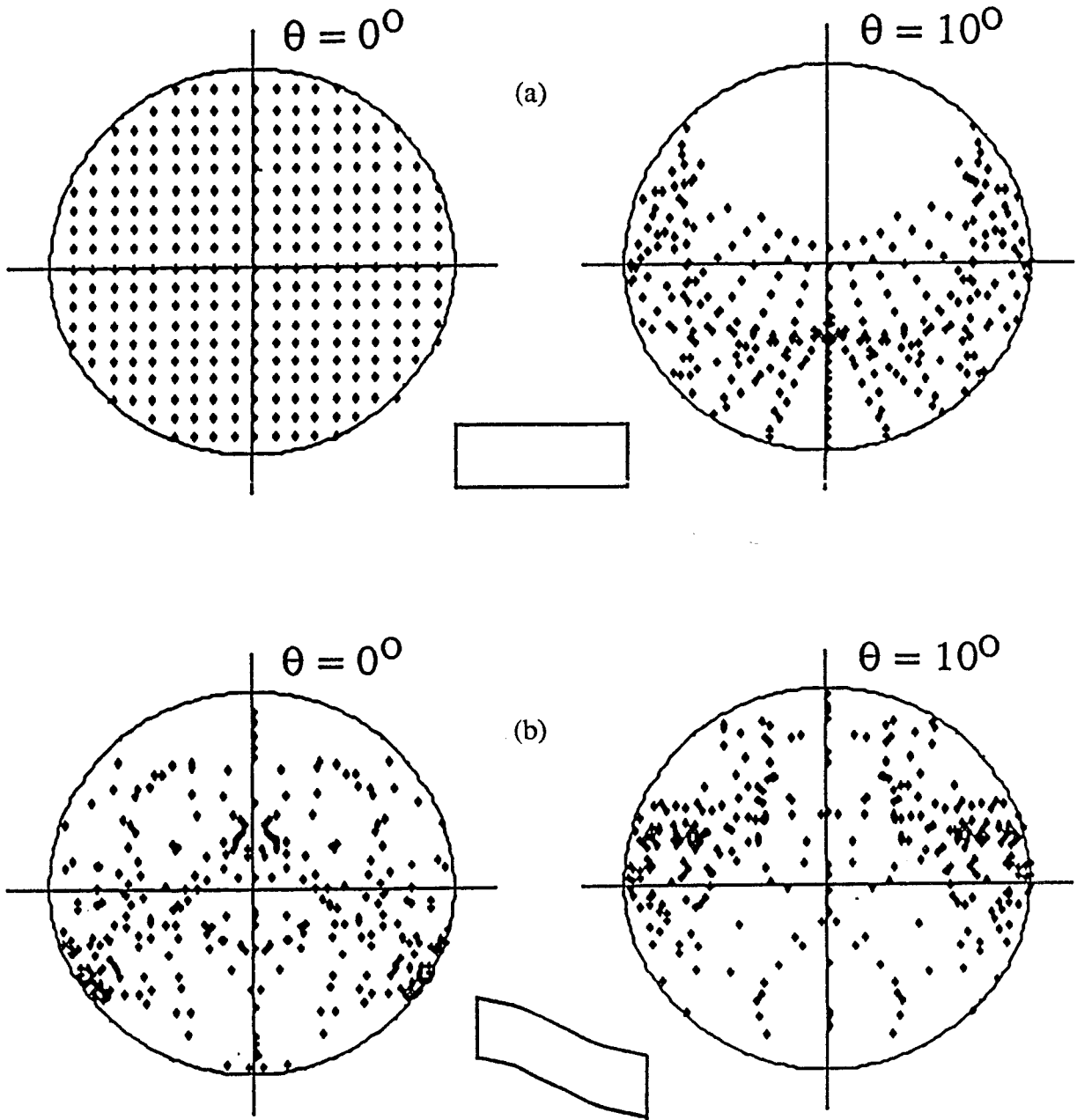


Fig. 4.7 Exit ray pictures for (a) circular cylinder with flat end-plate and (b) S-bend circular cylinder with flat end-plate.

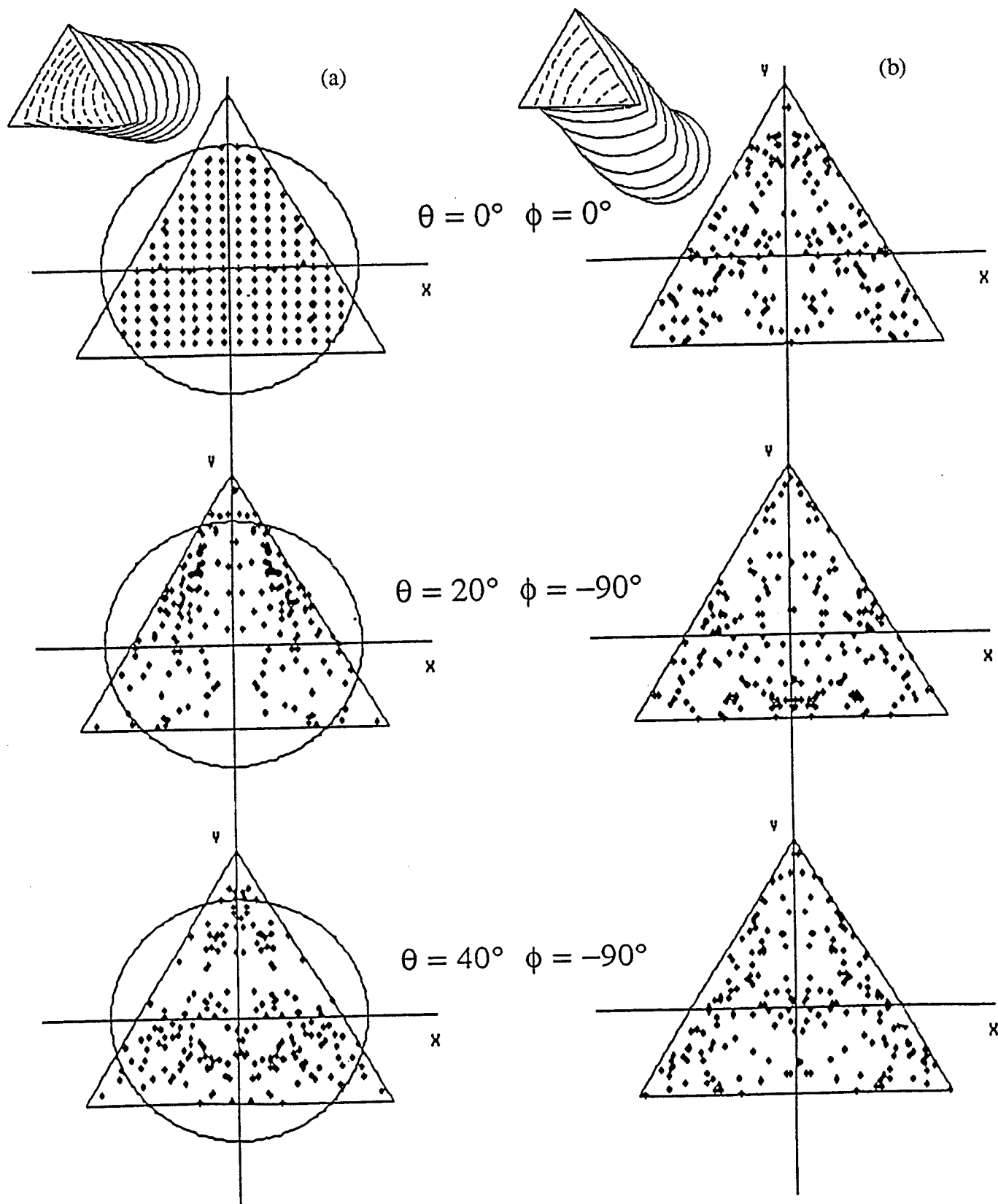


Fig. 4.8 Exit ray pictures for (a) straight triangle-to-circle transition waveguide with flat plate end-plate and (b) S-bend straight triangle-to-circle transition waveguide with flat end-plate.

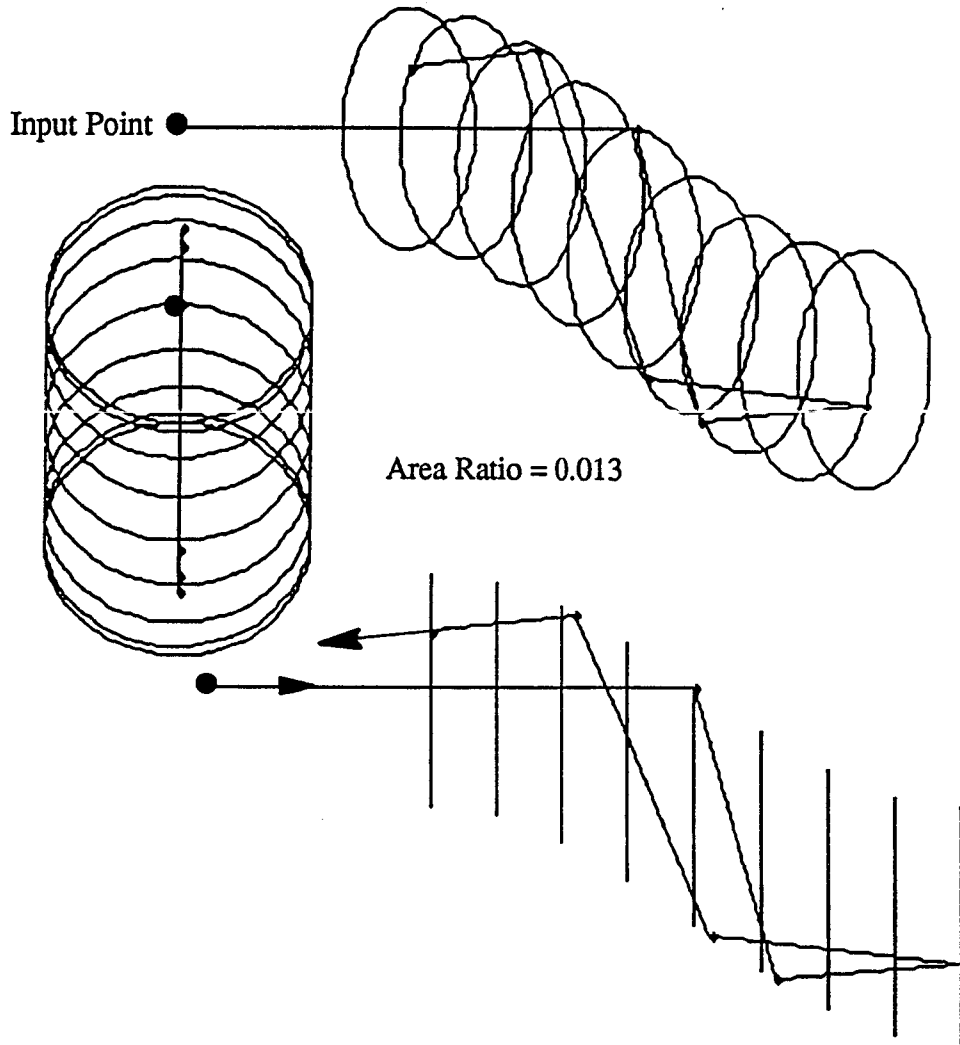


Fig. 4.9 Ray path in an S-bend circular cylinder (5λ offset).

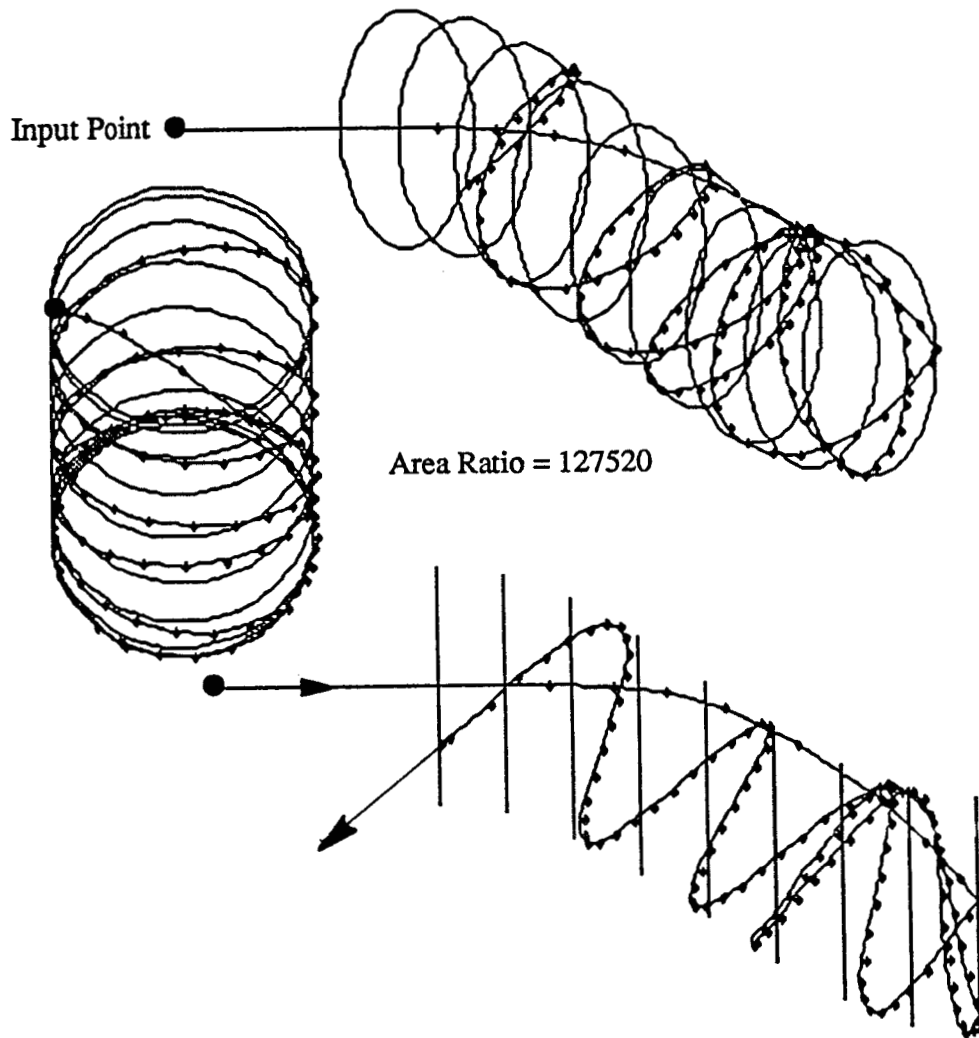


Fig. 4.10 Ray path in an S-bend circular cylinder (5λ offset).

target can then be reshaped or coated with absorbing material, and the RCS of the modified geometry can be recomputed.

Figure 4.11 shows the front aperture for the S-bend triangle-to-circle transition waveguide. Each dot represents an input position for a ray to be launched at axial incidence. Figures 4.12 - 4.17 show the individual ray paths. The number next to each dot in Fig. 4.11 indicates the number of the figure that shows the ray path for that particular input point. Again, the area ratio for each individual ray is given. Note for this sampling of six rays, the value of the area ratio varies from a low of 3.52 (Fig. 4.13) to a high of 477558 (Fig. 4.15). For highly curved closed cavities, a ray that takes a very high number of bounces generally has a very high area ratio due to a very low divergence factor product. No conclusion can be reached for rays that take only a few bounces. The ray in Fig. 4.12 has a higher area ratio than the ray in Fig. 4.16 despite making more bounces.

4.3.2 Radar cross section computations

Convergence of SBR for the S-bend circular cylinder is checked by increasing the number of rays launched into the cylinder. Figure 4.18 shows the BCS calculations for the 2.5λ offset S-bend cavity for an incident plane wave at $(\theta_i, \phi_i) = (10^\circ, -90^\circ)$. Figure 4.19 shows the BCS calculations for the 5.0λ offset case. A greater cavity bend requires a higher density of rays for convergent BCS calculations. Figures 4.20 and 4.21 show the BCS's for the straight and S-bend transition waveguides, respectively, for the same incident plane wave. Note that the S-bend transition waveguide requires twice the linear density for convergence over the straight waveguide. This results in a four-fold increase in computation time due to a corresponding increase in the number of rays. Figure 4.22 compares the calculated RCS for a 2.5λ offset S-bend cylinder against a straight circular cylinder. Figure 4.23 compares the calculated RCS for a 5.0λ offset S-bend cylinder against a straight circular cylinder. Though

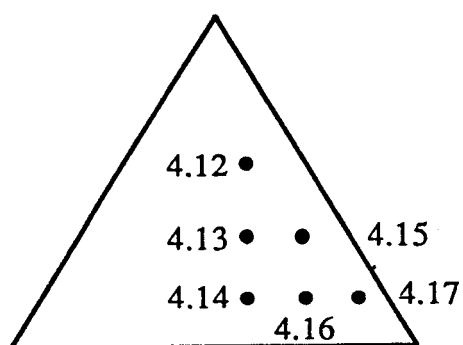


Fig. 4.11 Triangular aperture of transition waveguide. Each point corresponds to input point of ray for Fig. 4.12 - Fig. 4.17.

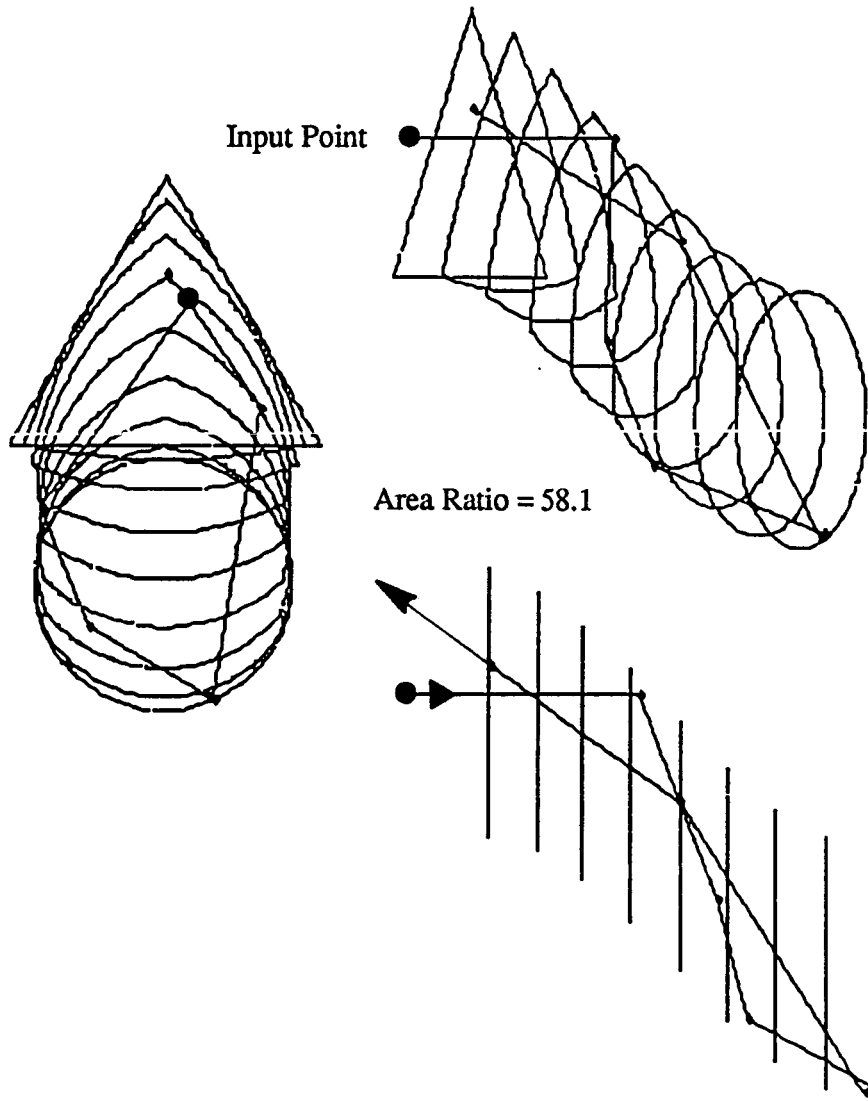


Fig. 4.12 Ray path in an S-bend triangle-to-circle transition waveguide.

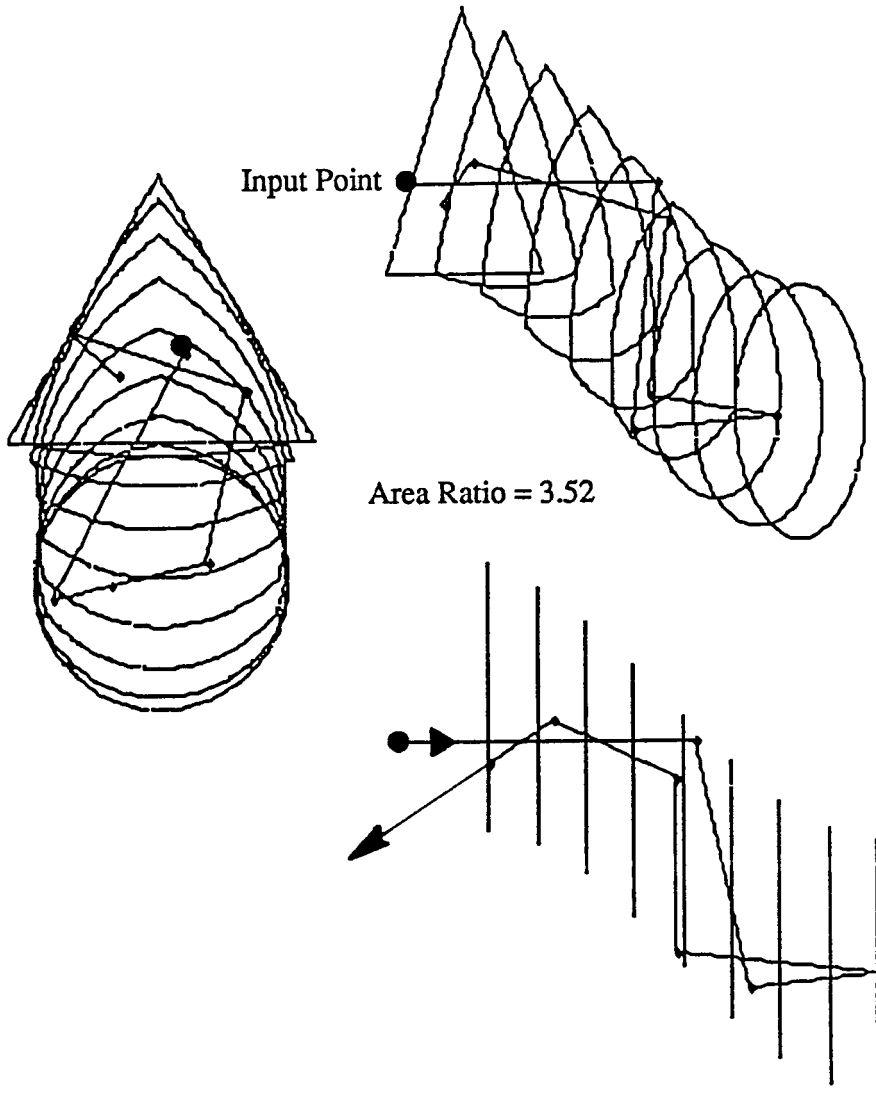


Fig. 4.13 Ray path in an S-bend triangle-to-circle transition waveguide.

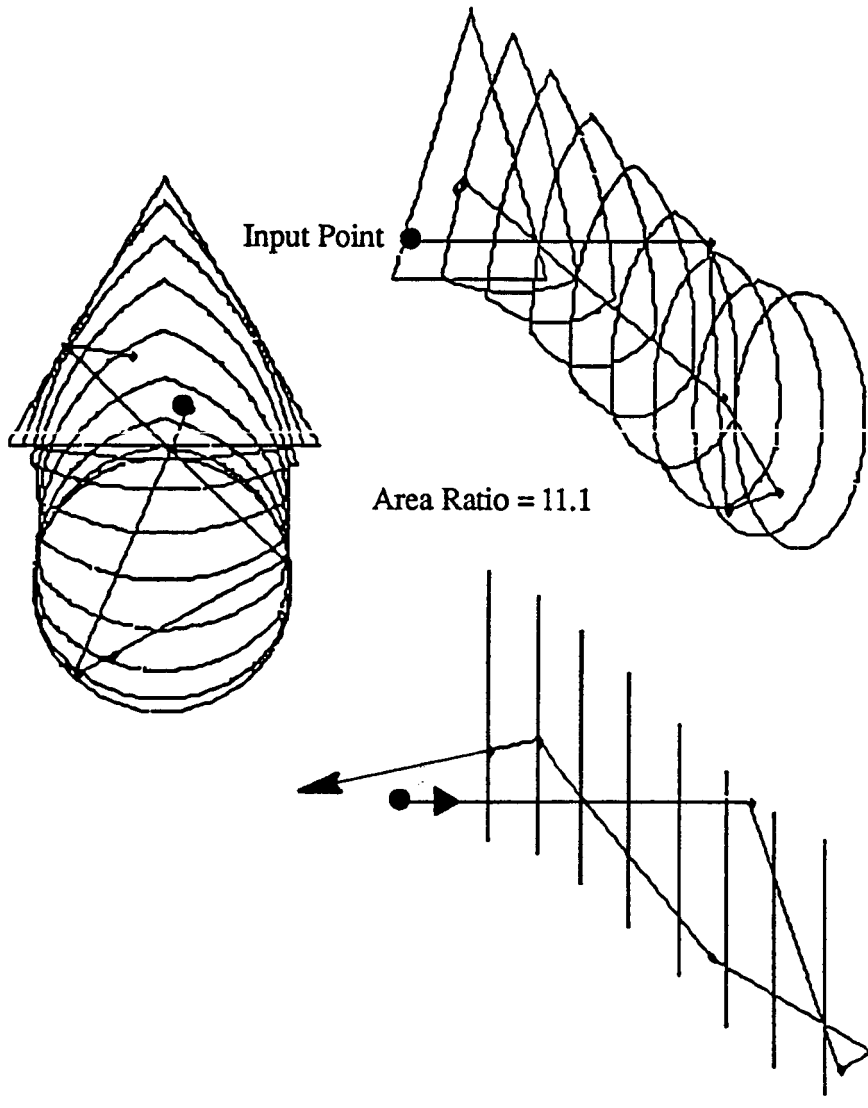


Fig. 4.14 Ray path in an S-bend triangle-to-circle transition waveguide.

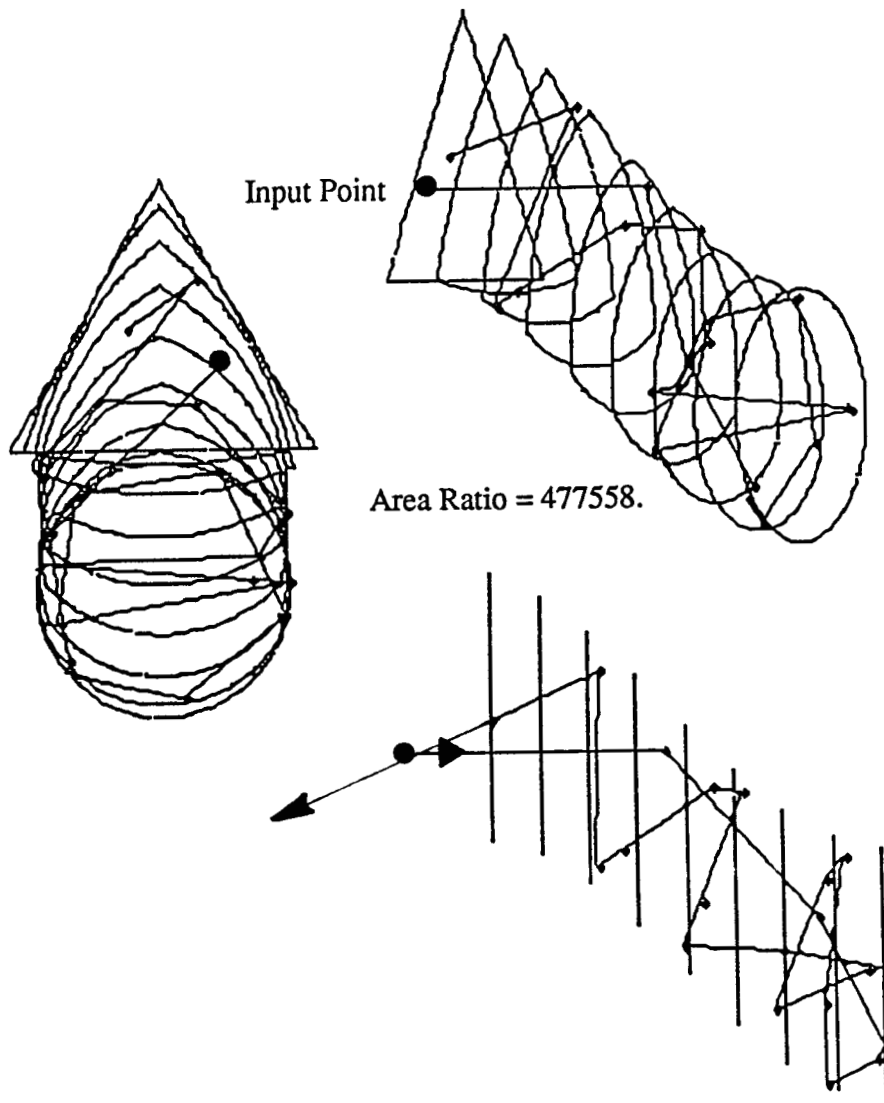


Fig. 4.15 Ray path in an S-bend triangle-to-circle transition waveguide.

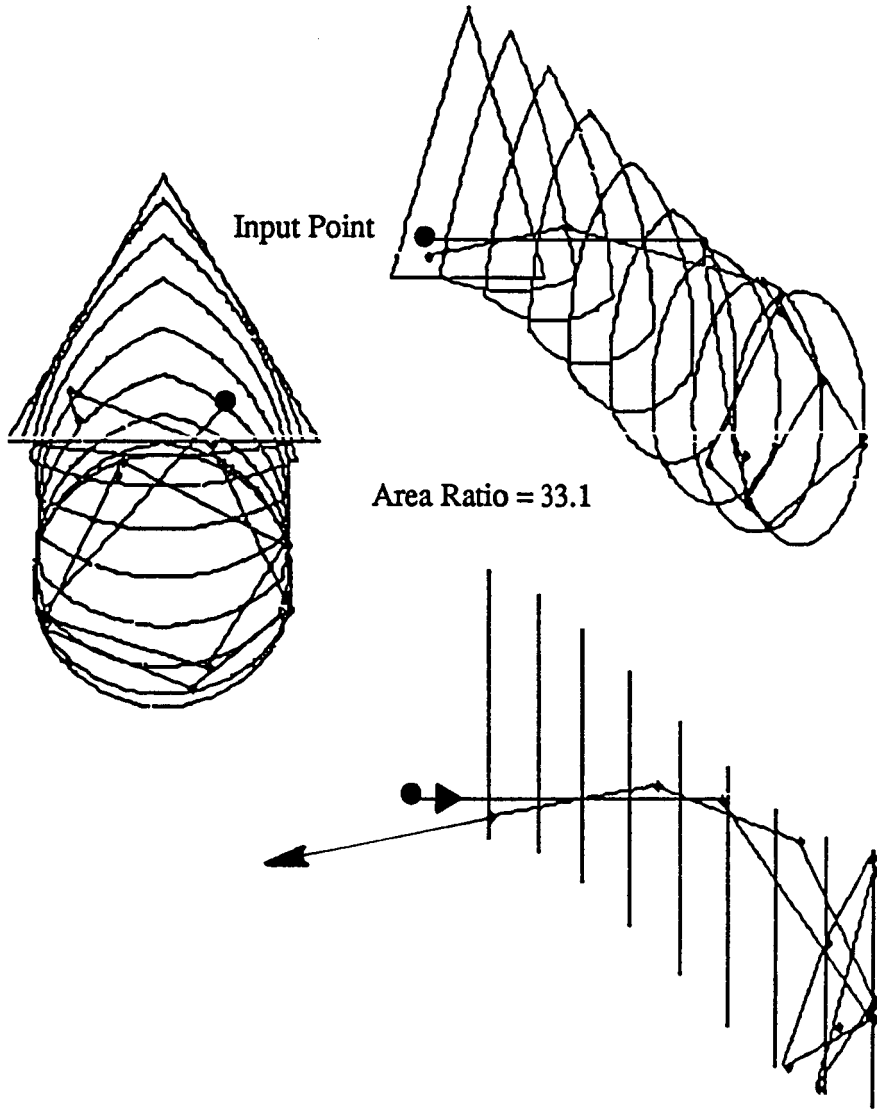


Fig. 4.16 Ray path in an S-bend triangle-to-circle transition waveguide.

C-2

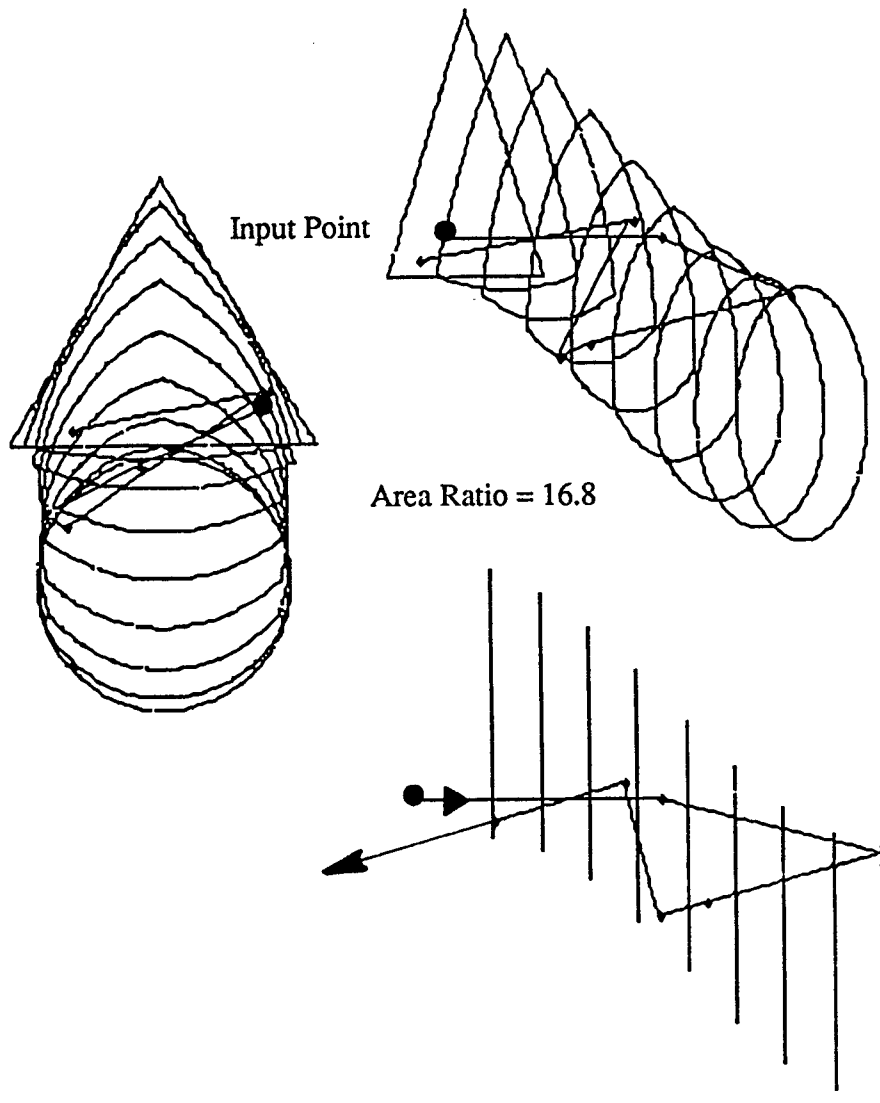
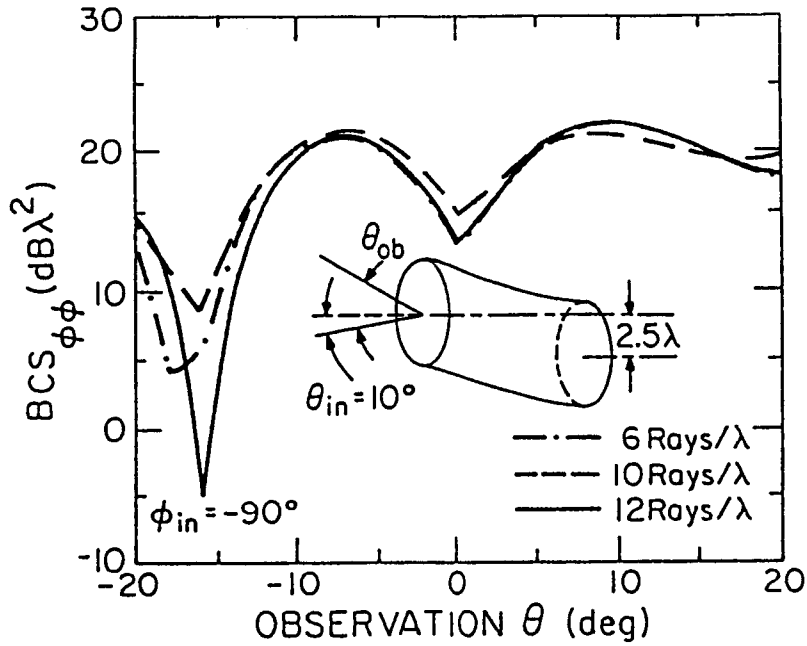


Fig. 4.17 Ray path in an S-bend triangle-to-circle transition waveguide.



(b) $\theta\theta$ -polarization

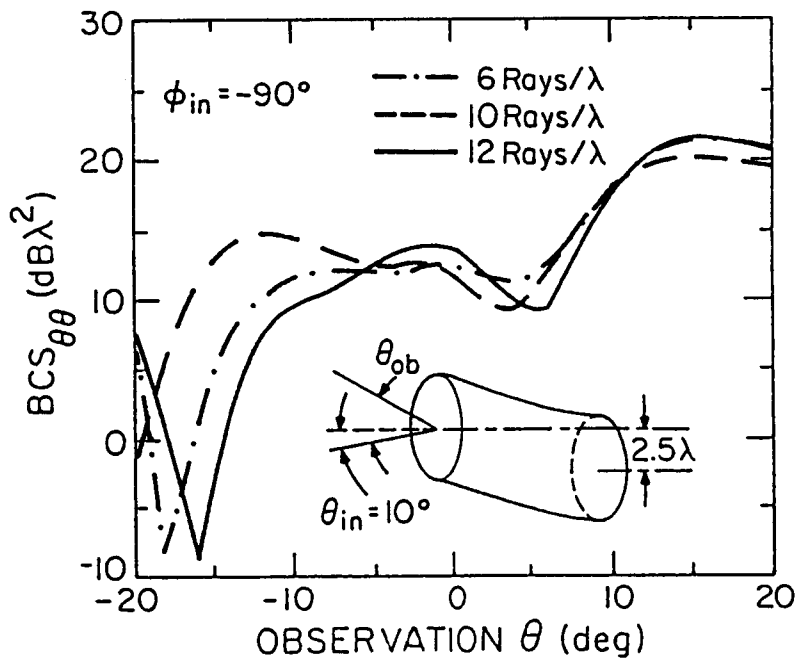


Fig. 4.18 BCS with different input ray densities for an S-bend cylinder with diameter of 5λ , depth of 10λ , and offset of 2.5λ . Direction of incidence $(\theta_{in}, \phi_{in}) = (10^\circ, -90^\circ)$. (a) $\phi\phi$ -polarization, (b) $\theta\theta$ -polarization.

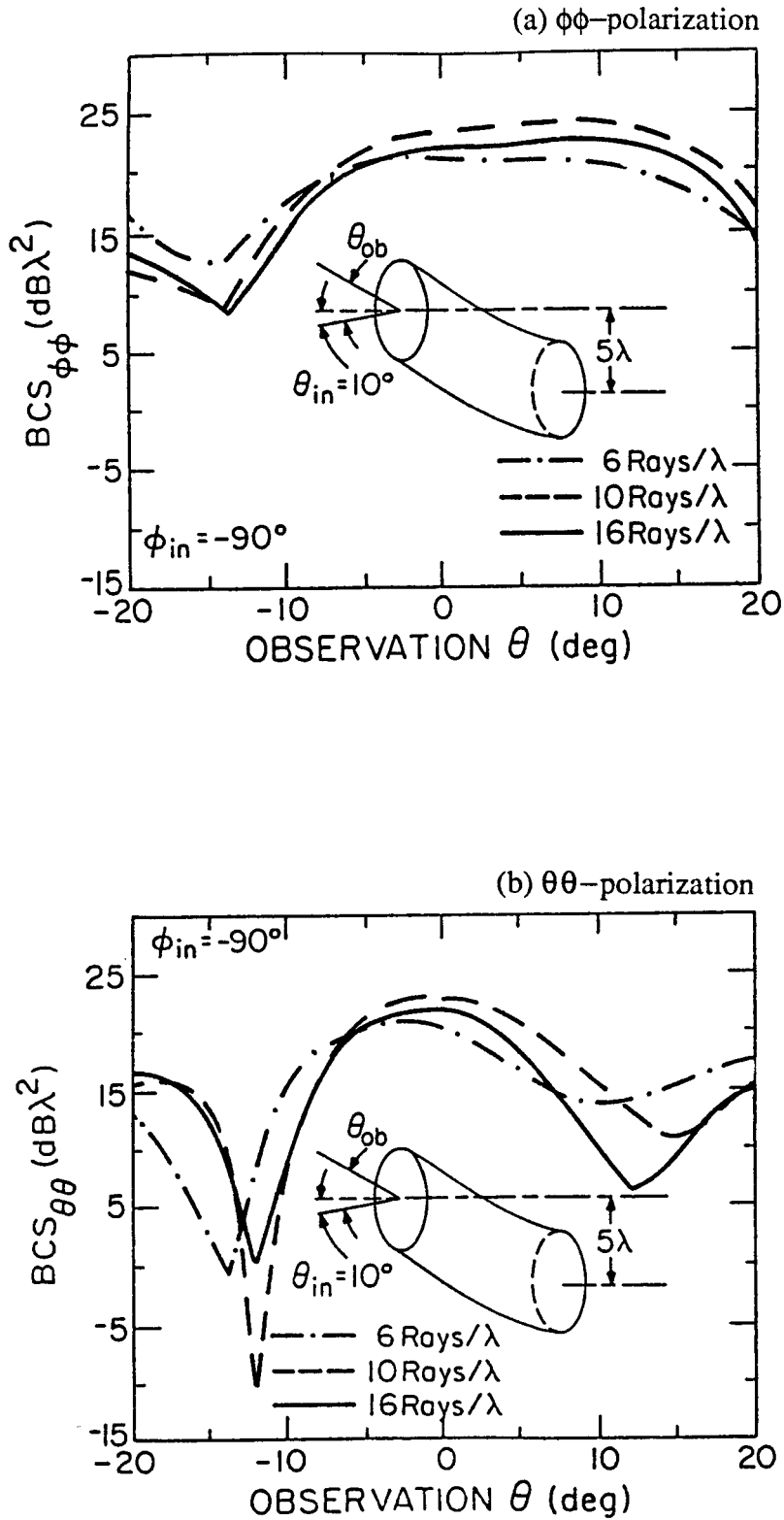


Fig. 4.19 BCS with different input ray densities for an S-bend cylinder with diameter of 5λ , depth of 10λ , and offset of 5.0λ . Direction of incidence $(\theta_{in}, \phi_{in}) = (10^\circ, -90^\circ)$. (a) $\phi\phi$ -polarization, (b) $\theta\theta$ -polarization.

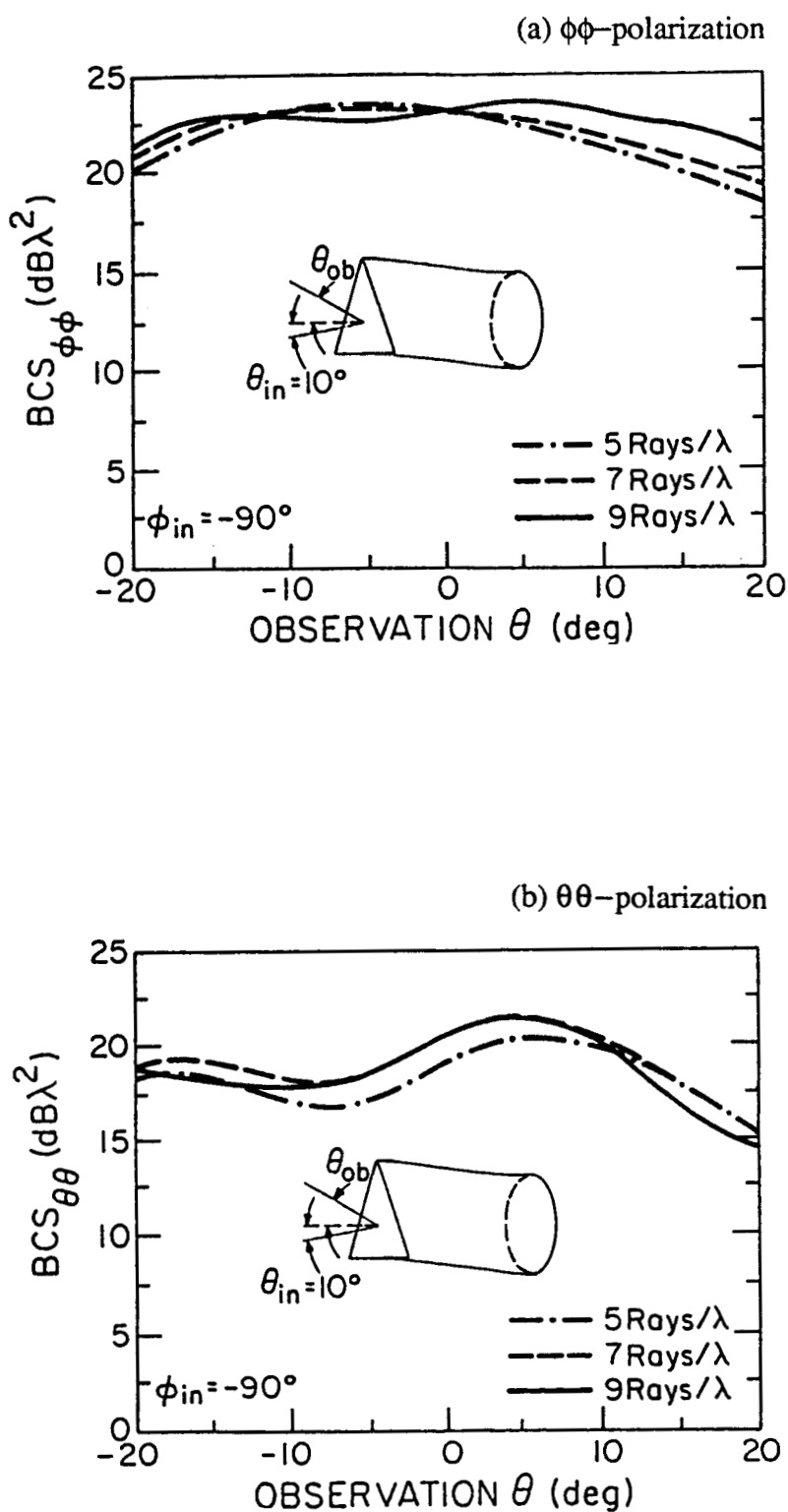


Fig. 4.20 BCS with different input ray densities for a triangle-to-circle transition waveguide with triangle side of 5.4λ , end circle diameter of Fig. 4.5 λ , and depth of 6.75λ . Direction of incidence $(\theta_{in}, \phi_{in}) = (10^\circ, -90^\circ)$. (a) $\phi\phi$ -polarization, (b) $\theta\theta$ -polarization.

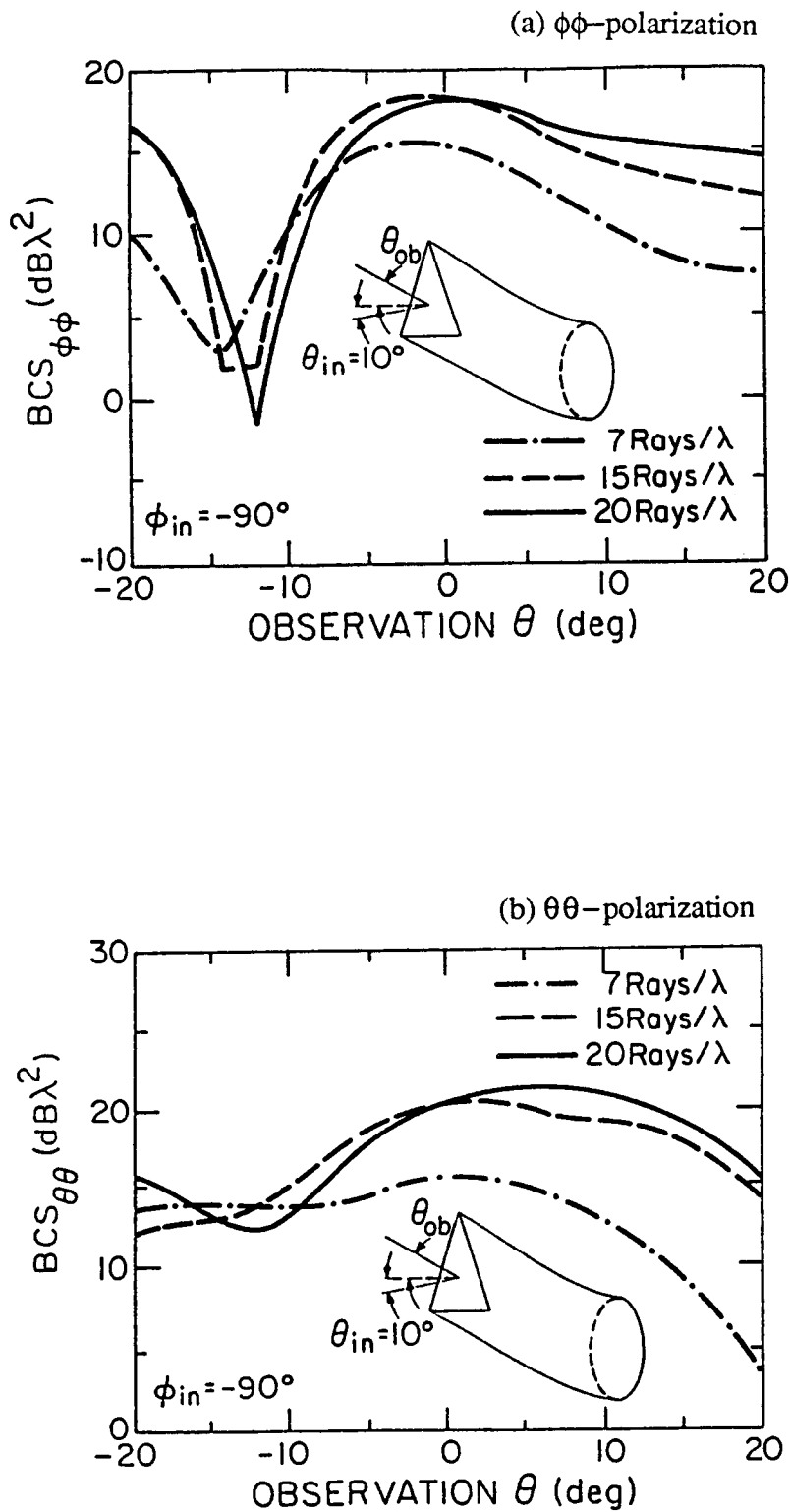


Fig. 4.21 BCS with different input ray densities for an S-bend triangle-to-circle transition waveguide with triangle side of 5.4λ , end circle diameter of 4.5λ , depth of 6.75λ , and offset of 4.05λ . Direction of incidence $(\theta_{in}, \phi_{in}) = (10^\circ, -90^\circ)$. (a) $\phi\phi$ -polarization, (b) $\theta\theta$ -polarization.

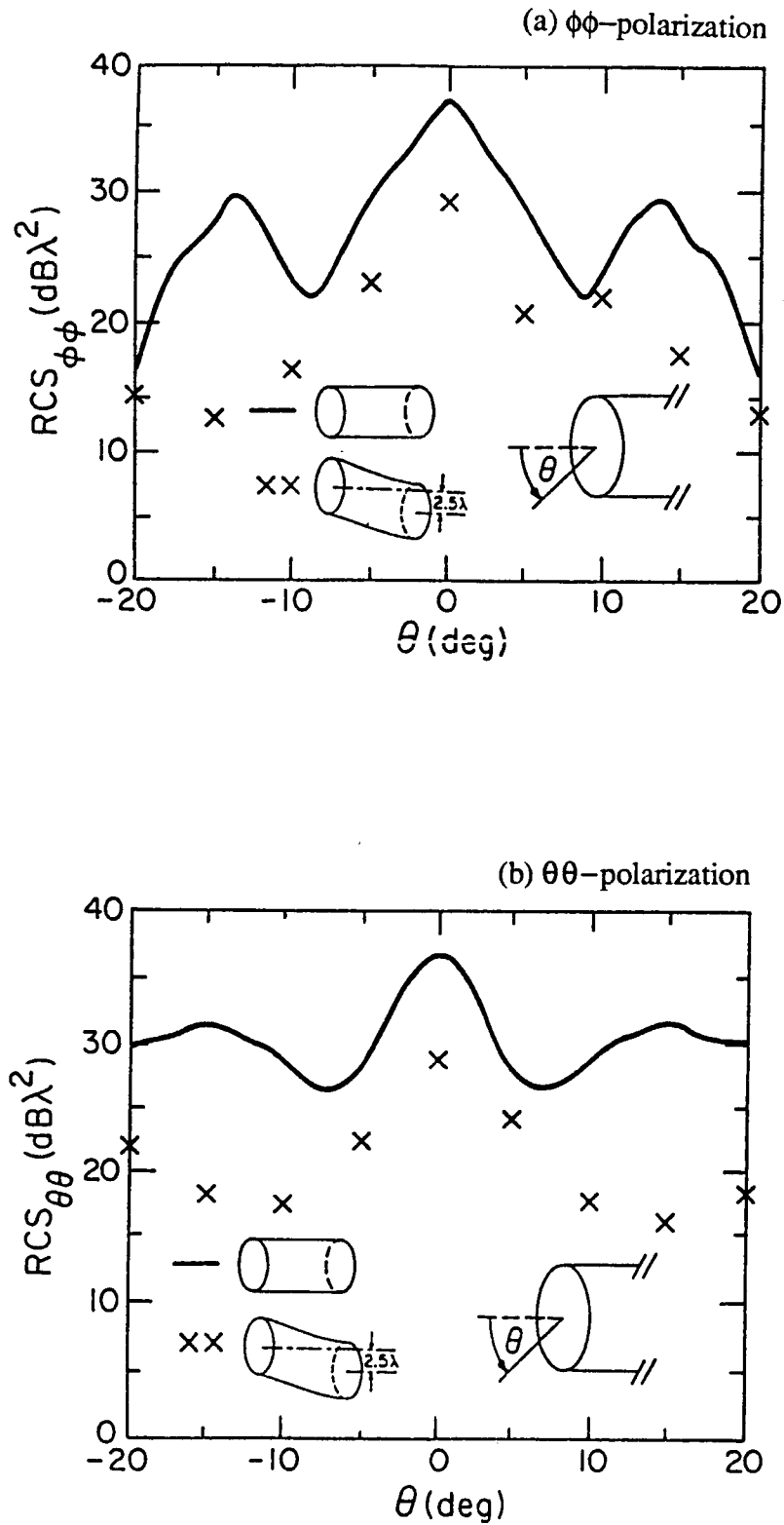


Fig. 4.22 Comparison of RCS's for straight circular cylinder (diameter of 5λ and depth of 10λ) with 2.5λ offset S-bend cylinder (same diameter and depth).
 (a) $\phi\phi$ -polarization, (b) $\theta\theta$ -polarization.

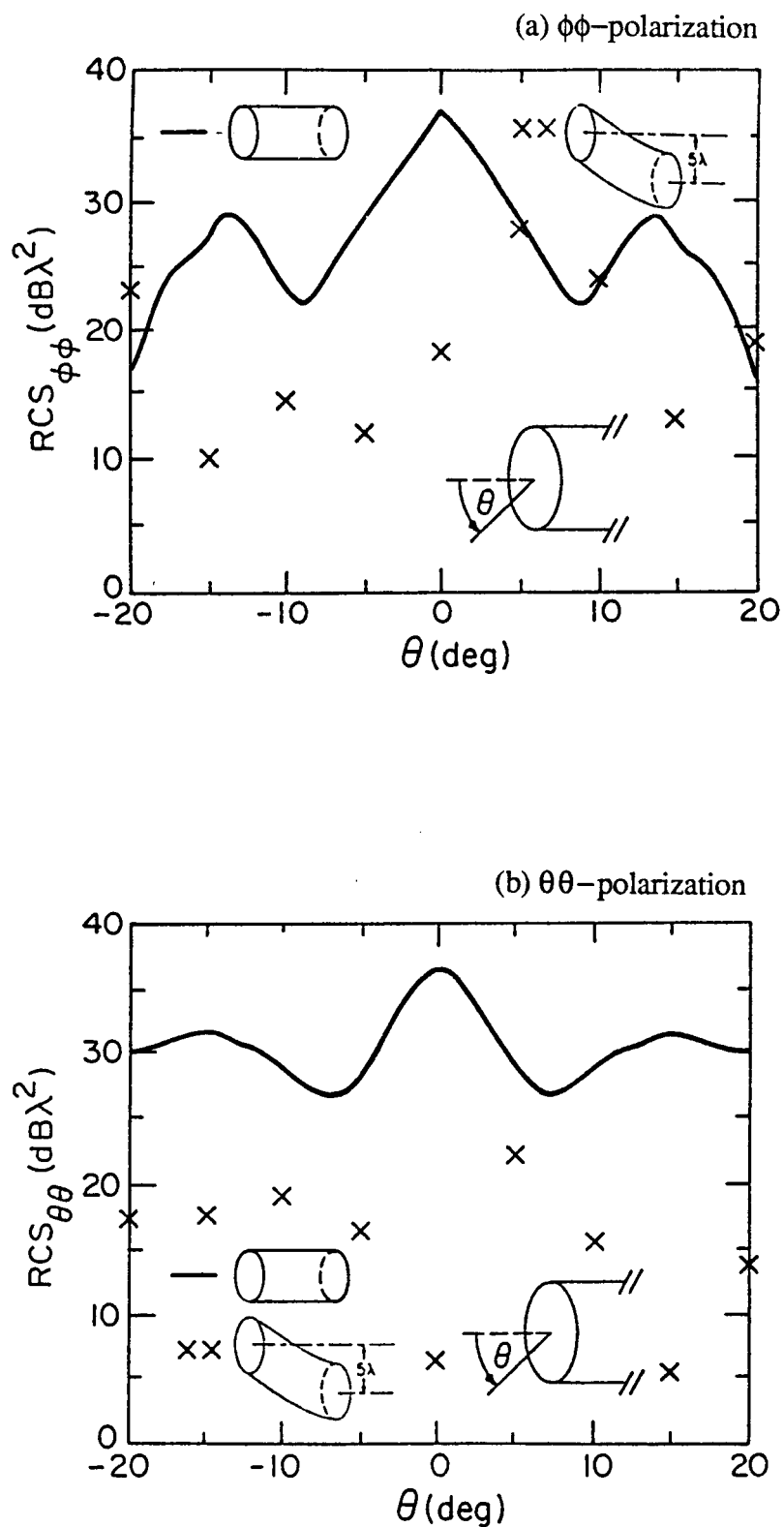


Fig. 4.23 Comparison of RCS's for straight circular cylinder (diameter of 5λ and depth of 10λ) with 5.0λ offset S-bend cylinder (same diameter and depth).
 (a) $\phi\phi$ -polarization, (b) $\theta\theta$ -polarization

both S-bend geometries show a reduction of RCS, there is a significant higher reduction near axial incidence by the 5.0λ offset. As the incidence angle increases to $\pm 20^\circ$, the RCS levels of both offsets become comparable. Figure 4.24 compares the RCS of a coated S-bend cylinder (2.5λ offset, $\epsilon_r = 2.5 - j1.25$, $\mu_r = 1.6 - j0.8$) to that of the uncoated S-bend and the straight cylinders. The coated S-bend case shows a 30 dB - 40 dB reduction across the range of angles calculated. Finally, Fig. 4.25 compares the RCS of the straight, the S-bend, and the S-bend with coating ($\epsilon_r = 2.5 - j1.25$, $\mu_r = 1.6 - j0.8$) transition waveguides. Again, the uncoated S-bend shows a good RCS reduction at near axial incidence, but the coated S-bend shows an even greater reduction over a greater range of incident angles.

4.4 Summary

The bouncing ray method presented in Chapter 3 was applied to study the electromagnetic scattering from several cavity structures. The emphasis was on shaping as a method of reducing the RCS of the cavities. It was shown that with a longitudinal S-bend, the RCS's of cylindrical cavities can be significantly reduced at near axial incidence. However, an S-bend cavity with coating causes an even greater RCS reduction, and over a greater range of incident angles. Convergence of the SBR method was demonstrated. S-bend geometries require a higher density of rays for convergence than their straight cylindrical counterparts.

SBR is a computer intensive method. The results in this chapter were generated on the NSF Cray X-MP supercomputer at the University of Illinois. For an S-bend structure, approximately 90 percent of the computation time is spent finding the ray paths in the cavity. In applications of this method, it is often of interest to compute the RCS of a geometry over a band of frequencies. The paths of the rays and the divergence factor (3.21) are independent of frequency. If the RCS is desired for more than one frequency value, the impact points of the

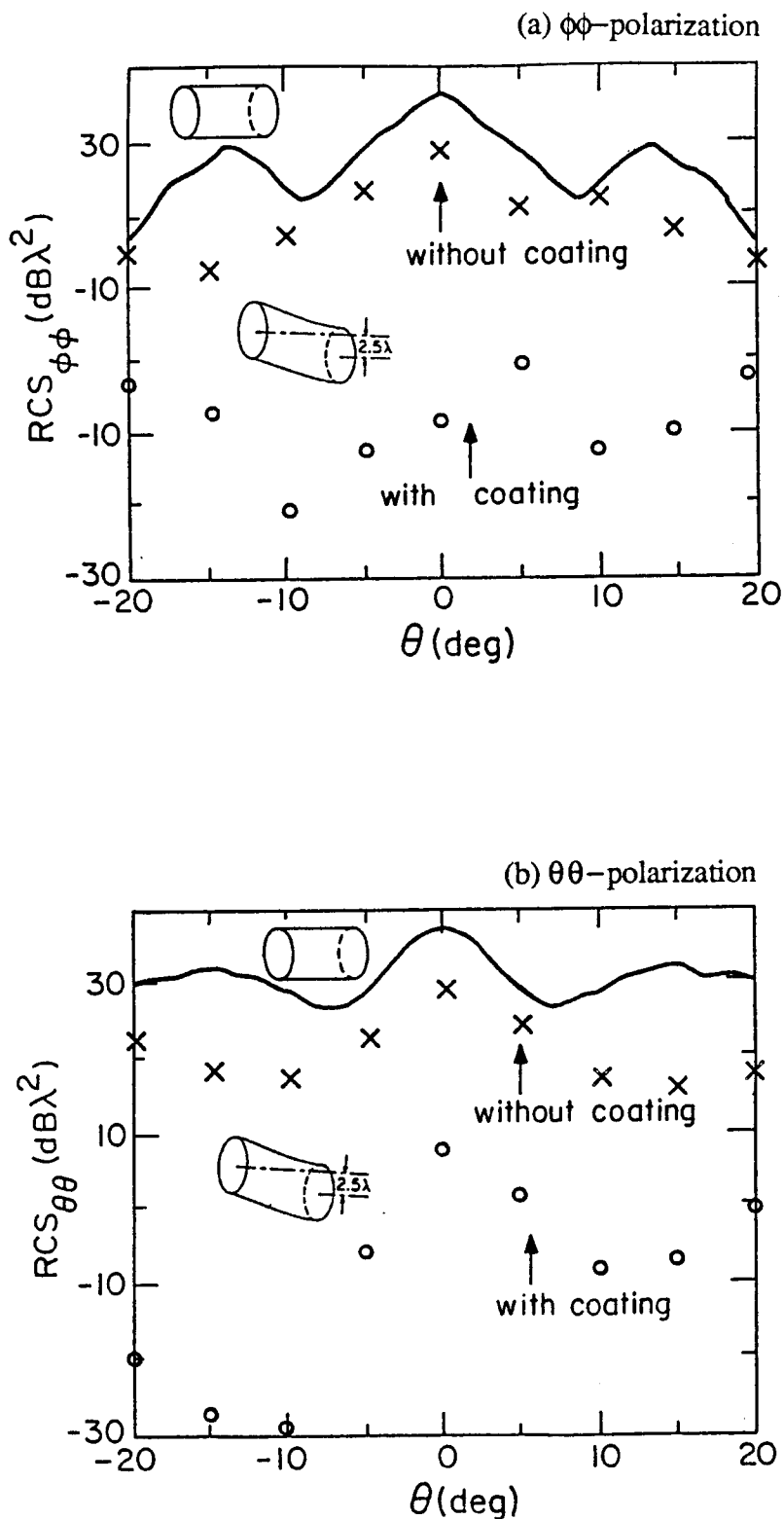


Fig. 4.24 Comparison of RCS's for straight circular cylinder (diameter of 5λ and depth of 10λ) with 2.5λ offset S-bend cylinder (same diameter and depth) and same S-bend with coating layer (thickness = 0.1λ , $\epsilon_r = 2.5 - j1.25$, $\mu_r = 1.6 - j0.8$). (a) $\phi\phi$ -polarization, (b) $\theta\theta$ -polarization.

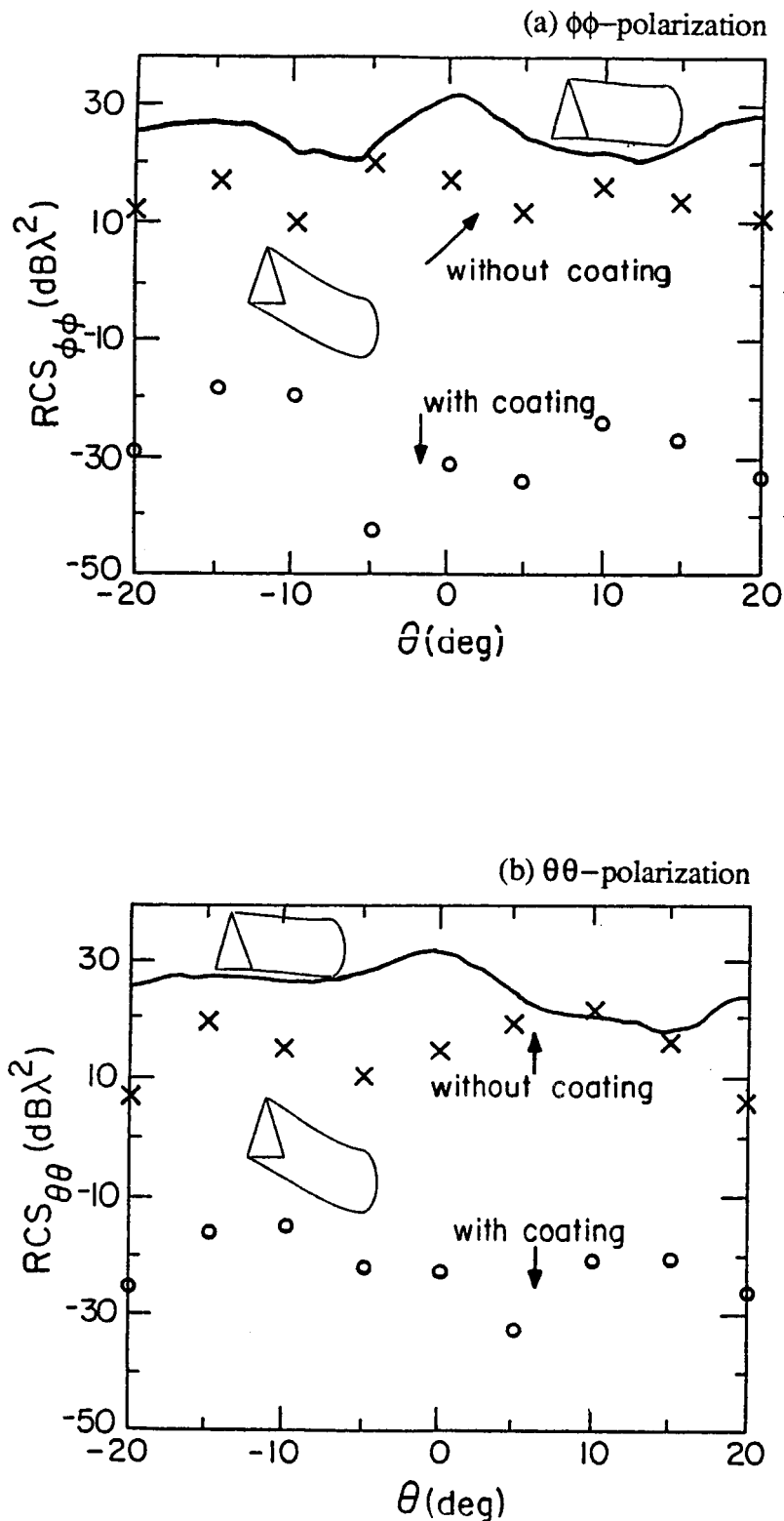


Fig. 4.25 Comparison of RCS's for triangle-to-circle transition waveguide (triangle side of 5λ , circle diameter of 4.5 , and depth of 4.05λ) with 4.05λ offset S-bend transition waveguide (same aperture, end diameter, and depth) and same S-bend with coating layer (thickness = 0.1λ , $\epsilon_r = 2.5 - j1.25$, $\mu_r = 1.6 - j0.8$).
 (a) $\phi\phi$ -polarization, (b) $\theta\theta$ -polarization

rays and the corresponding divergence factors could be written to a file and saved on the computer and simply read back for different frequency values. The density of rays used should correspond to a sufficiently high number to insure convergence for the highest frequency. This would result in a substantial reduction in total computation time.

CHAPTER 5

RAYS VERSUS MODES: PICTORIAL DISPLAY OF ENERGY FLOW IN AN OPEN-ENDED WAVEGUIDE

5.1 Introduction

Although the SBR method has shown promise in treating complicated structures, one of the important issues to address is, What are the limitations of this approach? This chapter addresses the above question by considering the problem of a plane wave impinging on a semi-infinite parallel-plate waveguide. Two alternative descriptions for the fields propagating in the waveguide are the "exact" modal analysis and GO - ray analysis, used by the SBR method. A comparison is made of the two field descriptions for the parallel-plate waveguide. Though the simple model of the parallel-plate waveguide was chosen because it best demonstrates the ray - mode equivalence, the results extend to other waveguide and cavity structures.

Based on ray optics, the fields and, therefore, the energy flow inside the guide should exhibit a beam behavior shown in Fig. 5.1. This physically intuitive ray picture is shown to be valid to a good extent if the separation of the waveguide plates is large compared to the wavelength. However, as the waveguide opening becomes smaller, the beam picture begins to blur after propagating a certain distance into the guide. These results are consistent with the fact that GO fields are high-frequency asymptotic solutions to Maxwell's equations. Although the complementary roles of ray and mode have been studied extensively in the past [37]-[39], this is believed to be the first graphical display showing the interplay between the two alternative descriptions of the fields.

5.2 Formulation

The problem under consideration is sketched in Fig. 5.2. The waveguide separation is given by a and the angle of the incident plane wave is θ . For the transverse electric (TE) polarized case, the incident electric field is assumed to be $(\exp(j\omega t)$ time convention)

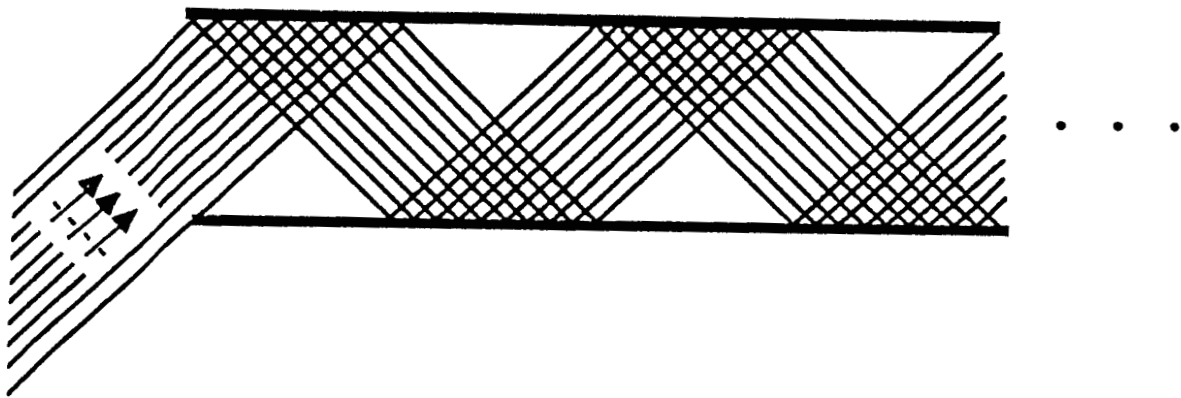


Fig. 5.1 Ray optical picture showing a beam bouncing back and forth in the parallel-plate waveguide.

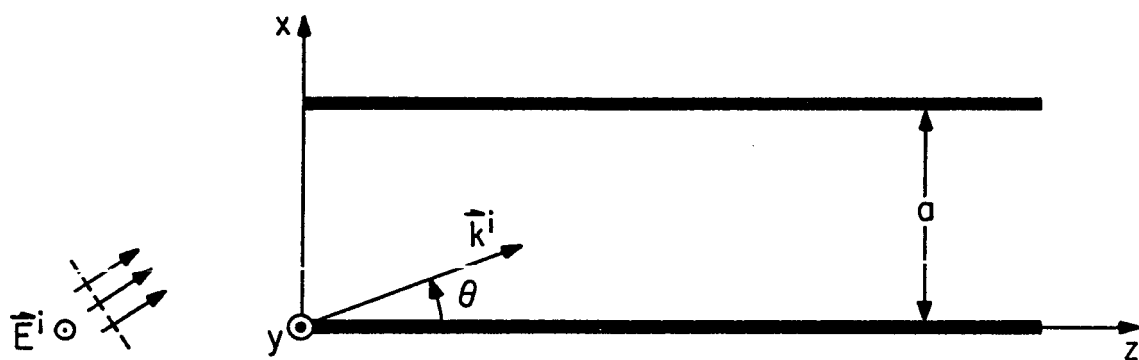


Fig. 5.2 Plane wave incident on a semi-infinite parallel-plate waveguide. The electric field vector is y -directed.

$$\vec{E} = \hat{y} e^{-jk_0 (\sin \theta x + \cos \theta z)} \quad (5.1)$$

where $k_0 = \omega \sqrt{\mu \epsilon}$ is the free-space wavenumber. The field excited inside of the waveguide can be described by TE modes:

$$E_y = \sum_{n=1}^{\infty} C_n \sin \frac{n\pi x}{a} e^{-jk_z z}$$

$$H_x = \sum_{n=1}^{\infty} C_n \left(\frac{k_z}{\omega \mu} \right) \sin \frac{n\pi x}{a} e^{-jk_z z}$$

$$H_z = \sum_{n=1}^{\infty} C_n \left(j \frac{n\pi}{\omega \mu a} \right) \cos \frac{n\pi x}{a} e^{-jk_z z} . \quad (5.2)$$

Here $k_z = [k_0^2 - (n\pi/a)^2]^{1/2}$ and C_n is the modal coefficient of the n th mode. The sign of k_z is to be taken as either positive real or negative imaginary.

For waveguide separation $k_0 a \gg 1$, Kirchoff's approximation can be used to determine the modal excitation coefficients by matching the incident field in (5.1) to the modal field in (5.2) at the aperture $z = 0$. The results are

$$C_n = \frac{2}{a} \int_0^a e^{-jk_0 \sin \theta x} \sin \frac{n\pi x}{a} dx$$

$$= \begin{cases} \left(\frac{2}{a}\right) \frac{(n\pi/a)}{\left(\frac{n\pi}{a}\right)^2 - (k_0 \sin \theta)^2} [e^{-jk_0 \sin \theta} (-1)^{n+1} + 1], \\ \quad \text{if } k_0 \sin \theta \neq \frac{n\pi}{a} \\ -j, \quad \text{if } k_0 \sin \theta = \frac{n\pi}{a} \end{cases} \quad (5.3)$$

It is important to point out that the present interest is mainly in observing the field behavior deep into the waveguide, not the details of the field distribution near the wave opening. Therefore, although the exact Wiener-Hopf solution exists for this problem [40], the Kirchhoff's approximation is sufficient for our purpose.

The above described procedure can also be applied to the transverse magnetic (TM) case. For the sake of brevity, the results for the TM case are not included here. The conclusions reached for the TE case can also be drawn for the TM case.

5.3 Numerical Discussion

Shown in Figs. 5.3(a) and 5.3(b) are plots of the energy flow inside the guide for waveguide separation $a = 50 \lambda$ and plane wave incident at $\theta = 30^\circ$. Each arrow contains information on both the magnitude and the direction of the Poynting vector $\text{Re}(\vec{E} \times \vec{H}^*)$ at that point. The size of the arrow is proportional to the magnitude of the Poynting vector. The direction of the arrow is the direction of the energy flow. All vectors with a magnitude of less than 3 dB of the incident field are too small to appear. The physically intuitive picture based on the ray argument is shown in Fig. 5.3(a) and the actual energy flow computed from the modal sum in (5.2) is shown in Fig. 5.3(b). Figure 5.3(c) is an enlargement of a section of Fig.

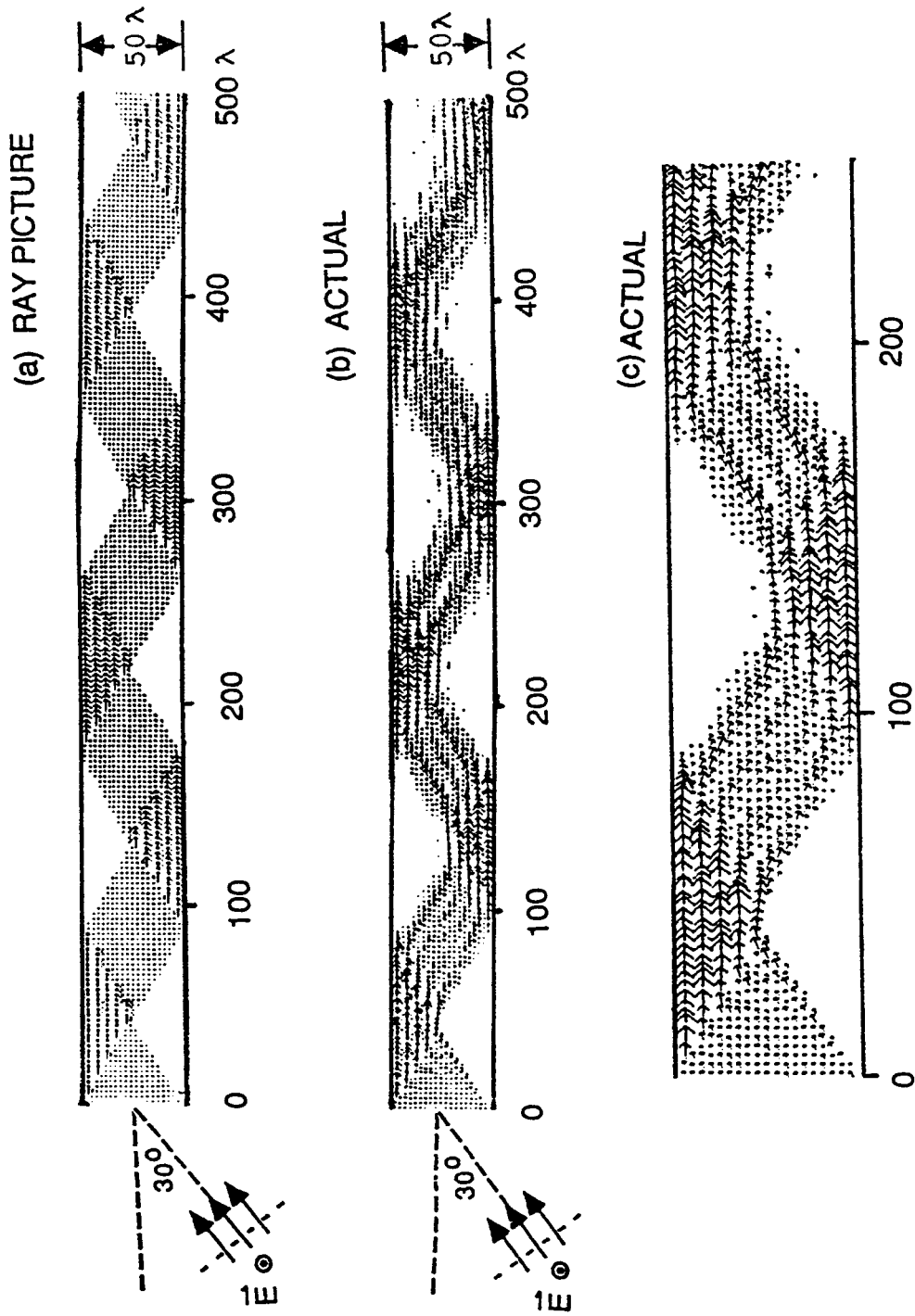


Fig. 5.3 Plots of Poynting vectors inside of a 50λ waveguide based on (a) the intuitive ray picture, (b) the actual fields obtained by summing up modes, and (c) an enlargement of a section of (b).

5.3(b) to show the details of the Poynting vectors. The evanescent modes are of little importance in the modal sum in the sense that there is no noticeable change in the energy plot if they are included or discarded. The resemblance of the actual distribution to the ray picture is apparent in this case. The fields in Fig. 5.3(b) are the sums of 99 propagating modes with different phase velocities. It is fascinating to observe that the modes add up to give an orderly ray picture.

As the waveguide separation is decreased to 10 and 3λ shown respectively in Figs. 5.4 and 5.5, the actual field no longer retains the beam behavior after some distance into the guide. The blurring occurs at approximately 70λ into the guide in Fig. 5.4(b) and 5λ in Fig. 5.5(b). In other words, the simple ray-optical picture is not accurate for describing the field after some depth into a small waveguide. Shown in Fig. 5.6 are the energy flow plots for various incident angles of a 5λ waveguide. The beam blurring is not a very strong function of the incident angle.

Finally, an interesting phenomenon is observed in Fig. 5.5(b) where the beam behavior reemerges after many wavelengths into the guide. At approximately $z = 25.5 \lambda$, the condition

$$[k_0^2 - (n\pi/a)]^{1/2} = \text{integer multiple of } 2\pi \quad (5.4)$$

is almost satisfied for all five of the propagating modes. The result is that the pattern from 0 to 25.5λ will be repeated approximately. Note, however, that the reemerged beam pattern no longer corresponds to the ray picture in Fig. 5.5(a). The same phenomenon is displayed in Fig. 5.7 for a 5λ waveguide. In this case the condition in (5.4) is satisfied at around $z = 60 \lambda$ for the nine propagating modes. If the waveguide separation is large and many propagating modes are excited, the distance inside the waveguide before observing this repetitive behavior will be extremely long.

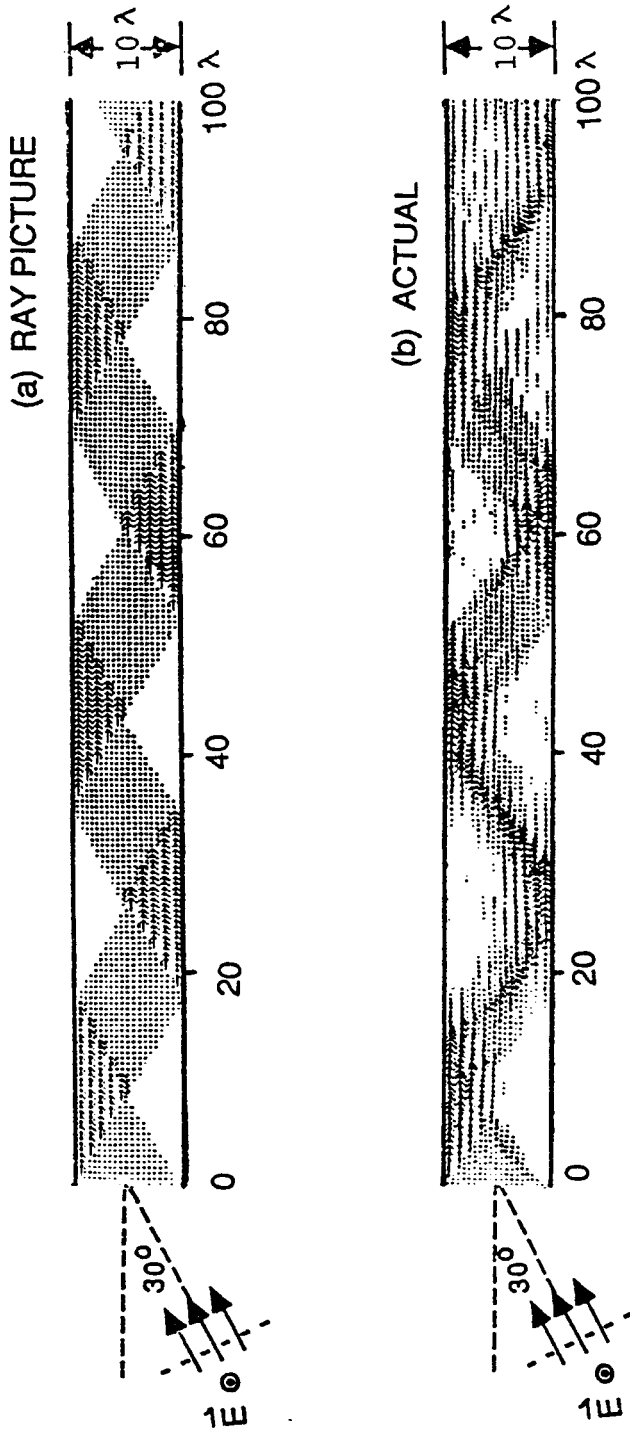


Fig. 5.4 Plots of Poynting vectors inside of a 10λ waveguide based on (a) the intuitive ray picture, (b) the actual fields obtained by summing up modes.

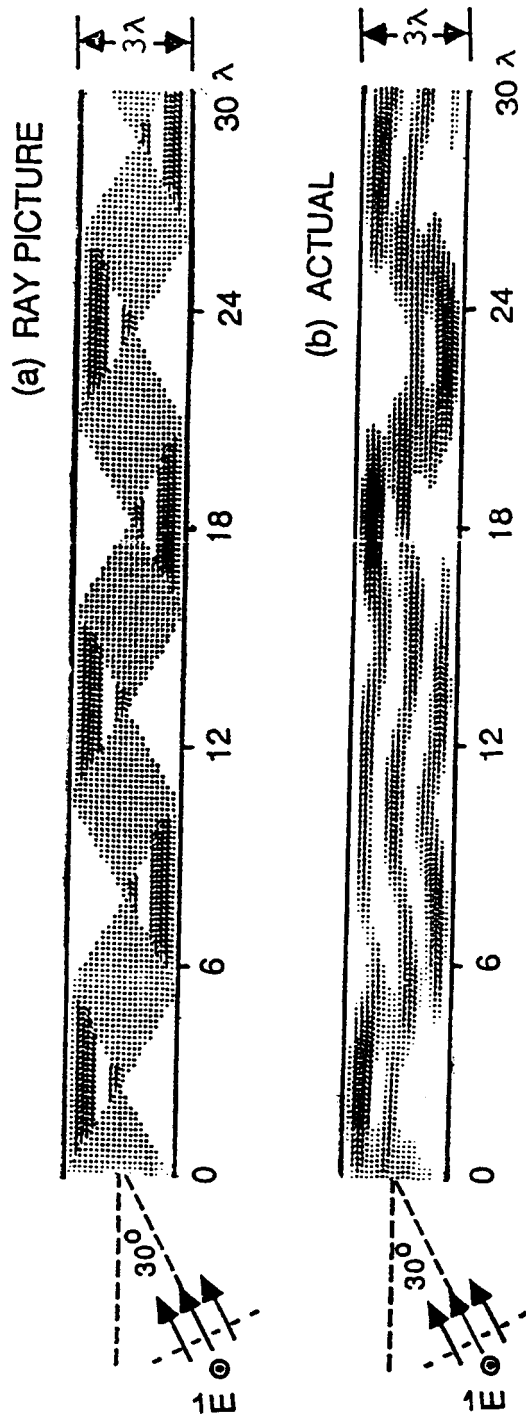


Fig. 5.5 Plots of Poynting vectors inside of a 3λ waveguide based on (a) the intuitive ray picture, (b) the actual fields obtained by summing up modes.

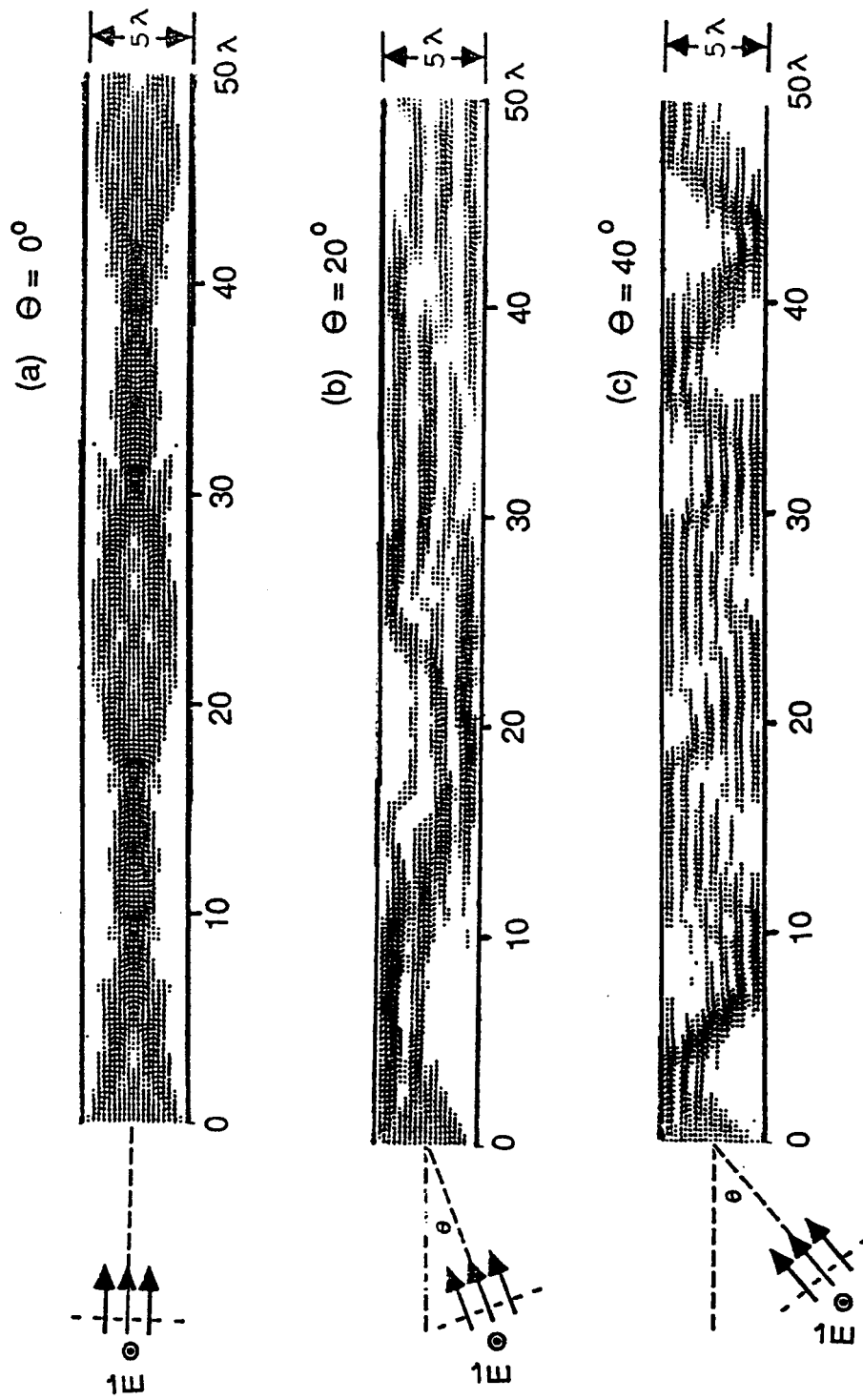


Fig. 5.6 Plots of Poynting vectors of the actual fields of a 5λ waveguide for various incident angles. (a) $\theta = 0^\circ$, (b) $\theta = 20^\circ$, (c) $\theta = 40^\circ$.

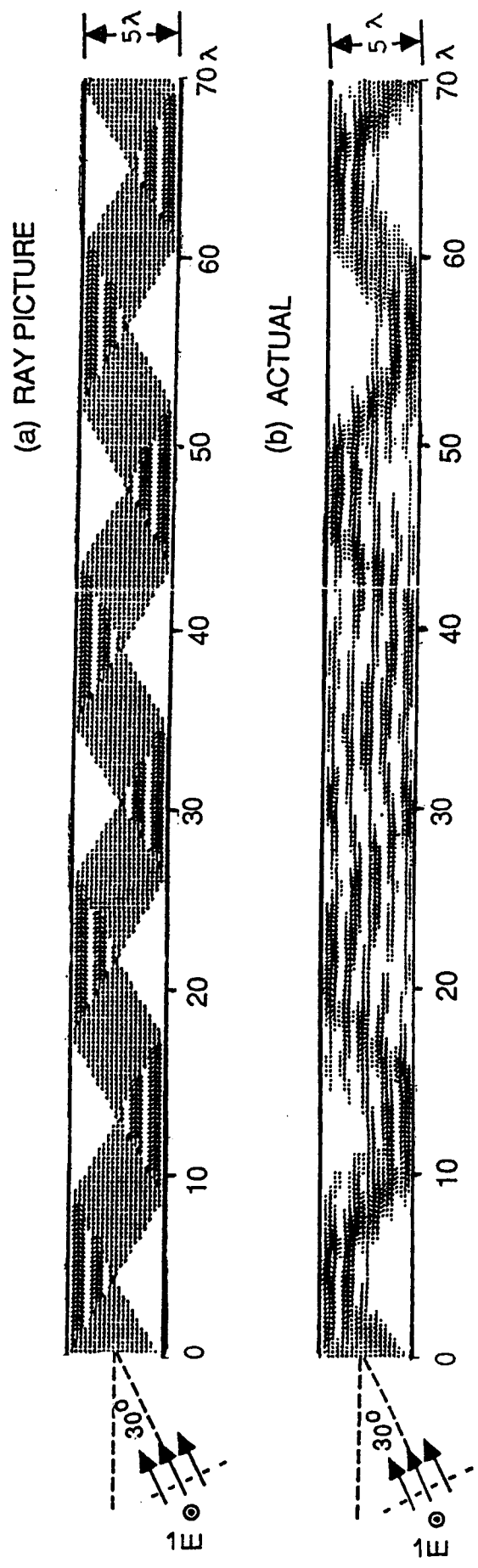


Fig. 5.7 Plots of Poynting vectors inside of a 5λ waveguide showing that the beam behavior reemerges after a chaotic region. (a) The intuitive ray picture, (b) the actual fields obtained by summing up modes.

5.4 Summary

This chapter demonstrated that the ray-optical description of the field in an open-ended waveguide excited by a plane wave is valid if the waveguide separation is large compared to the wavelength. As the waveguide separation gets smaller, the actual energy flow inside the guide begins to blur after propagating in a beamlike manner some distance into the guide. The simple ray-optical picture begins to break down at this point. Therefore, the GO-based SBR should be valid for deep cavities when the aperture is large compared to the wavelength. When the cavity is not too deep, SBR should also be valid for small apertures. For the small aperture, deep cavity case, the simple ray description must be modified to account for the beam blurring. This would possibly correct the discrepancy of the null predicted at $\theta = 10^\circ$ by SBR not found by modal analysis for the $\phi\phi$ -polarization in Fig. 3.11(a). The solution to this problem will enable the extension of the ray-bouncing technique to a wider class of problems.

CHAPTER 6

CONCLUSIONS AND EXTENSIONS

In this thesis, the problem of the reduction of the radar cross section of open-ended cavities was studied. The issues investigated were reduction through lossy coating materials on the inner cavity wall and reduction through shaping of the cavity. A new method was presented to calculate the RCS of any arbitrarily shaped structure in order to study the shaping problem. The limitations of this method were also addressed.

Chapter 2 studied modal attenuation in a multilayered coated waveguide. It was shown that by employing two layers of coating, it was possible to achieve an increase in both the magnitude of attenuation and the frequency band of effectiveness. It was also shown that the near axial incidence RCS of a terminated circular waveguide with a 4λ diameter aperture can be significantly reduced with a double layer of coating. As the angle of incidence increased, the effectiveness of the coating diminished. This is due to the fact that higher-order modes that are not highly attenuated by the given coating geometry are strongly excited at the wide angles of incidence. Further studies should be made in multilayered coatings to determine geometries that would result in a strong level of attenuation for higher-order modes in addition to the low-order modes. This would result in an increase in the range of effective RCS reduction not only in incidence angle, but in frequency as well, since more modes are excited in the guide as the frequency increases.

The numerical method used in finding the roots of the characteristic equation breaks down when the coating thickness is very lossy and large in terms of wavelength. For complex arguments with large imaginary components, the Bessel and Neumann functions are related by

$$\begin{aligned} J_{\nu}(z) &= iN_{\nu}(z) \\ J'_{\nu}(z) &= iN'_{\nu}(z) \end{aligned} \tag{6.1}$$

where $i = \sqrt{-1}$ and thus are no longer independent (shown in Appendix A). This causes the corresponding 4×4 matrices for that coating layer to become singular, and the matrix inversion in (2.9) is no longer possible. A reformulation of this problem using a different set of basis functions for the radial dependence of the modal fields might circumvent this problem.

Chapter 3 presented a new method of computing the RCS of an arbitrary cavity, and Chapter 4 applied this method to study the effects of longitudinal bending on RCS reduction. Of course, experimental results to verify the SBR calculations would be highly desirable. For a complex structure such as the S-bend, SBR requires a large number of rays per wavelength for numerically convergent solutions. This results in a large computation time. The development of the SBR computer code and the results generated for this thesis would not have been possible without the availability of the NSF Cray-XMP supercomputer. A more sophisticated scheme in determining the far fields from the aperture field of the cavity might reduce the number of rays needed for convergent results and greatly reduce the computer time.

Additionally, the SBR method could be applied to computing the RCS's of external structures in addition to cavity structures. One such use would be to use SBR to compute the RCS of, for example, a realistic model of an entire aircraft instead of idealized models of different components of the aircraft. This has the added advantage of being able to take into account mutual interaction between the various parts of the aircraft. Another possible application of SBR would be for the analysis of beam waveguide problems [41]-[44].

Finally, Chapter 5 compared the ray and modal descriptions for the fields in a parallel-plate waveguide. For large waveguide separations, the fields do indeed exhibit a beam behavior after travelling a very large distance into the guide. For small separations, the beam picture begins to blur a short distance into the guide. To extend the range of validity of the SBR method, the simple ray picture must be modified to account for the beam blurring. One improvement would be launching of edge diffracted rays. This has the difficulty that, in

general, one ray gives rise to an infinite amount of diffracted rays. Another possible improvement lies in finding a proper way to account for the propagation of a finite-width collimated beam.

APPENDIX A
BESSEL FUNCTIONS FOR LARGE ARGUMENTS
WITH LARGE IMAGINARY PARTS

For very lossy coating in an overmoded waveguide, $k_{\rho r}$ is complex with

$$\begin{aligned} |k_{\rho r}| &\gg 1 \\ \text{Im}(k_{\rho r}) &< 0 \\ |\text{Im}(k_{\rho r})| &\gg 1 \end{aligned} \tag{A.1}$$

From Abramowitz and Stegun [45], (9.1.2) and (9.1.3):

$$\begin{aligned} \text{For } |z| \rightarrow \infty: \quad J_{\nu}(z) &= \sqrt{\frac{2}{\pi z}} \cos\left(z - \frac{1}{2}\nu\pi - \frac{1}{4}\pi\right) \\ N_{\nu}(z) &= \sqrt{\frac{2}{\pi z}} \sin\left(z - \frac{1}{2}\nu\pi - \frac{1}{4}\pi\right). \end{aligned} \tag{A.2}$$

$$\text{Let } z' = z - \frac{1}{2}\nu\pi - \frac{1}{4}\pi.$$

If ν is fixed and finite, then

$$|z'| = \left|z - \frac{1}{2}\nu\pi - \frac{1}{4}\pi\right| \rightarrow \infty \quad \text{as} \quad |z| \rightarrow \infty. \tag{A.3}$$

Express z' as $z' = x + iy$ where x and y are purely real.

From Churchill [46], pg 57:

$$\begin{aligned} \sin z' &= \sin x \left(\frac{e^y + e^{-y}}{2}\right) + i \cos x \left(\frac{e^y - e^{-y}}{2}\right) \\ \cos z' &= \cos x \left(\frac{e^y + e^{-y}}{2}\right) - i \sin x \left(\frac{e^y - e^{-y}}{2}\right). \end{aligned} \tag{A.4}$$

If $y < 0$ and $|y| \gg 1$, then $e^{-y} \gg e^y$, and we have

$$\begin{aligned}\sin z' &= \frac{1}{2} e^{-y} (\sin x - i \cos x) \\ \cos z' &= \frac{1}{2} e^{-y} (\cos x + i \sin x).\end{aligned}\tag{A.5}$$

Clearly, $\cos z' = i \sin z'$. Therefore,

$$\begin{aligned}J_{\nu}(k_{\rho}r) &= iN_{\nu}(k_{\rho}r) \\ J'_{\nu}(k_{\rho}r) &= iN'_{\nu}(k_{\rho}r)\end{aligned}\tag{A.6}$$

when (A.1) holds.

REFERENCES

- [1] M. I. Skolnik, *Introduction to Radar Systems*. New York: McGraw-Hill Book Co., 1980.
- [2] A. Sommerfeld, *Math. Ann.*, vol. 47, p. 317, 1896.
- [3] G. Mie, "Beitrage zur Optik trüber Medien speziell kolloidaler Metallösungen," *Ann. Phy.*, vol. 25, pp. 337-445, 1908.
- [4] S. G. Marconi, "Radio Telegraphy," *Proc. IRE*, vol. 10, p. 237, 1922.
- [5] E. F. Knott, J. F. Shaeffer, and M. T. Tuley, *Radar Cross Section*. Dedham, Mass: Artech House, Inc., 1985.
- [6] P. Bedard, "Stealth Cars," *Car and Driver*, vol. 26, December 1980, pp. 140-148
- [7] H. A. Brooks and J. W. Crispin, Jr., "Comments on the RCS characteristics of cylinders, hollow pipes, and cylindrical cavities," Conductor Corporation Report No. 1801-2-T(0043-147), Ann Arbor, Michigan, Aug. 1966.
- [8] H. R. Witt and E. L. Price, "Scattering from hollow conducting cylinders," *Proc. IEE*, vol. 115, pp. 94-99, Jan. 1968.
- [9] S. Chang and T. B. A. Senior, "Scattering by a spherical shell with a circular aperture," Air Force Weapons Lab., Albuquerque, NM, Interaction Note 141, Apr. 1969.
- [10] J. W. Moll and R. G. Seecamp, "Calculation of radar reflecting properties of jet engine intakes using a waveguide model," *IEEE Tran. Aerosp. Electron. Sys.*, vol. AES-6, pp. 675-683, Sept. 1970.
- [11] T. W. Johnson and D. L. Moffat, "Electromagnetic scattering by open circular waveguide," *Radio Science*, vol. 17, no. 6, pp. 1547-1556, Nov. 1982.
- [12] C. S. Lee and S. W. Lee, "RCS of a coated circular waveguide terminated by a perfect conductor," *IEEE Trans. Antennas Propagat.*, vol. AP-35, pp. 391-398, April 1987.
- [13] C. S. Lee, S. L. Chuang, S. W. Lee, and Y. T. Lo, "Wave attenuation and mode dispersion in a waveguide coated with lossy dielectric material," University of Illinois Electromagnetics Laboratory, Urbana, IL, Technical Report, No. 84-13, July 1984.
- [14] C. S. Lee, S. W. Lee, and S. L. Chuang, "Normal modes in an overmoded circular waveguide coated with lossy material," *IEEE Trans. Microwave Theory Tech.*, vol. MTT-34, pp. 773-785, July 1986.
- [15] M. Miyagi, A. Hongo, and S. Kawakami, "Transmission characteristics of dielectric-coated metallic waveguide for infrared transmission: slab waveguide model," *IEEE J. Quantum Electron.*, vol. QE-19, pp. 136-145, Feb. 1983.

- [16] H. G. Unger, "Lined waveguide," *Bell System Tech. J.*, vol. 41, pp. 745-768, March 1962.
- [17] J. W. Carlin and P. D'Agostino, "Low-loss modes in dielectric lined waveguide," *Bell System Tech. J.*, vol. 50, pp. 1631-1638, May-June 1971.
- [18] J. W. Carlin and P. D'Agostino, "Normal modes in overmoded dielectric-lined circular waveguide," *Bell System Tech. J.*, vol. 52, pp. 453-486, April 1973.
- [19] E. A. J. Marcatili and R. A. Schmeltzer, "Hollow metallic and dielectric waveguides for long distance optical transmission and lasers," *Bell System Tech. J.*, vol. 43, pp. 1783-1809, July 1964.
- [20] C. Dragone, "High-frequency behavior of waveguides with finite surface impedances," *Bell System Tech. J.*, vol. 60, pp. 89-116, January 1981.
- [21] P. H. Pathak and A. Altintas, "An efficient approach for analyzing the EM coupling into large open-ended waveguide cavities," *1985 North American Radio Science Meeting Digest*, p. 216, Vancouver, Canada, 1985.
- [22] R. F. Harrington, *Time Harmonic Electromagnetic Fields*. New York: McGraw-Hill Book Co., 1961.
- [23] P. J. B. Clarricoats, "Propagation along unbounded and bounded dielectric rods," Part 1 and Part 2, *Proc. IEE*, Mon. 409E and 410E, pp.170-186.
- [24] C. Yeh and G. Lindgren, "Computing the propagation characteristics of radially stratified fibers: an efficient method," *Applied Optics*, vol. 16, pp. 483-493.
- [25] C. S. Lee, S. W. Lee and R. Chou, "RCS reduction of a cylindrical cavity by dielectric coating," *International IEEE/AP-S Symposium Digest*, pp. 305-308, Philadelphia, June 1986.
- [26] R. W. Ziolkowski and W. A. Johnson, "Plane wave scattering from an open spherical shell: a generalized dual series approach," *National Radio Science Meeting Digest*, p. 162, Boston, June 1984.
- [27] W. A. Johnson and R. W. Ziolkowski, "The scattering of an H-polarized plane wave from an axially slotted infinite cylinder: a dual series approach," *Radio Science*, vol. 19, no. 1, pp. 275-291, 1984.
- [28] C. -C. Huang, "Simple formula for the RCS of a finite hollow circular cylinder," *Electron. Lett.*, vol. 19, pp. 854-856, Sept. 1983.
- [29] S. W. Lee, P. Cramer, Jr., K. Woo, and Y. Rahmat-Samii, "Diffraction by an arbitrary subreflector: GTD solution," *IEEE Trans. Antennas Propagat.*, vol. AP-27, pp. 305-316, May 1979.
- [30] S. W. Lee, P. Cramer, Jr., K. Woo, and Y. Rahmat-Samii, Correction to "Diffraction by an arbitrary subreflector: GTD solution," *IEEE Trans. Antennas Propagat.*, vol. AP-34, p. 272, Feb. 1986.

- [31] S. W. Lee, M. S. Sheshadri, V. Jamnejad and R. Mittra, "Reflection at a curved dielectric interface: geometrical optics solution," *IEEE Trans. Microwave Theory Tech.*, vol. MTT-30, pp. 12-19, Jan. 1982.
- [32] M. Born and E. Wolf, *Principles of Optics*, Sec. 8.8.4. New York: MacMillan Co., 1964.
- [33] R. Mittra and A. Rushdi, "An efficient approach for computing the geometrical optics field reflected from a numerically specified surface," *IEEE Trans. Antennas Propagat.*, vol. AP-27, pp. 871-877, Nov. 1979.
- [34] S. W. Lee and R. Mittra, "Fourier transformation of a polygonal shape function and its application in electromagnetics," *IEEE Trans. Antennas Propagat.*, vol. AP-31, pp. 99-103, Jan. 1983.
- [35] H. Peot, "An electronic umbrella: the B1B defensive avionics system," , vol. 2, pp. 15-18, May 1984.
- [36] T. Ishihara, L. B. Felsen, and A. Green, "High-frequency fields excited by a line source located on a perfectly conducting concave cylindrical surface," *IEEE Trans. Antennas Propagat.*, vol. AP-26, pp. 757-767, Jan. 1978.
- [37] L. B. Felsen and H. Shirai, "Hybrid ray-mode analysis of high frequency wave coupling into large waveguides and cavities," *Opt. Lett.*, to appear.
- [38] L. B. Felsen and A. H. Kamel, "Hybrid ray-mode formulation of parallel plane waveguide Green's functions," *IEEE Trans. Antennas Propagat.*, vol. AP-29, pp. 637-649, July 1981.
- [39] L. B. Felsen, "Progressing and oscillatory waves for hybrid synthesis of source excited propagation and diffraction," *IEEE Trans. Antennas Propagat.*, vol. AP-32, pp. 775-796, Aug. 1984.
- [40] R. Mittra and S. W. Lee, *Analytical Techniques in the Theory of Guided Waves*. New York: Macmillan, 1971.
- [41] G. Goubau and F. Schwing, "On the guided propagation of electromagnetic wave beams," *IEEE Trans. Antennas Propagat.*, vol. AP-9, pp. 248-256, May 1961.
- [42] J. R. Christian and G. Goubau, "Experimental studies on a beam waveguide for millimeter waves," *IEEE Trans. Antennas Propagat.*, vol. AP-9, pp. 256-263, May 1961.
- [43] M. Mizusawa and T. Kitsuregawa, "A beam waveguide feed having a symmetric beam for Cassegrain antennas," *IEEE Trans. Antennas Propagat.*, vol. AP-21, pp. 884-886, Nov. 73.
- [44] T. -S. Chu, "An imaging beam waveguide feed," *IEEE Trans. Antennas Propagat.*, vol. AP-31, pp. 614-619, July 1983.

- [45] M. Abramowitz and I. A. Stegun, *Handbook of Mathematical Functions*. Washington: National Bureau of Standards, 1972.
- [46] R. V. Churchill, J. W. Brown, and R. F. Verhey, *Complex Variables and Applications*. New York: McGraw Hill Book Company, 1976.